

DEUTSCHES ELEKTRONEN-SYNCHROTRON
Ein Forschungszentrum der Helmholtz-Gemeinschaft



DESY 22-030
HU-EP-22/05
IFIC/22-05
arXiv:2202.07975
February 2022

Phenomenology of $tt \ X$ Production at the LHC

S. Alioli et al.

ISSN 0418-9833

NOTKESTRASSE 85 - 22607 HAMBURG

DESY behält sich alle Rechte für den Fall der Schutzrechtserteilung und für die wirtschaftliche Verwertung der in diesem Bericht enthaltenen Informationen vor.

DESY reserves all rights for commercial use of information included in this report, especially in case of filing application for or grant of patents.

Herausgeber und Vertrieb:

Verlag Deutsches Elektronen-Synchrotron DESY

DESY Bibliothek
Notkestr. 85
22607 Hamburg
Germany

Phenomenology of $t\bar{t}j + X$ production at the LHC

**Simone Alioli,^a Juan Fuster,^b Maria Vittoria Garzelli,^c Alessandro Gavardi,^a
Adrian Irlles,^b Davide Melini,^d Sven-Olaf Moch,^c Peter Uwer,^e Katharina Voß^{f c}**

^a*Dipartimento di Fisica “G. Occhialini”, Università degli Studi di Milano-Bicocca and INFN,
Sezione di Milano Bicocca,*

Piazza della Scienza 3, I – 20126 Milano, Italy

^b*IFIC, Universitat de València and CSIC,*

Catedrático Jose Beltrán 2, E – 46980 Paterna, Spain

^c*II. Institut für Theoretische Physik, Universität Hamburg,*

Luruper Chaussee 149, D – 22761 Hamburg, Germany

^d*Physics Department, Technion–Institute of Technology,*

Haifa 3200003, Israel

^e*Institut für Physik, Humboldt-Universität zu Berlin,*

Newtonstraße 15, D – 12489 Berlin, Germany

^f*Center For Particle Physics Siegen, Department Physik, Universität Siegen,*

Walter Flex Str. 3, D – 57068 Siegen, Germany

*E-mail: simone.alioli@unimib.it, fuster@ific.uv.es,
maria.vittoria.garzelli@desy.de, a.gavardi@campus.unimib.it,
adrian.irlles@ific.uv.es, davide.melini@cern.ch,
sven-olaf.moch@desy.de, peter.uwer@physik.hu-berlin.de,
katharina.voss@desy.de*

ABSTRACT: We present phenomenological results for $t\bar{t}j + X$ production at the Large Hadron Collider, of interest for designing forthcoming experimental analyses of this process. We focus on those cases where the $t\bar{t}j + X$ process is considered as a signal. We discuss present theoretical uncertainties and the dependence on relevant input parameters entering the computation. For the \mathcal{R} distribution, which depends on the invariant mass of the $t\bar{t}$ -system, we present reference predictions in the on-shell, $\overline{\text{MS}}$ and MSR top-quark mass renormalization schemes, applying the latter scheme to this process for the first time. Our conclusions are particularly interesting for those analyses aiming at extracting the top-quark mass from cross-section measurements.

KEYWORDS: QCD, NLO computations, top quark, LHC

Contents

1	Introduction and motivations for this work	2
2	Computational framework	3
3	Phenomenology of $t\bar{t}j$ production at the LHC	7
3.1	Options for scale choice and scale uncertainty evaluation	7
3.2	Comparison of NLO and LO differential cross sections	16
3.3	Effects of PDF + s M_z variation	23
3.4	Effects of variation of the R parameter used in jet reconstruction	33
4	Theoretical predictions for top-quark mass measurements using the \mathcal{R} distribution	34
4.1	Setup of the calculation	34
4.2	Conversion to the $\overline{\text{MS}}$ and MSR mass scheme	35
4.3	Exemplary results for the \mathcal{R} distribution using different parton distribution function sets and different renormalization schemes	37
4.4	Off-shell effects and non-resonant/non-factorizable contributions	41
5	Conclusions	47
A	Numerical results for cross sections for different scales, top-quark masses and analysis cuts	50

1 Introduction and motivations for this work

The $t\bar{t}j$ X production process at the Large Hadron Collider (LHC) is very interesting both as a signal and as a background in numerous experimental analyses. When considered as a signal, it can be used to extract precise values of the top-quark mass from measurements of differential cross sections particularly sensitive to the value of this Standard Model (SM) parameter. In particular, in Ref. [1] it has been argued that the additional jet activity in the $t\bar{t}j$ X process due to gluon radiation can lead to an enhanced mass sensitivity of the respective inclusive and differential cross sections, compared to the corresponding inclusive and differential cross sections for the $t\bar{t}$ X process. This may allow for a more precise measurement, while keeping the advantage of uniquely fixing the renormalization scheme of the extracted mass value through higher-order theoretical predictions.

More precisely, Ref. [1] introduced the following observable

$$\mathcal{R} = m_t^R \left(\frac{1}{\sigma_{t\bar{t}j}} \frac{d\sigma_{t\bar{t}j}}{ds} \right) m_t^R \quad (1.1)$$

with $\sigma_{t\bar{t}j}$ given by

$$\sigma_{t\bar{t}j} = \frac{2m_0}{\overline{s_{t\bar{t}j}}} \quad (1.2)$$

In the above definition, $\overline{s_{t\bar{t}j}}$ is the invariant mass of the $t\bar{t}j$ system, built from the top-quark pair and the hardest jet satisfying typical transverse momentum and pseudorapidity cuts depending on the experimental analysis, and m_t^R is used to denote the top-quark mass in the renormalization scheme R . We have not explicitly specified the renormalization scheme for the top-quark mass, as different schemes can be and have been employed. The ‘mass’ m_0 occurring in the definition of $\sigma_{t\bar{t}j}$ is an arbitrary scale to make $\sigma_{t\bar{t}j}$ dimensionless. In practical applications it is fixed to a value of the order of the top-quark mass, e.g. $m_0 = 170$ GeV that we will use in the following. As a proof of concept, the measurement of \mathcal{R} was used by the ATLAS collaboration to determine the top-quark mass in the on-shell scheme using LHC data collected at 7 TeV [2]. As a follow-up, the aforementioned published experimental results were used in Ref. [3] to determine the top-quark mass in the $\overline{\text{MS}}$ renormalization scheme. Later, also LHC data collected at 8 TeV were used by both the ATLAS and CMS collaborations [4, 5] to extract the top-quark mass, whereas new analyses exploiting the large statistics accumulated at $\sqrt{S} = 13$ TeV are in preparation.

Motivated by the experimental needs for the ongoing and forthcoming analyses, we present in this work theoretical predictions for the $t\bar{t}j$ X process, discuss their main theoretical uncertainties and study their dependence on the choice of the input parameters and on some of the experimental cuts for the jet reconstruction procedure. We also investigate the role of different top-quark mass renormalization schemes. Besides the on-shell and the $\overline{\text{MS}}$ schemes, already used in previous papers, in this work we apply, for the first time, the MSR top-quark mass renormalization scheme [6, 7] in deriving predictions for this process.

We limit our discussion to fixed-order predictions in the stable top-quark case, considering the sophisticated techniques that have been developed by the experimental collaborations to reconstruct top quarks from their decay products and to unfold their results from the particle to the parton level (see for example Refs. [5, 8]).

We provide reference predictions at next-to-leading order (NLO) accuracy, for different top-quark mass renormalization schemes and state-of-the-art choices for other input quantities, with the intent of providing useful information and concrete numerical results to the experimental collaborations in view of their ongoing $t\bar{t}j + X$ studies and top-quark mass extractions. In fact, to determine the top-quark mass in the experimental analyses in preparation, as well as in those already published so far, the unfolded measurements are compared with theoretical predictions with this accuracy in QCD.

The manuscript is organized as follows. In Section 2 we briefly describe the theoretical framework. Theoretical predictions for fiducial inclusive and differential cross sections and their uncertainties are discussed in Section 3, where we show their dependence on various inputs, including renormalization and factorization scale choices, parton distribution functions (PDFs) and the jet algorithm R parameter. In Section 4 we focus on the \mathcal{R} distribution, providing detailed predictions useful to the experimental collaborations to extract the top-quark mass value in different mass renormalization schemes. Furthermore we investigate the impact of off-shell effects and non-resonant/non-factorizable contributions. We conclude in Section 5. Further material and Tables with our reference numerical cross sections are collected in Appendix A.

2 Computational framework

NLO QCD corrections for $t\bar{t}j + X$ hadroproduction at the LHC have been computed and discussed in a number of papers, using multiple methods. In particular, Refs. [9, 10] consider the top quark as stable, Refs. [11] and [12] complement NLO QCD production with top-quark decays at LO and NLO, respectively, by working in the narrow width approximation (NWA) retaining spin correlations¹, whereas Refs. [13, 14] include full off-shellness and resonance effects for the cases where the top and antitop quarks decay leptonically. One-loop amplitudes for the parton-parton $t\bar{t}j$ process were first obtained analytically in Refs. [9, 10]. Refs. [11, 12] used instead generalized D -dimensional unitarity [15] in a numerical implementation, whereas Refs. [13, 14] are based on numerical results from HELAC-NLO [16], which provides one-loop amplitudes through a numerical implementation of the OPP method [17] complemented by effective Feynman rules for the calculation of the contribution due to the R_2 rational terms [18]. Nowadays, the same amplitudes can also be easily obtained, still numerically, by making use of various other automated tools (the so-called one-loop providers), such as MADLOOP [19], GOSAM [20, 21], OPEN-LOOPS [22, 23] and RECOLA [24, 25]. Real emission amplitudes can also be easily ob-

¹In Ref. [12] jet radiation from the top-quark decay products is also included.

tained numerically, and multiple automatic frameworks for the cancellation of the infrared singularities when combining real and virtual contributions at NLO have also been developed, working according to either the Catani-Seymour (CS) dipole subtraction method for calculations with massive partons [26], or the Frixione-Kunst-Signer (FKS) method [27], or the Nagy-Soper subtraction formalism [28, 29]. These developments have allowed for the automatic computation of fixed-order NLO cross sections with a variety of different tools, leading to predictions fully consistent among each other². Additionally, one-loop providers have been interfaced to computational frameworks providing NLO QCD matching to parton shower (PS) approaches, considering both the POWHEG [32, 33] and the MC@NLO [34] matching methods. In particular, first predictions with NLO QCD + PS accuracy for $t\bar{t}j$ production were obtained in the POWHEL framework [35], using numerical matrix elements from HELAC-NLO as input to the POWHEG-BOX implementation [36], interfaced to Shower Monte Carlo (SMC) codes. Top-quark decays as well as PS emissions besides the first one and hadronization effects were taken care of by the interface of the produced events at the first radiation emission level to the PYTHIA [37] and HERWIG [38] SMC. Subsequently, the analytical amplitudes of Refs. [9, 10] were also used as input to the POWHEG-BOX, producing, in case of stable top quarks, predictions [39] consistent with the previous ones. As an alternative to the top-quark decay by the SMC code, an in-house implementation of top-quark decays including spin correlations in the NWA was considered in Ref. [39]. On the other hand, one-loop amplitudes as automatically obtained by MADLOOP are at the core of the $t\bar{t}j$ NLO QCD + PS computation in the MADGRAPH5_AMC@NLO framework [40], which provides PS-dependent matching terms for various versions of the PYTHIA and HERWIG SMC approaches [37, 38, 41–43]. The MC@NLO matching method has also been implemented in the $t\bar{t}j$ NLO QCD + PS implementation of Ref. [44], using amplitudes from HELAC-NLO, in association with the DEDUCTOR PS approach [45, 46]. Furthermore, NLO electroweak (EW) corrections have been recently computed in Ref. [47], and embedded in the multi-jet merging technique MEPS@NLO [48], giving rise to merged predictions for $t\bar{t}$ and $t\bar{t}j$ including NLO QCD + EW radiative corrections³ together with PS and hadronization effects as available in the SHERPA SMC [49].

In this work we have used various frameworks to compute predictions for the $t\bar{t}j$ process at NLO QCD accuracy: i) the implementation as presented in Refs. [9, 10] and ii) the POWHEG-BOX, which makes use of the FKS method for the infrared subtraction as numerically implemented inside the code, together with either the analytical amplitudes of Refs. [9, 10], implemented in a C++ library, or the numerical amplitudes from

²The fully local schemes for the subtraction of infrared divergences employed at NLO are a necessary prerequisite for the consistency of the predictions. This is not guaranteed in different regularization frameworks, which use non-local methods for the subtraction, as pointed out recently in case of the Drell-Yan process at NNLO in Refs. [30, 31]. For the $t\bar{t}j$ process NNLO predictions are not yet available.

³In this implementation the dominant virtual electroweak corrections are incorporated exactly, whereas the NLO QED bremsstrahlung is accounted for in an approximate way.

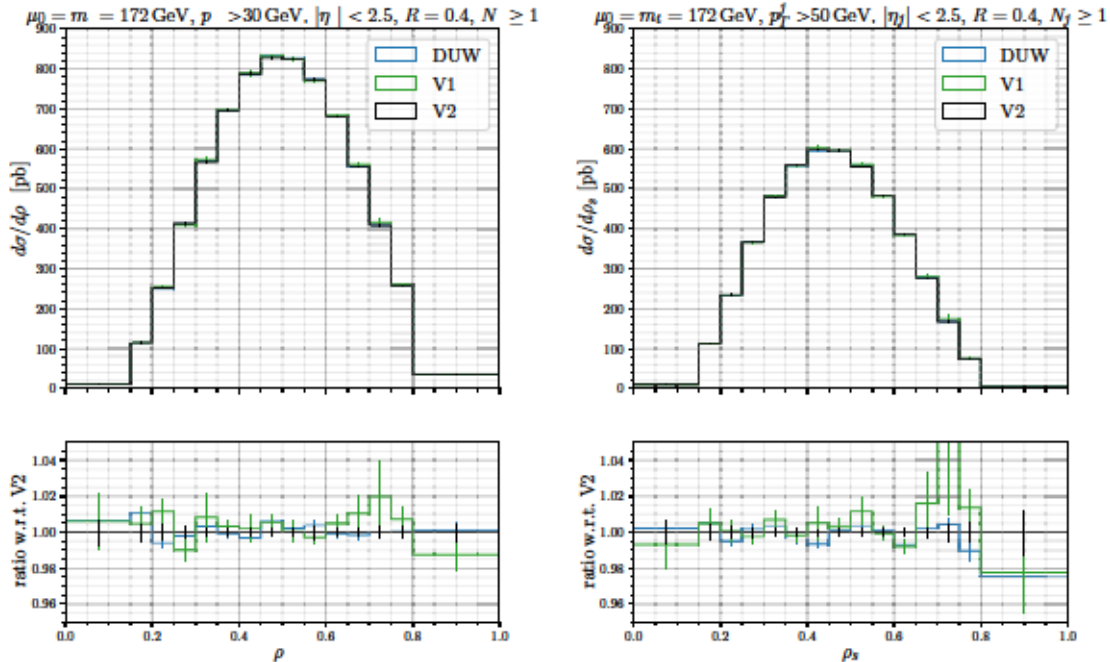


Figure 1. Comparison of predictions of the ρ_s distribution for $t\bar{t}j + X$ production in pp collisions at $\sqrt{s} = 13$ TeV using different frameworks described in the text: POWHEG-BOX-V2 (black) vs. POWHEG-BOX-V1 (green) vs. the in-house NLO implementation of Dittmaier-Uwer-Weinzierl (blue) in an analysis setup where at least one light jet reconstructed with the anti- k_T algorithm with $R = 0.4$ is required, with $|\eta_j| < 2.5$ and a p_T^j -cut of at least 30 GeV (left panel) and 50 GeV (right panel). The renormalization and factorization scales are fixed to the value of the top-quark mass $m_t = 172$ GeV.

OPENLOOPS 2. In particular, the first ones have been interfaced in the POWHEG-BOX-V1 framework, whereas the second ones have been interfaced to the POWHEG-BOX-V2, respectively. We have extensively cross-checked these frameworks by comparing predictions for many differential distributions among each other, using also different systems of cuts. In all cases we have obtained perfect agreement. An illustration of these cross-checks can be found in Fig. 1, using as an example the ρ_s distribution introduced in Section 1.

The computations of $t\bar{t}j + X$ hadroproduction have all been performed considering five active flavors at the scales relevant for this process, an assumption commonly adopted for most of the top quark related production processes⁴. Various modern PDF sets have

⁴Processes involving bottom-quarks as final states, like e.g. single-top and $t\bar{t}b\bar{b}$ production, besides in schemes with five active flavors, have also been computed in the decoupling factorization and renormalization scheme with four active flavors, i.e. considering massive b -quarks (see e.g. Refs. [50, 51]). For $t\bar{t}b\bar{b}$ the two descriptions have been shown to be compatible within uncertainties [51], at least for the experimental set of analysis cuts considered in that work. In $t\bar{t}j$ production at hadron colliders, the final-state jet j

been taken as input. In particular, in the present work we make use of the ABMP16 [52], CT18 [53], MMHT2014 [54], MSHT20 [55] and NNPDF3.1 [56] NLO PDF sets, together with their associated $\alpha_s M_Z$ value, and α_s evolution at two-loops according to the LHAPDF interface [57] for the phenomenological predictions presented in Section 3.

PDF uncertainties are computed according to the specific prescriptions associated to each set. As we will show in the following, for the distributions and the kinematical regions in which we are most interested, it turns out that PDF uncertainties obtained in NLO hadronic computations involving NLO PDFs ($+\alpha_s$) and NLO partonic cross sections have approximately the same relative size as PDF uncertainties obtained in LO hadronic computations involving NLO PDFs ($+\alpha_s$) and LO partonic cross sections. Therefore, considering that the second approach is computationally much faster than the first one, we make use of it in Section 3 in order to compute the NLO PDF uncertainty bands for a number of different PDF fits. We still make use of the first approach only when computing PDF uncertainties in association with our nominal PDF set (CT18 NLO). Additionally, we present some considerations concerning the effect of the simultaneous variation of $\alpha_s M_Z$ and PDFs, using as a basis a set of ABMP16 NLO PDF $+\alpha_s M_Z$ fits, which fully preserve the correlations between these quantities.

The predictions presented in Section 3 refer to the case when the top-quark mass is renormalized in the on-shell scheme, i.e. $m_t = m_t^{\text{pole}}$. On the other hand, in Section 4 we discuss how to obtain predictions with the top-quark mass renormalized in the MSR and $\overline{\text{MS}}$ schemes, while we always used the latter scheme for α_s renormalization, and present the corresponding results for selected distributions.

As further input, in Section 3 we consider various choices for the renormalization and factorization scales μ_R and μ_F . To that end, we define the quantities H_T^B and $m_{t\bar{t}j}^B$ as

$$H_T^B = \frac{\overline{p_T^{tB^2} m_t^2}}{\overline{p_T^{\bar{t}B^2} m_t^2} p_T^j B} \quad (2.1)$$

$$m_{t\bar{t}j}^B = \frac{\overline{p_t^B p_{\bar{t}}^B p_j^B}}{2} \quad (2.2)$$

which, as emphasized by the “ B ” superscript, are computed using the four-momenta of the outgoing particles of the underlying Born phase-space configuration in the POWHEG-BOX framework. The quantities H_T and $m_{t\bar{t}j}$ are defined in analogy to Eqs. (2.1) and (2.2) using instead the real emission kinematics at NLO for the four-momenta of the outgoing

can also be a b -jet. This case is however suppressed with respect to the cases where j is a light jet, also due to the smallness of the b -quark PDF with respect to the ones for other partons. Therefore, given that b -initiated contributions (absent when b is considered as a massive quark) are indeed small when b is taken to be massless, and that u, d, c, s quarks are massless in both cases, we do not expect a large difference in the description of the $t\bar{t}j$ production using either four or five active flavors. On the other hand, when considering scales well above m_t , as appropriate e.g. for the high- p_T^t and high- $m_{t\bar{t}j}$ tails, it might be worth to investigate the $t\bar{t}j$ process even in scheme with six active flavors. This may be done by using appropriate PDFs with six active flavors above the top-quark threshold. Most of the PDF fits available nowadays are however limited to a maximum of five active flavors.

particles, i.e. p_t , $p_{\bar{t}}$ and p_j . Central predictions are obtained by fixing $\mu_R = \mu_F = \mu_0$, with μ_0 being one of the following options:

$$1 \quad \mu_0 = m_t \quad 2 \quad \mu_0 = H_T^B/2 \quad 3 \quad \mu_0 = H_T^B/4 \quad 4 \quad \mu_0 = m_{ii}^B/2 \quad (2.3)$$

The scale uncertainties are obtained by the usual seven-point prescription, i.e. by varying independently μ_R and μ_F by factors of $[1/2, 2]$ around their central value, excluding the extreme configurations $(\mu_R, \mu_F) = (2, 0.5)\mu_0$ and $(0.5, 2)\mu_0$.

We reconstruct jets following the E -recombination scheme, according to which the energy and the momentum of a jet are defined as the sums of the energies and the momenta of its constituents, by using the anti- k_T jet clustering algorithm [58], with two different values for the jet radius parameter, $R = 0.4$ and $R = 0.8$. The first value is the present default value adopted by both the ATLAS and CMS collaborations in their analyses. We consider the second value as a possible alternative, in order to study the sensitivity of the predictions and their uncertainties in dependence on R .

A general discussion of the effects of these inputs on predictions for total and differential cross sections is included in Section 3.

3 Phenomenology of $t\bar{t}j$ production at the LHC

If not specified otherwise, the predictions presented in the following refer to our default configuration. This corresponds to a center-of-mass energy of $\sqrt{S} = 13$ TeV. The top-quark mass renormalized in the on-shell scheme is set to $m_t^{\text{pole}} = 172$ GeV. In our fixed-order computation the top quarks are considered as stable and the CT18 NLO PDF set is used as default. At the phenomenological analysis level, at least one jet is required with a transverse momentum $p_T^j \geq 30$ GeV and an absolute pseudorapidity $|\eta_j| \leq 2.4$. Jets are reconstructed using the anti- k_T jet clustering algorithm from FASTJET [59] (version 3.3.4) with $R = 0.4$ and the E -recombination scheme. This system of analysis cuts closely resembles typical systems of cuts used by the ATLAS and CMS experimental collaborations.

3.1 Options for scale choice and scale uncertainty evaluation

Before studying uncertainties related to PDF and R variation, as explained in Subsection 3.3 and 3.4, respectively, we investigated the influence of different central scale definitions on differential cross sections at NLO, considering many different observables. As mentioned in Eq. (2.3), we have considered four central scale choices, a static scale and three dynamical scales. The investigation of different μ_0 choices was motivated by observations presented in Ref. [14], where a more stable behavior of the scale variation uncertainty was found when using a dynamical scale with respect to the static scale case. However, while in the present manuscript the top quarks are considered as stable and the effects of relatively loose systems of cuts are investigated, in line with the procedures applied in ongoing experimental $t\bar{t}j + X$ analyses for the determination of the top-quark

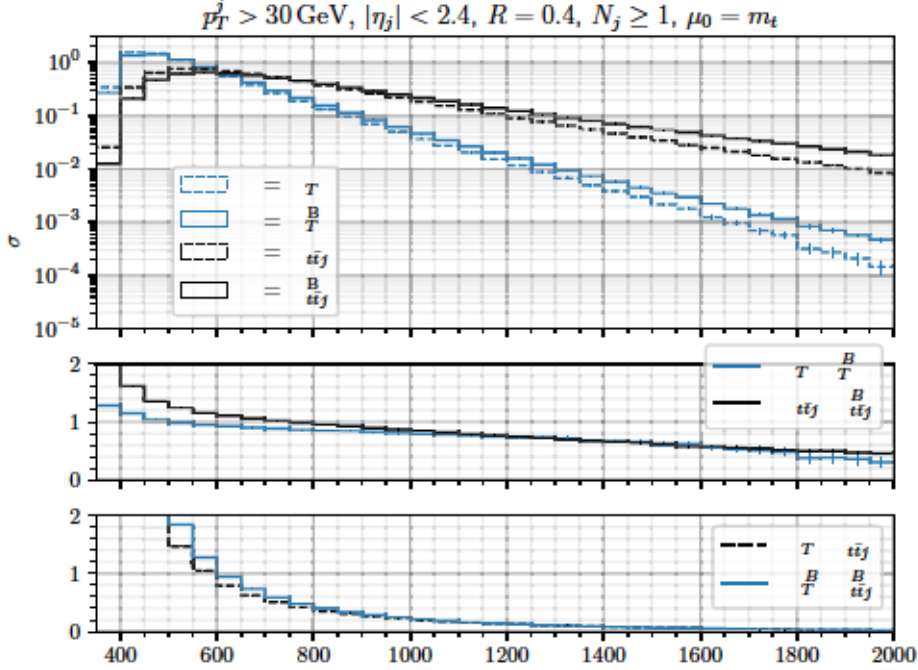


Figure 2. Differential cross section as a function of H_T^B (blue solid), H_T (blue dashed), m_{ii}^B (black solid) and m_{ii} (black dashed), calculated for the $pp \rightarrow t\bar{t}j + X$ process at a center of mass energy of $\sqrt{S} = 13 \text{ TeV}$, using as input a central scale μ_0 set to $\mu_0 = m_t$.

mass, in Ref. [14] the $t\bar{t}j + X$ process was studied in presence of fully leptonic top-quark decays and the analyzed events fulfilled more specific analysis cuts, which differ substantially from the more inclusive cuts used here. This difference motivates the work presented in this Subsection.

In Fig. 2 the NLO distributions in the variables H_T^B (blue solid), m_{ii}^B (black solid), H_T (blue dashed) and m_{ii} (black dashed) as defined in Eqs. (2.1) and (2.2) are shown for comparison. All these differential cross sections were obtained by setting the central scale to the fixed value $\mu_0 = m_t$. In the lower panels ratios between various pairs of these distributions are shown. It is evident that the m_{ii}^B and m_{ii} spectra are harder than the H_T^B and H_T ones. This leads to reduced integrated and differential cross sections when using the scales m_{ii}^B - or m_{ii} -based on the invariant-mass of the $t\bar{t}j$ -system compared to the H_T^B - or H_T -based scales as the coupling $\alpha_s(\mu_R)$ decreases for increasing scales μ_R . The same considerations also apply when comparing predictions obtained with $\mu_0 = H_T^B/2$ and $\mu_0 = H_T/4$, as we will discuss next. The dynamical central scale choices $\mu_0 = H_T^B/2$ and $\mu_0 = m_{ii}^B/2$ lead in general to larger numerical values for the renormalization and factorization scales, than the static scale choice $\mu_0 = m_t$. They are exactly equal to the latter only at threshold. Comparing the dashed and solid histograms in Fig. 2, we also

expect that the slightly different options H_T and $m_{t\bar{t}j}$ for the dynamical scales, i.e. building them from the real emission kinematics instead of from the underlying Born configuration, will lead to slightly larger cross-section values.

μ_0	LO [pb]	scale [pb]	NLO [pb]	scale [pb]	\mathcal{K}	NLO	LO
m_t	294.3	138.0 47% 87.5 30%	359.4	15.3 4% 41.5 12%		1.22	
H_T^B 2	231.08	100.30 43% 65.42 28%	331.9	34.9 11% 47.2 14%		1.44	
H_T^B 4	331.4	159.5 48% 100.3 30%	366.8	3.3 1% 34.9 10%		1.11	
$m_{t\bar{t}j}^B$ 2	202.17	83.91 42% 55.61 28%	302.5	35 12% 43.2 14%		1.50	

Table 1. Integrated cross section at LO and NLO of the process $pp \rightarrow t\bar{t}j + X$ with the analysis cuts $N_j = 1$, $p_T^j = 30\text{ GeV}$ and $j = 2, 4$, where the anti- k_T jet clustering algorithm with $R = 0.4$ and the CT18 NLO PDF set were used. The scale variation uncertainty δ_{scale} is obtained according to the seven-point scale variation procedure described in Section 2. In each δ_{scale} column, the first number refers to the absolute uncertainty due to scale variation, whereas the second number, indicated in parentheses, gives the same uncertainty in a percentage format.

The values of the integrated cross sections at LO and NLO under our default system of cuts described at the beginning of this Section are presented in Table 1 for the four central scale choices in Eq. (2.3). Thereby the seven-point scale variation was used to estimate the scale uncertainty δ_{scale} . The resulting \mathcal{K} -factors, given by the ratio of the NLO and LO integrated cross sections evaluated with each central scale, are presented in the last column. Both for the NLO and LO computations the CT18 NLO PDF set was used, accompanied by the associated default $\alpha_s^{\text{NLO}}(M_Z)$ value, equal to 0.118. Typical values of the strong coupling accompanying LO PDF sets are in general larger, amounting to $\alpha_s^{\text{LO}}(M_Z) = 0.13$ ⁵.

Using the static scale choice leads to larger values of the integrated cross section than the corresponding calculation with the dynamical scales $\mu_0 = H_T^B$ 2 and $\mu_0 = m_{t\bar{t}j}^B$ 2. On the other hand, the cross section obtained with the static scale is smaller than that obtained with the dynamical scale $\mu_0 = H_T^B$ 4. In the threshold region, $\mu_0 = H_T^B$ 4 is close to m_t 2, which leads to a larger α_s value in the bulk of the phase-space at the LHC, as compared to the static scale choice $\mu_0 = m_t$, and, with this, to a larger integrated cross section. The generally smaller cross sections obtained with $\mu_0 = m_{t\bar{t}j}^B$ 2 compared to $\mu_0 = H_T^B$ 2 can be explained by the harder spectrum of the $m_{t\bar{t}j}^B$ distribution (see Fig. 2), implying that events

⁵On the basis of this consideration, the LO cross sections, obtained using as input NLO (PDFs + $\alpha_s(M_Z)$) values and two-loop α_s evolution, have generally smaller values than those obtained with a LO (PDF + $\alpha_s(M_Z)$) set.

with large m_{ij}^B , leading to small values of $\sigma \mu_R \approx m_{ij}^B/2$, are more frequent than events with large H_T^B .

As expected the LO predictions suffer from larger scale uncertainties compared to the NLO results. A slightly asymmetrical scale variation uncertainty is observed at LO using all considered scale definitions, the size of the upper uncertainty band being larger than that of the lower one. The symmetrized scale uncertainties result in $38\text{--}39\%$ when using the static scale $\mu_0 = m_t$ and the dynamical scale $\mu_0 = H_T^B/4$, while they amount to $35\text{--}36\%$ for the dynamical scales $\mu_0 = H_T^B/2$ and $\mu_0 = m_{ij}^B/2$.

For NLO predictions with the static scale, the downward scale variation is dominant, leading to a clearly asymmetrical scale uncertainty of $\frac{4\%}{12\%}$ around the central value. This is also observed using the dynamical scale $\mu_0 = H_T^B/4$ with a scale uncertainty of the NLO integrated cross section under the analysis cuts amounting to $\frac{1\%}{10\%}$. Using other dynamical scale definitions, this asymmetry at NLO is strongly reduced, with scale uncertainties of $\frac{11\%}{14\%}$ in case of $\mu_0 = H_T^B/2$ and $\frac{12\%}{14\%}$ in case of $\mu_0 = m_{ij}^B/2$, around the respective central values.

The symmetrized scale uncertainty at NLO is larger when using the dynamical scales $\mu_0 = H_T^B/2$ and $\mu_0 = m_{ij}^B/2$, amounting to $12\text{--}13\%$ than for the static scale case, where it amounts to 8% . This can be explained as an artefact of the crossing of the scale variation graphs corresponding to different multiples (K_R, K_F) of the central renormalization and factorization scale, occurring only when using the static scale, as discussed in the following, which leads to an artificial reduction of the scale uncertainty in some kinematical regions. The smallest symmetrized scale uncertainty at NLO, of $5\text{--}5\%$, is found using the dynamical scale $\mu_0 = H_T^B/4$. As far as the inclusive cross section is concerned the static scale as well as the dynamical scale $\mu_0 = H_T^B/4$ show a moderate \mathcal{K} -factor suggesting a well behaved perturbative expansion. Furthermore, both scale settings give, within the uncertainty, consistent results. The two other dynamical scales lead to a larger \mathcal{K} -factor suggesting that higher-order corrections are sizable. This is consistent with the observation that for these scales the predictions are 10% or even 20% smaller than using the static scale or $H_T^B/4$.

In Fig. 3 the NLO QCD integrated fiducial cross sections are plotted, which were obtained by varying the factorization and renormalization scales simultaneously by the factor $x = 0.125, 0.25, 0.5, 1, 2, 4, 8$ (black) or by only varying μ_F (green) or μ_R (blue) while keeping the other scale (μ_R or μ_F , respectively) fixed. Following Ref. [14], a broad range of x values is considered, in order to check the stability of predictions with respect to scale variation. The standard seven-point scale variation procedure gives rise to a subset of these predictions, corresponding to the points $x = 0.5, 1, 2$. In Fig. 3 it can be seen that, as also noticed in [14], the (μ_R, μ_F) scale uncertainty band strongly depends on the variation of μ_R for all central scale choices considered in this paper, since the integrated cross section varies only marginally when changing the value of the factorization scale, if the renormalization scale is kept fixed (green). Thereby the influence of either renormalization or factorization scale variation can vary, when considering different central scale choices.

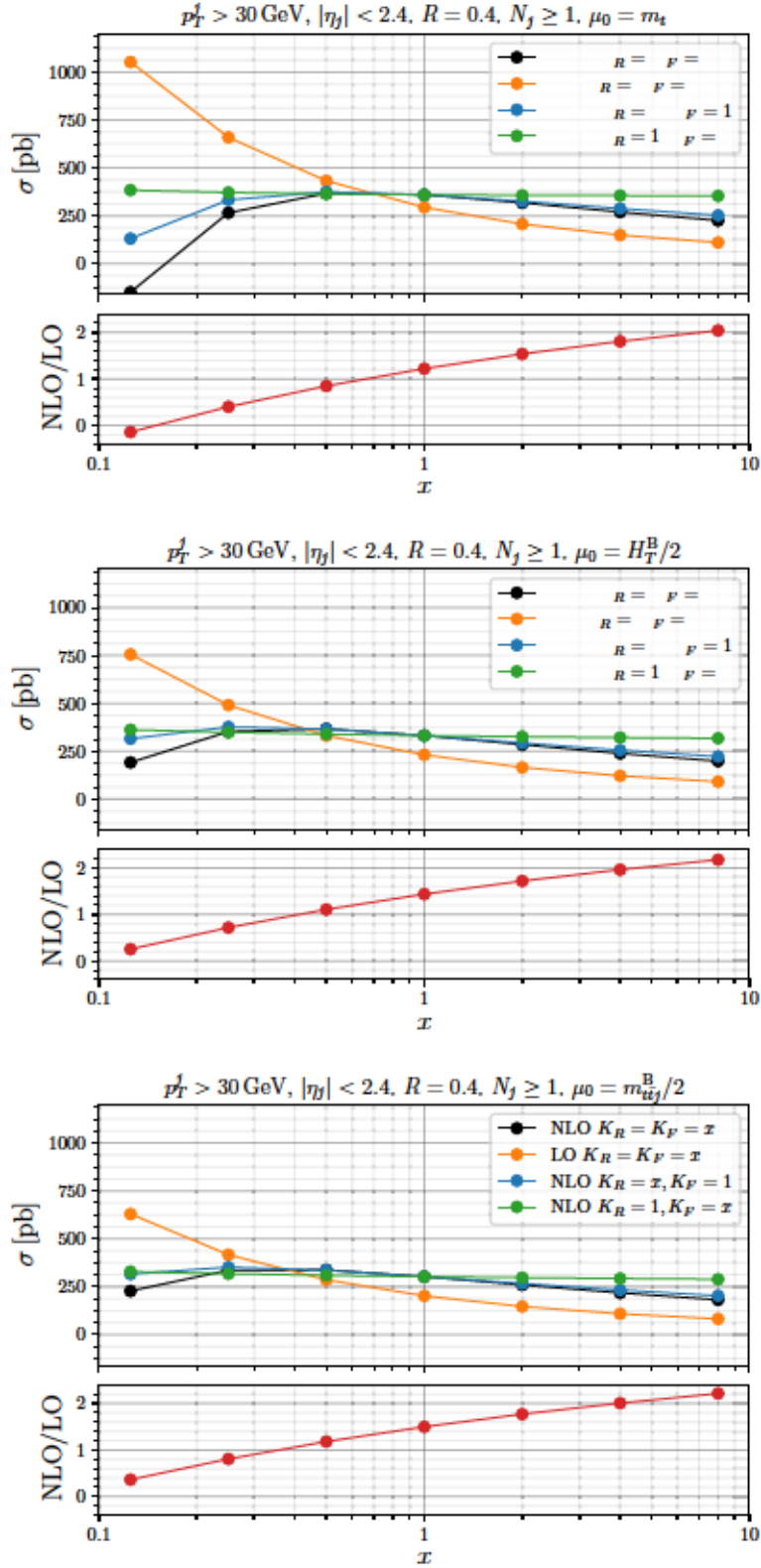


Figure 3. Integrated cross section of the $pp \rightarrow t\bar{t}j + X$ process after our default system of analysis cuts, using multiple (K_R, K_F) of the static scale definition $\mu_0 = m_t$ (upper panel) and of the dynamical scale definitions $\mu_0 = H_T^B/2$ (central panel) and $\mu_0 = m_{tj}^B/2$ (lower panel).

For example, when using $\mu_0 = H_T^B/4$ the μ_R dependence is less pronounced compared to using $\mu_0 = H_T^B/2$ in the seven-point scale variation, whereas the μ_F scale dependence is extremely mild in both cases. This can be seen by comparing the integrated cross sections in the intermediate panel in Fig. 3 for values of $x = 0.5/1/2$ and $x = 0.25/0.5/1$ corresponding to the seven-point scale variation using $\mu_0 = H_T^B/2$ and $\mu_0 = H_T^B/4$, respectively. The strong influence of the renormalization scale on the scale uncertainty is also evident from the fact that the $K_F = K_R = x$ results (black) follow closely the $K_F = 1/K_R = x$ ones (blue), with the exception of the very extreme case of $x = 0.125$. For extreme choices as $K_F = K_R = 0.125$ the cross section turns out to be negative, i.e. unphysical, for the static scale choice, but not for the dynamical scale choices. This was also noticed in Ref. [14].

The much larger width of the LO scale uncertainty band with respect to the NLO one can also be inferred from Fig. 3, being already evident when the factorization and renormalization scales are varied simultaneously by the factor $K_R = K_F = x$ (orange). In the lower inset of each panel of Fig. 3 the ratio between the NLO and LO predictions is shown. This ratio is computed from integrated cross sections obtained by varying μ_R and μ_F simultaneously by x in both the LO and NLO case. Thereby it can be seen that the smallest \mathcal{K} -factors using the dynamical scales are found for $\mu_0 = H_T^B/4$ and $\mu_0 = m_{ij}^B/4$. This motivates further investigation of these central scales. In the sequel only the central scale $\mu_0 = H_T^B/4$ is additionally studied, since the differential cross sections obtained using $\mu_0 = m_{ij}^B/4$ showed larger scale uncertainties, as better clarified in the following (see discussion of Fig. 5).

As a first differential cross section, the s distribution is investigated. In the most left panel of Fig. 4 the central scale prediction is shown obtained by setting $\mu_R = \mu_F = m_t$, while the graphs resulting from the various (K_R, K_F) combinations corresponding to seven-point scale variation, performed as discussed in Section 2, are also drawn individually. The scale variation uncertainty is rapidly increasing in the high energy tails of the distribution signaling that this region is not well described by the static scale. The high energy tail corresponds thereby to the region of low s values, since this implies large values of m_{ij} . Furthermore, a crossing of the scale variation graphs is observed for values of $0.1 < s < 0.3$. Also a clearly asymmetrical scale variation uncertainty band is found, in which the downwards variation is much larger than the upwards one for values of $0.4 < s < 0.7$. As already observed in case of integrated fiducial cross sections, also for the s differential distribution the renormalization scale dependence is stronger than the factorization scale one. This can be directly observed in the left panel, as graphs obtained with each fixed value of K_R and different values of K_F are grouped together. This behavior is especially clear when looking e.g. at the graphs with $K_R = 2$, noticing that for most of the s values they represent the minimum of the (μ_R, μ_F) uncertainty band. This behavior is also noticeable in the scale variation graphs obtained with the dynamical scales $\mu_0 = m_{ij}^B/2$ and $\mu_0 = H_T^B/2$ (second and third panels of Fig. 4). Using the central scale $\mu_0 = H_T^B/4$ (fourth panel) the stronger μ_R dependence with respect to the μ_F dependence is reduced, as was already noticed when comparing the integrated cross sections in Fig. 3.

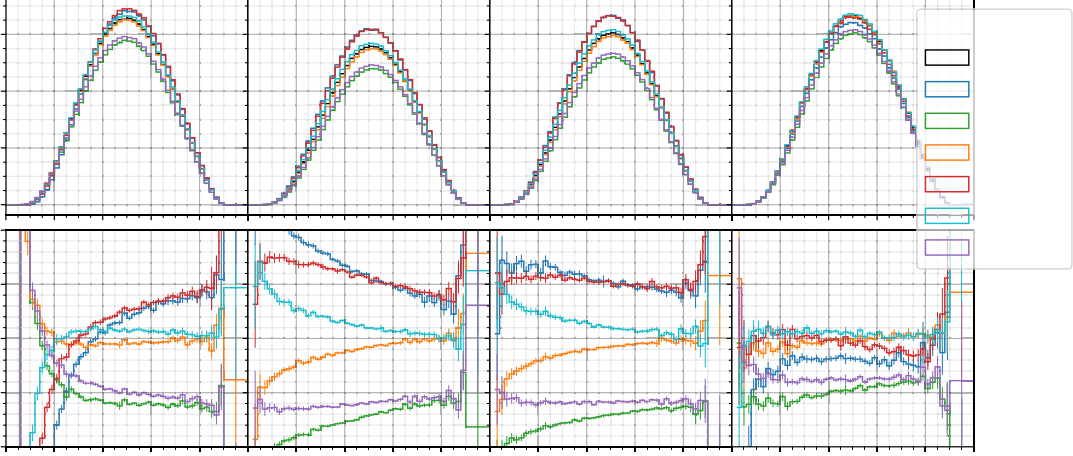


Figure 4. NLO differential cross section as a function of s for the $pp \rightarrow t\bar{t}j + X$ process at $\sqrt{S} = 13$ TeV using as central scales the static scale $\mu_0 = m_t$ (left panel) and the dynamical scales $\mu_0 = m_{t\bar{t}j}^B/2$, $H_T^B/2$, $H_T^B/4$. Thereby the seven-point scale variation graphs are explicitly drawn and the ratio between these and the central scale predictions are shown in the lower ratio plot. Due to low statistics for large values of s the distribution was rebinned, such that the region $s = 0.9 - 1$ corresponds to one bin.

In contrast to the static scale prediction in Fig. 4 (left panel), the predictions with dynamical scales (right panels) show a more uniform width of the scale variation uncertainty band in the high energy tails and in the bulk of the s distribution, especially when using the scales $\mu_0 = H_T^B/2$ and $\mu_0 = H_T^B/4$. In addition, only a reduced crossing of the scale variation graphs among each other is observed when using the dynamical scale. This is especially true for the scale choice $\mu_0 = H_T^B/4$ (last panel), for which the scale variation induces a nearly uniform shift of the central scale result, with the exception of the large s tail, where statistics is however very limited and experimental measurements are thus not possible, at least at present. When considering the normalized s distribution, this leads to strongly reduced scale variation uncertainties, if each scale variation graph is normalized by its respective integrated cross section. But even considering the differential cross section shown in Fig. 4, it is clearly visible that using the dynamical scale choice $\mu_0 = H_T^B/4$ the smallest scale variation uncertainties are obtained in the experimentally explored region. On the other hand, the differential cross sections obtained using $\mu_0 = m_{t\bar{t}j}^B/4$ show larger scale variation uncertainties and the differential cross sections evaluated with different K_R and K_F factors were found to cross each other, as displayed in Fig. 5. Therefore, in the following of this paper, we will not consider anymore the latter scale choice.

To better compare the distributions computed with different central scale choices, the

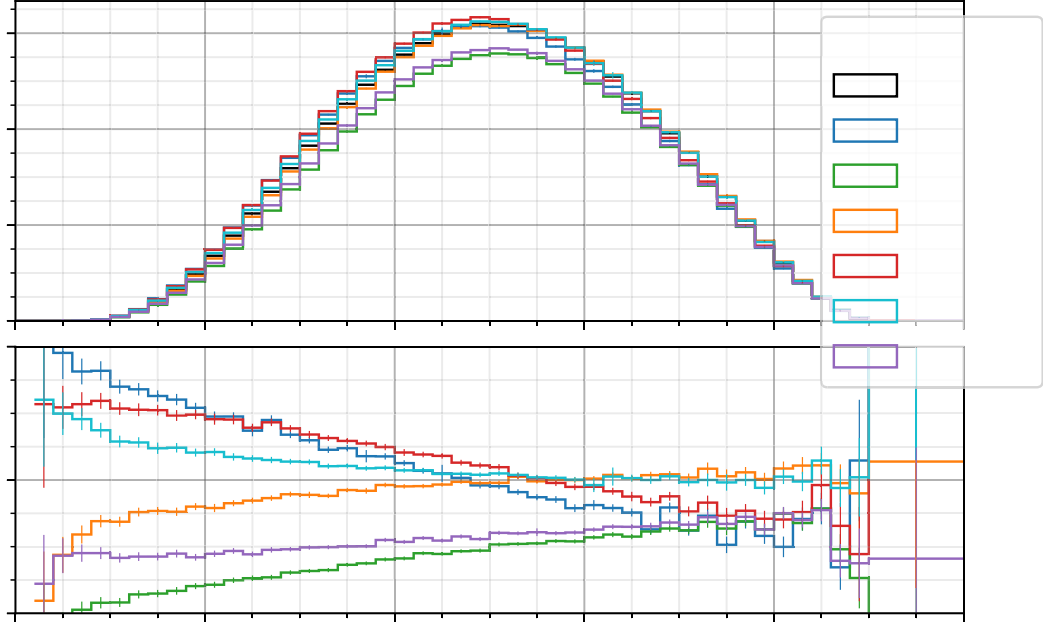


Figure 5. Same as the rightmost panel of Fig. 4, but using the scale $\mu_0 = m_{tj}^B/4$, instead of $H_T^B/4$.

envelope of the seven-point scale variation and the central scale prediction obtained by using either the static $\mu_0 = m_t$ (black) or the dynamical scale $\mu_0 = H_T^B/2$ (blue) are overlaid in the left panel of Fig. 6. Thereby in the lower two ratio plots the scale variation bands are rescaled by the corresponding central scale result. The relative distortion between the two central scale results is depicted with the red line, which shows the ratio between the distribution obtained with $\mu_R = \mu_F = H_T^B/2$ and the one obtained with $\mu_R = \mu_F = m_t$. From this ratio it can be seen that the differential cross section obtained with the dynamical scale evaluates in general to lower values compared to the one obtained with the static scale, excluding thereby the high-energy tail, in which an unstable behavior of the s distribution using the static scale was found. This can be explained due to the larger values of the scale (and, consequently, smaller values of s), which are obtained by applying the dynamical scale definition instead of the static one. The effect of the variation of s with the renormalization scale seems to be dominant compared to the effect of the explicit scale logarithm in the NLO corrections.

For large values of s the scale variation uncertainties for the distributions computed with $\mu_0 = H_T^B/2$ and $\mu_0 = m_t$ become very similar to each other. This is expected, since in this kinematic region of the s distribution close to threshold this dynamical and the

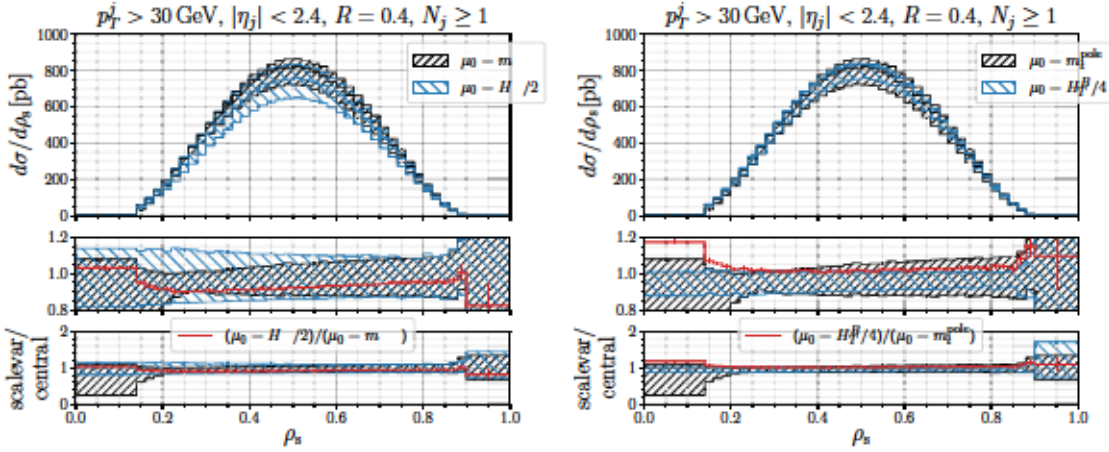


Figure 6. NLO differential cross section as a function of ρ_s for the $pp \rightarrow t\bar{t}j + X$ process at $\sqrt{s} = 13$ TeV calculated using the static central scale $\mu_0 = m_t$ (black) and the dynamical central scale $\mu_0 = H_T^B/2$ (blue) (left panel) or the dynamical central scale $\mu_0 = H_T^B/4$ (blue) (right panel). Thereby the envelopes of the seven-point scale variation and the central scale predictions are shown. In the two lower insets the ratios of the scale variation bands with the corresponding central scale predictions are shown with two different ranges on the y-axis, respectively. Additionally, the ratio of the central prediction obtained with the dynamical scale with the one obtained with $\mu_0 = m_t$ is shown with the red line.

static scale are becoming equal. As shown in the right panel of figure 6, with the choice $\mu_0 = H_T^B/4$ larger differential cross sections are found in the threshold region compared to using the scale $\mu_0 = m_t$, since the dynamical scale evaluates to lower values close to the threshold region.

Further it is observed that the scale variation uncertainty using the static scale is in fact reduced in the region of $0.2 \lesssim \rho_s \lesssim 0.4$ compared to the uncertainty obtained with the dynamical scale definition $\mu_0 = H_T^B/2$. This can be explained with the crossing of the scale variation graphs among each other in the static scale case in this region of the ρ_s distribution, as also seen in Fig. 4, leading to an artificial reduction of the scale variation uncertainty. For the lowest values of ρ_s the scale variation uncertainty is strongly reduced using the dynamical scale $\mu_0 = H_T^B/2$, as is evident from the lowest ratio in the left panel of Fig. 4. In contrast, using the static scale, a steep increase in the scale variation uncertainty was found in this region.

Looking at the right panel of Fig. 6, it is evident that this dynamical scale choice leads to central predictions more similar to those obtained with the static scale than the previously discussed $H_T^B/2$ choice (left panel). Additionally, they lead to a smaller uncertainty band size, as already discussed when commenting Fig. 4.

3.2 Comparison of NLO and LO differential cross sections

One of the indications of how well a scale definition is suited to describe a specific observable is the apparent convergence of the predictions, when including higher orders in the perturbative expansion. This applies for those cases where the same initial-state partonic channels are present at both orders ⁶.

To this end we compare the LO and NLO predictions obtained with the static and the dynamical scale choices ⁷. In Fig. 7 the LO and NLO differential cross sections in σ_s are compared among each other, using the scale choices in Eq. (2.3). In the middle ratio plot, below the σ_s distribution, the scale variation bands, normalized to the result obtained with $K_R = K_F = 1$ at either LO (black) or NLO (blue), are shown. The red line in the ratio plot indicates the differential \mathcal{K} -factor $d^{\text{NLO}}/d\sigma_s = d^{\text{LO}}/d\sigma_s$. In contrast, in the lowest ratio plot the scale variation bands are both rescaled by the LO result. This way it can be easily checked if the NLO and LO scale variation bands overlap.

As expected, the NLO scale variation band is generally smaller compared to the LO one. It turns out that, for $\sigma_s = 0.9$, the NLO predictions obtained with the dynamical scales $\mu_0 = H_T^B/2$ and $H_T^B/4$ are shifted to higher values with respect to the LO predictions, by an almost uniform differential \mathcal{K} -factor of ≈ 1.5 and 1.1 , respectively, as visible in Fig. 7. The scale uncertainty band is thereby reduced when going from LO to NLO and shows a nearly uniform width over the whole range of the σ_s distribution, amounting to about 10% for $\mu_0 = H_T^B/2$ and to about ($\approx 1\%$, $\approx 10\%$) for $\mu_0 = H_T^B/4$. On the other hand, the same distribution evaluated with the scale $\mu_0 = m_{t\bar{t}j}^B/2$, as shown in the second panel of Fig. 7, is characterized by a larger differential \mathcal{K} -factor for low values of σ_s , where $d^{\text{NLO}}/d\sigma_s = d^{\text{LO}}/d\sigma_s \approx 1.9$, than for high values of σ_s , where the differential \mathcal{K} -factor is found to be ≈ 1.4 (excluding the very last bin near threshold). Applying the scale definition $\mu_0 = m_{t\bar{t}j}^B/2$, the LO and NLO scale variation bands depart from each other in the low σ_s region, signaling that this region is not well described. The aforementioned behaviour can be understood from the fact that the process is a multi-scale problem. While for inclusive quantities, the invariant mass of the final states at the underlying Born level $m_{t\bar{t}j}^B/2$ gives an appropriate scale setting, the scale relevant for the emission of the additional jet can be much lower. As a consequence, one expects that observables relying significantly on the additional emission are not well described using the $m_{t\bar{t}j}^B/2$ scale. This implies a large \mathcal{K} -factor using this setting as at NLO accuracy the scale dependence should be reduced with respect to LO and differences in the predictions on the basis of different choices should be attenuated as well.

In case of the static scale $\mu_0 = m_t$, the central values of the NLO and LO distributions are strongly distorted one with respect to each other, as shown in the first panel of Fig. 7. A

⁶Differently from the case of $t\bar{t}$ production, for $t\bar{t}j$ production the qg , gq , $\bar{q}g$ and $g\bar{q}$ channels contribute already at LO, together with the gg and $q\bar{q}$ channels.

⁷Both NLO and LO predictions are obtained by using the CT18 NLO PDF set with its own $\sigma_s M_Z = 0.118$ value and two-loop σ_s evolution, see also Sections 3.1 and 3.3.

crossing of the NLO and LO distributions evaluated with $K_R = K_F = 1$ occurs in the same region of the s distribution, namely at $s = 0.2$, where the NLO predictions, evaluated at the scales that allow to build the seven-point scale variation band, cross among each others (see the left panel of Fig. 4). Additionally, with the static scale definition, the NLO and LO scale variation bands are only marginally overlapping in the high s region. As follows from the relation between s and $m_{t\bar{t}}$ in the definition of s , the features of the s distribution at low s calculated with the different scales are of course reflected in the $m_{t\bar{t}}$ distributions for large values of $m_{t\bar{t}}$, shown in Fig. 8.

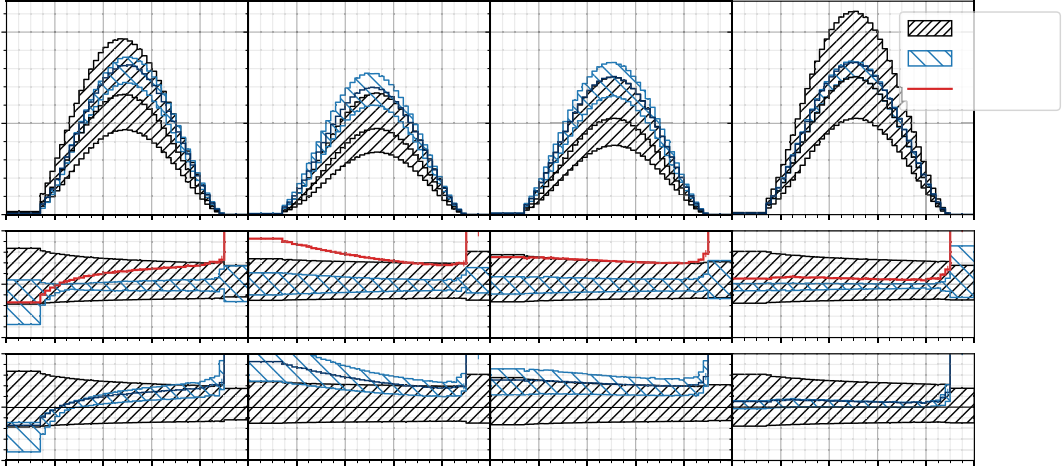


Figure 7. Central predictions for the s distribution at NLO (blue) and LO (black), together the corresponding NLO and LO seven-point scale variation uncertainty bands, using as a central scale $\mu_0 = m_t, m_{t\bar{t}}^B/2, H_T^B/2$ and $H_T^B/4$ (from left to right). In the middle ratio plot the scale variation uncertainty at either NLO or LO is rescaled by the central scale prediction at NLO or LO respectively. To visualize the difference between the NLO and LO differential cross section the ratio of the NLO and LO central scale predictions is shown in red. In the bottom ratio insets both the NLO and LO scale variation uncertainty bands are rescaled by the LO central scale prediction.

Another distribution, in which the more stable behavior in the high-energy tail with the dynamical scale choices is visible, is the invariant mass of the top-quark pair $m_{t\bar{t}} = \sqrt{p_t^2 + p_{\bar{t}}^2}$, shown in Fig. 9. In case of the static scale assignment (left panel), for large values of the invariant mass of the top-quark pair, the scale variation band at NLO departs from the LO one. This signals again an instability in the high energy tail of the distribution. The width of the NLO scale uncertainty band is smaller with respect to the LO one at small values of $m_{t\bar{t}}$, whereas in the high energy tail the NLO scale variation band shows a strong increase, being of similar size as the LO band for $m_{t\bar{t}} = 1.5$ TeV. Also in this distribution a distortion of the central NLO prediction with respect to the corresponding LO one is

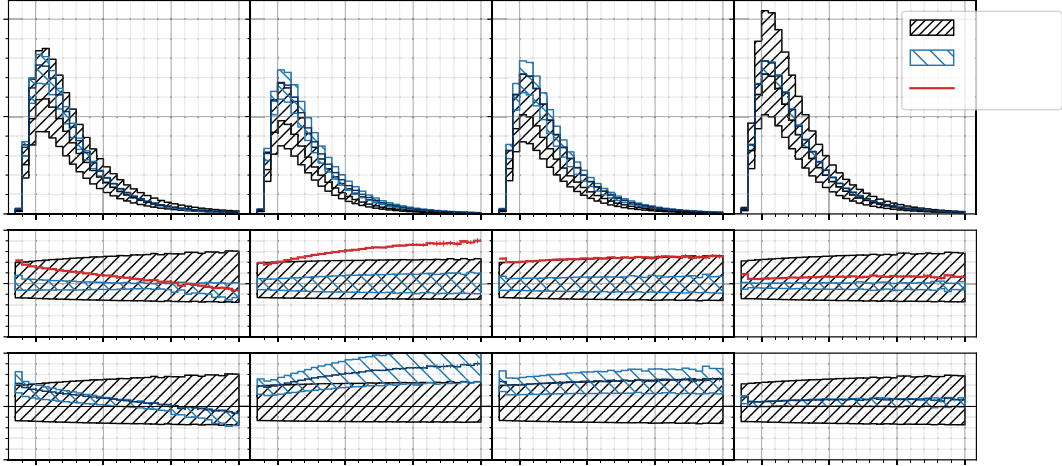


Figure 8. Same as in Fig. 7, but for the $m_{i\bar{i}}$ distribution.

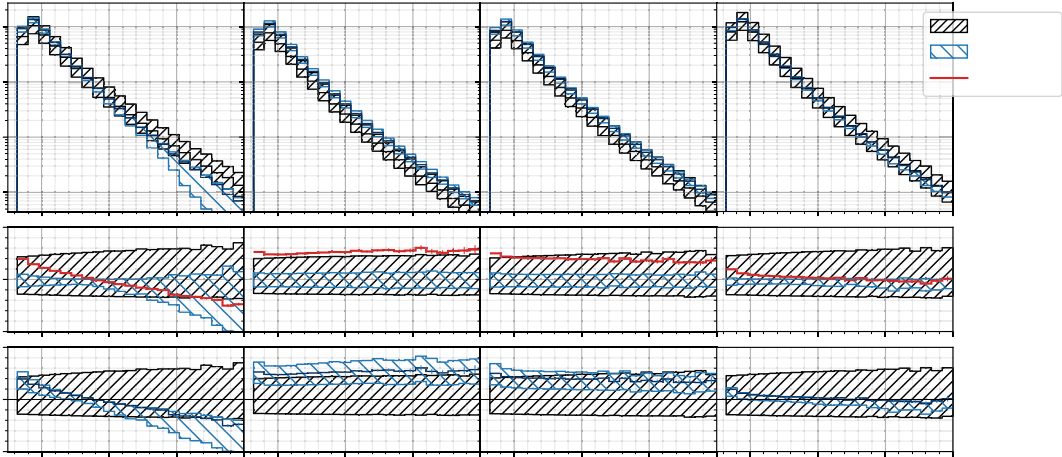


Figure 9. Same as in Fig. 7, but for the $m_{i\bar{i}}$ distribution.

visible, the NLO values going from 40% of the LO values in the region of small $m_{i\bar{i}}$ (large values of s) to 50% in the region of high $m_{i\bar{i}}$. The predictions obtained with the dynamical scale show a much smaller distortion of the central values when going from LO to NLO, while the width of the scale variation bands are quite stable over the whole range of explored $m_{i\bar{i}}$ values.

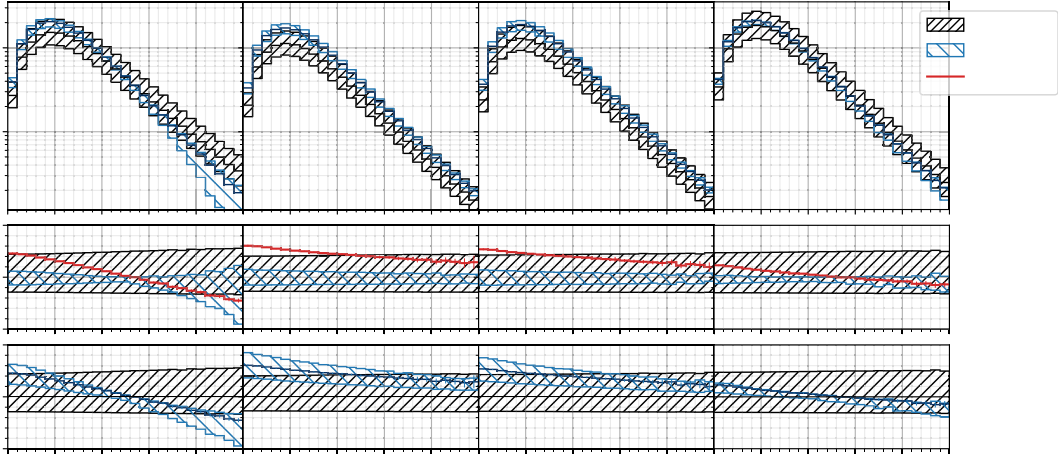


Figure 10. Same as in Fig. 7, but for the p_T^t distribution.

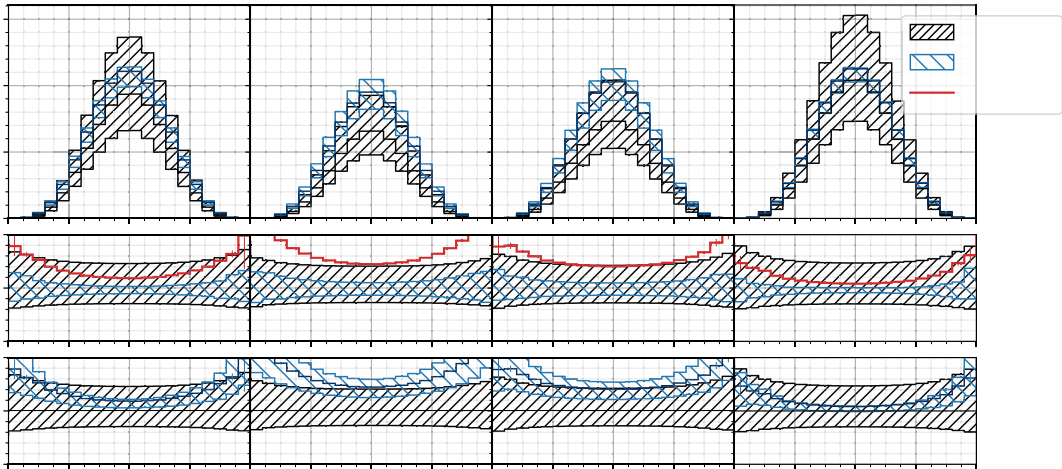


Figure 11. Same as in Fig. 7, but for the y_t distribution.

Similar features as for the behavior of the NLO uncertainty bands can also be observed in e.g. the transverse momentum distribution of the top-quark p_T^t , shown in Fig. 10, although in that case a distortion of NLO predictions with respect to LO ones is present even when using the dynamical scales.

In Fig. 11 the differential cross section is shown as a function of the rapidity of the

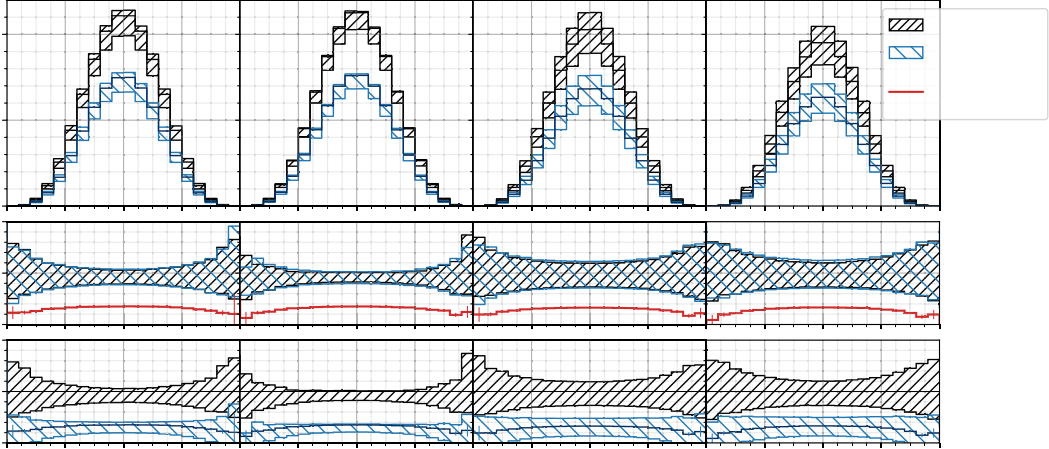


Figure 12. NLO central predictions for the y_t distribution with a p_T^j -analysis cut of 30 GeV (black) and 50 GeV (blue), accompanied by the corresponding seven-point scale variation uncertainty bands, obtained using as a central scale $\mu_0 = m_t$, $H_T^B = 4$, $H_T^B = 2$ and $m_{tj}^B = 2$ (from left to right). In the middle ratio plot the scale variation uncertainty band with either p_T^j -cut is rescaled by the central scale prediction with the same analysis cut. To visualize the difference between the differential cross section obtained with the different p_T^j -cuts the ratio of the central scale predictions is shown in red. In the bottom ratio plot the scale variation uncertainty bands using either analysis cut are rescaled by the central scale result using the requirement $p_T^j = 30$ GeV.

top-quark y_t . The scale variation bands in the static and dynamical scale cases have a more similar width. While using $\mu_0 = H_T^B = 4$ leads to the smallest size of the scale uncertainty band. For the y_t distribution the dynamical scale choice does not lead to an improvement in the stability of the prediction. In fact, as also observed in Ref. [14], the observable y_t receives contributions from all phase-space regions, with most of them from the bulk, where the differences between dynamical and static scales are reduced. The shape of the y_t distribution is almost independent on the p_T^j cut applied in the reconstruction of the hardest jet. This is shown in Fig. 12, where this observable is plotted for two different p_T^j cuts, namely $p_T^j = 30$ GeV and $p_T^j = 50$ GeV. The integrated cross section becomes lower when applying a stronger p_T^j -cut, but the ratio of the distributions $\frac{d}{dy_t} \Big|_{p_T^j = 50 \text{ GeV}}}{\frac{d}{dy_t} \Big|_{p_T^j = 30 \text{ GeV}}}$ is almost uniform, showing that no region in the y_t distribution has a much stronger dependence on this analysis cut compared to the rest of the distribution.

As far as the differential contributions are concerned, the dynamical scale $\mu_0 = H_T^B = 4$ gives in most cases a flat \mathcal{K} -factor close to 1, suggesting that potentially large logarithms are effectively absorbed when adopting this particular choice.

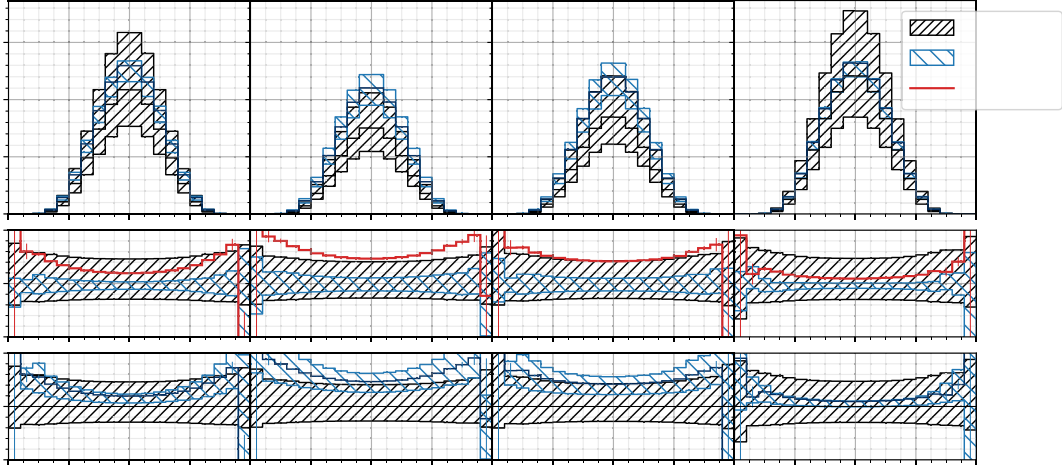


Figure 13. Same as in Fig. 7, but for the $y_{i\bar{i}}$ distribution.

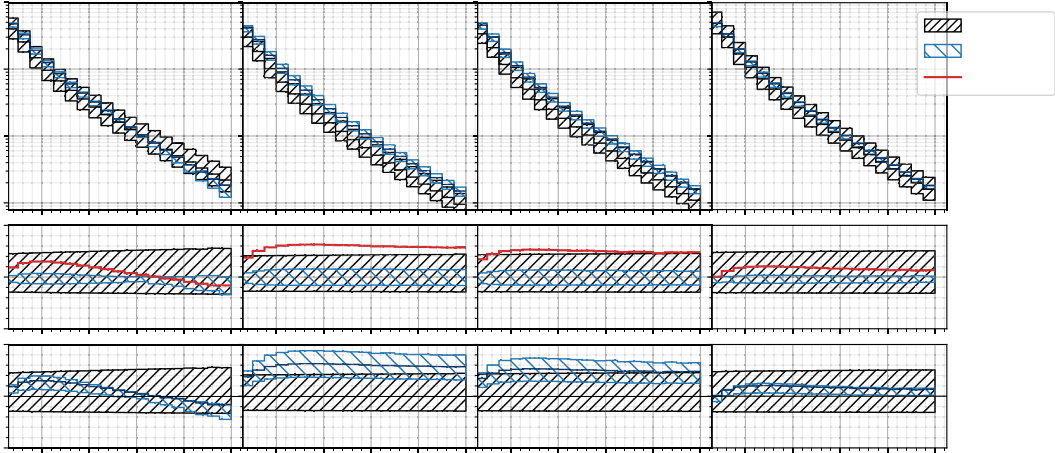


Figure 14. Same as in Fig. 7, but for the p_T^{j1} distribution.

While the two other dynamical scales also show a flat \mathcal{K} -factor for most distributions, the \mathcal{K} -factor value itself is much larger. Uncalculated higher orders could thus be important. This interpretation is supported by the larger scale uncertainty observed for these two dynamical scales. For most distributions using the static scale leads to a \mathcal{K} -factor which depends significantly on the phase space. This is in particular true for the distributions

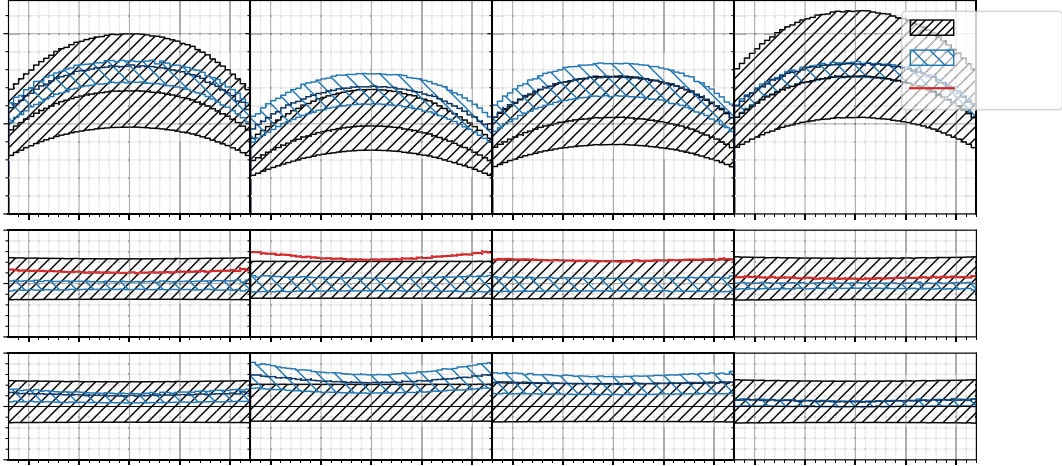


Figure 15. Same as in Fig. 7, but for the j_1 distribution.

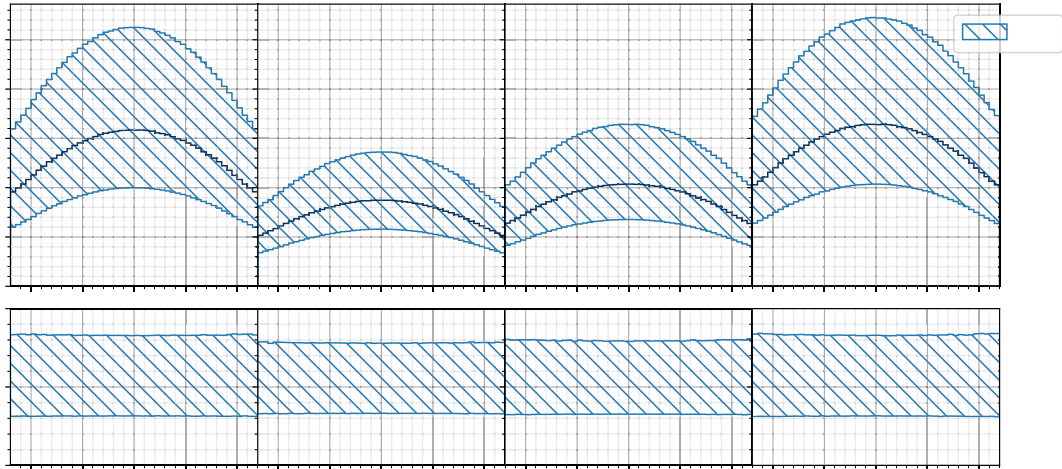


Figure 16. Same as in Fig. 7, but for the j_2 distribution. The content of the panels reflect the fact that the second jet appears for the first time in NLO calculations and, therefore, the accuracy of the predictions for it is limited to LO.

where the individual bins set different energy scales. This is not surprising as a static treatment cannot absorb corresponding logarithms. However, as long as the tails of the distributions are avoided, the static scale choice leads to a smaller \mathcal{K} -factor than the two

dynamical scales $m_{t\bar{t}j}^B/2$ and $H_T^B/2$. We can thus conclude that the static scale is still a reasonable choice for many distributions, at least for the time being. An improved understanding of the perturbative series for the $t\bar{t}j$ process will be possible when higher-order calculations beyond NLO will start to appear.

Since the integrated cross section is dominated by the threshold region, in which the static and dynamical scales $\mu_0 = H_T^B/2$ and $\mu_0 = m_{t\bar{t}j}^B/2$ give similar predictions, no large differences in the size of the scale variation bands of the y_t predictions when using either one or the other scale are expected, as observed in Fig. 11. It can also be seen in Fig. 11 that the LO result varies much stronger going from the static to the dynamical scales, than the NLO result. In the region of large absolute rapidity of the top quark the NLO scale variation band starts to depart from the LO one. This is observed using all four scale choices. The t -channel diagrams contributing in this region lead to final state particles closely following the direction of the initial state particles, such that these final state particles have a large rapidity. Removing the j -cut would result in a t -channel singularity explaining the aforementioned behavior observed at large y_t . In case of $t\bar{t}$ production, and more generally heavy-quark production, this was already investigated in Ref. [60] and [61]. We also observe that similar trends as for the y_t distribution occur even for the $y_{t\bar{t}}$ distribution, plotted for various scale choices in Fig. 13.

Additionally, we looked at the differential distributions of the hardest and second hardest jet. The transverse momentum of the hardest jet is shown in Fig. 14, where the high-energy tail seems again to be better described using a dynamical scale definition, than in case of a static scale. Looking at the pseudorapidity of the hardest jet j_1 and second hardest jet j_2 , a relatively flat differential \mathcal{K} -factor is found using either central scale, comparing Figs. 15 and 16, respectively. Predictions for the second hardest jet are only available in the NLO $t\bar{t}j$ calculation, since at LO only one light parton is present in the final state. As expected from accuracy considerations, these predictions are characterized by larger scale uncertainty bands than those for the first hardest jet. The size of the scale uncertainty bands for the j_2 distribution in Fig. 16 is even larger than the size of the LO scale uncertainty band for j_1 in Fig. 15. As visible in each panel of both figures, for all central scale choices, the size of scale uncertainties accompanying both the j_1 and j_2 distributions does not depend on the pseudorapidity value, i.e. it is uniform, differently from the size of scale uncertainties accompanying the top-quark y_t distribution, which increase at large absolute values of rapidity, as discussed above.

Some of the described differential cross sections were also discussed in Ref. [14], where similar trends were observed, although using more exclusive cuts (and different scales) as mentioned at the beginning of this Section.

3.3 Effects of PDF + $s M_Z$ variation

In this Subsection we discuss the effect of PDF + $s M_Z$ variations. We take as default the CT18 NLO PDF set, with their associated $s M_Z$ value, the latter being subject to two-loop evolution in QCD as provided by the LHAPDF interface. We compute central

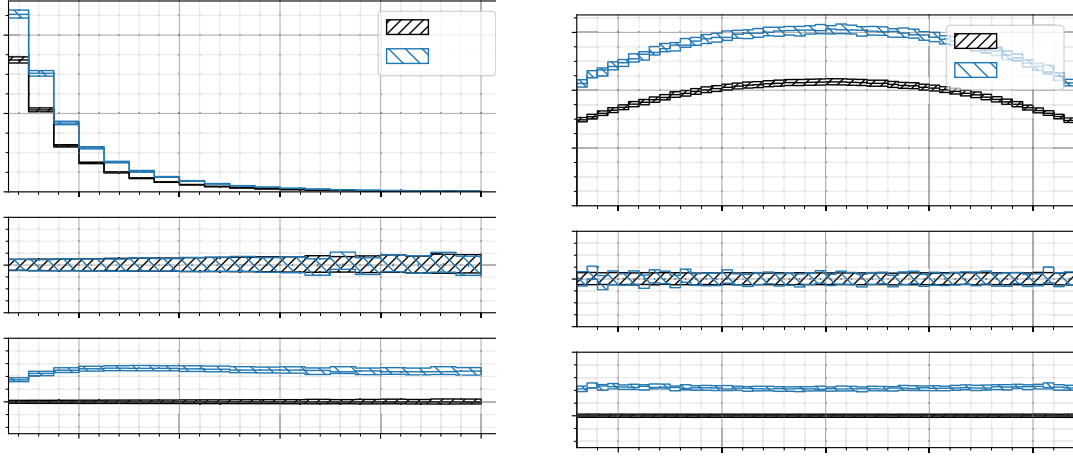


Figure 17. Central predictions for the $p_T^{j_1}$ (left) and y_{j_1} (right) distributions in a full NLO computation (blue) and in a LO computation (black), using as input in both cases the CT18 NLO PDFs + s M_Z value, two-loop evolution of s and the scale $\mu_0 = H_T^B/2$. PDF uncertainty bands computed according to the CT18 prescription and rescaled to the 68% C.L. are also shown.

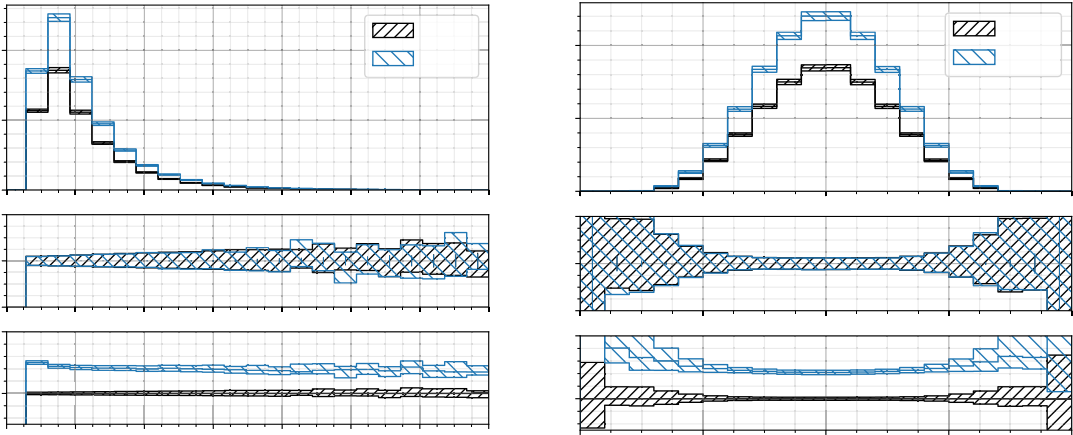


Figure 18. Same as Fig. 17, but for the $m_{l\bar{l}}$ (left) and the $y_{l\bar{l}}$ (right) distributions.

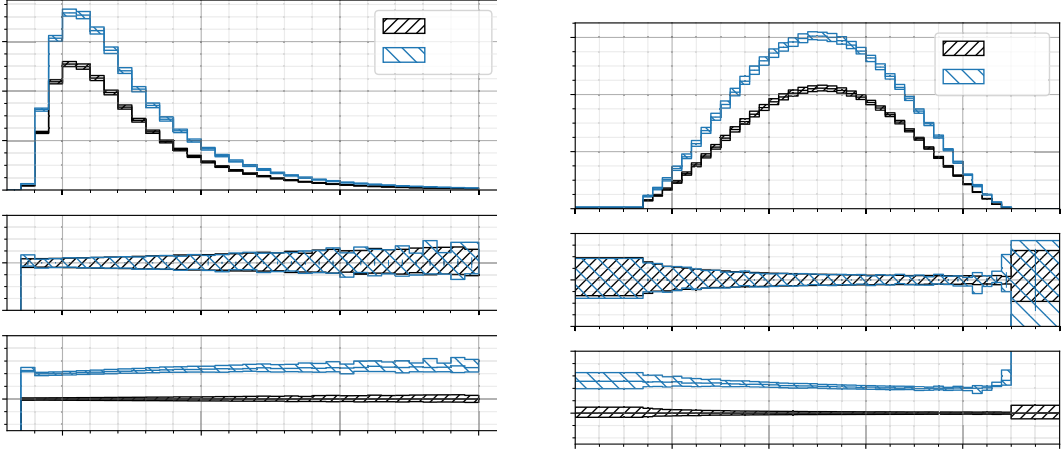


Figure 19. Same as Fig. 17, but for the $m_{i\bar{i}j}$ (left) and the s (right) distributions.

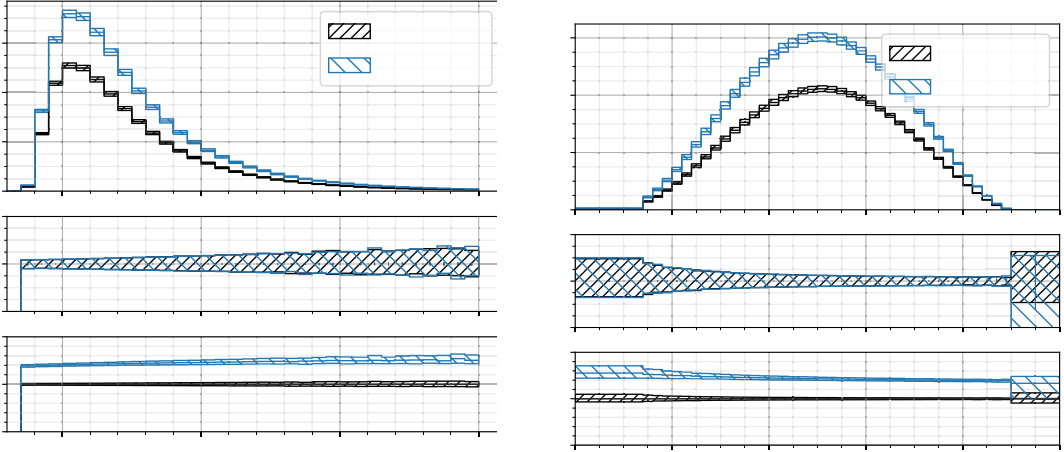


Figure 20. Central predictions for the $m_{i\bar{i}j}$ (left) and s (right) distributions in a LO computation with the scales $\mu_0 = H_T^B/2$ (black) and $\mu_0 = H_T^B/4$ (blue), using as input in both cases the CT18 NLO PDFs + s M_Z value and two-loop evolution of s . PDF uncertainty bands computed according to the CT18 prescription and rescaled to 68% C.L. are also shown.

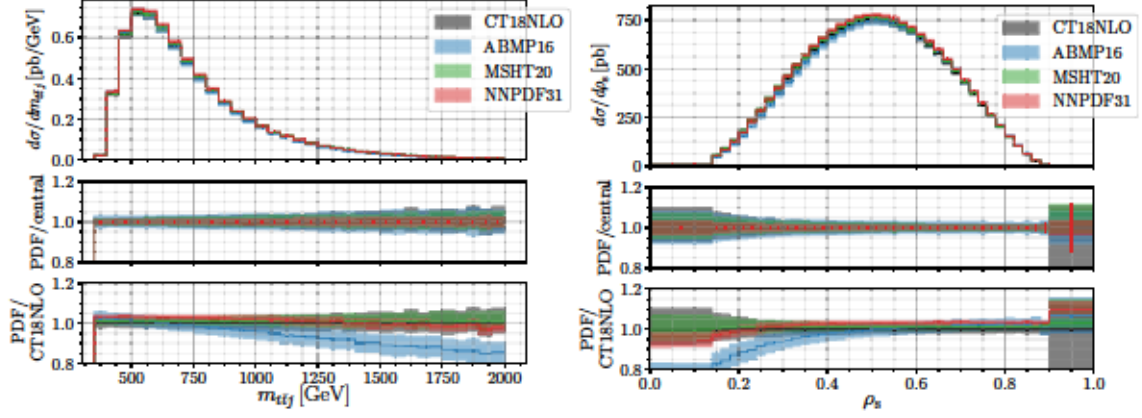


Figure 21. Predictions for the m_{ij} (left) and ρ_s (right) distributions in a LO computation with scale $\mu_0 = H_T^B/4$, including PDF uncertainties of the ABMP16, CT18, MSHT20 and NNPDF3.1 NLO PDF sets. PDF uncertainty bands have been computed according to the prescriptions of the various PDF collaborations, which differ among each other. The CT18 NLO uncertainty band is rescaled to 68% C.L. The $\alpha_s(M_Z)$ value is fixed according to the prescription associated to each PDF set and two-loop α_s evolution is considered. For $\rho_s < 0.85$, corresponding to $m_{ij} > 400$ GeV, the percentage size of the PDF uncertainty band in a full NLO computation would be approximately the same as the one shown in these plots (see also Fig. 19).

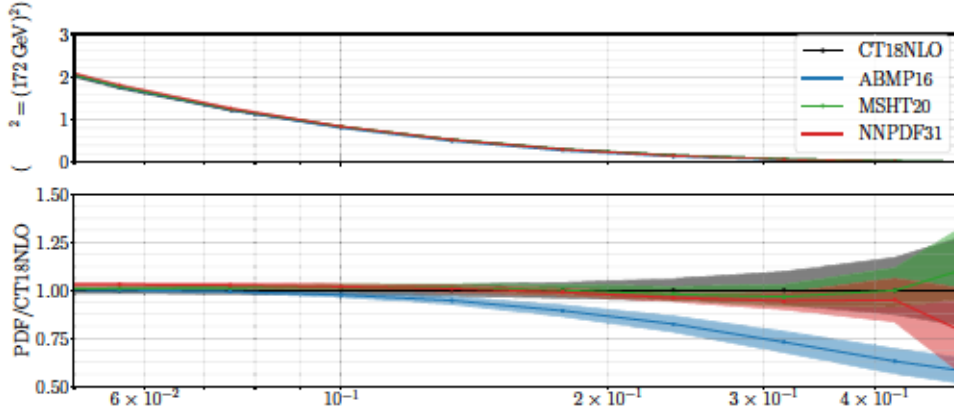


Figure 22. Gluon PDFs obtained with the NLO PDF sets ABMP16, CT18NLO, MSHT20 and NNPDF3.1 as a function of the momentum fraction x for $Q^2 = m_i^2 = (172 \text{ GeV})^2$.

predictions using the set 0 (best fit) and we determine the PDF uncertainty band from the 58 available eigenvectors, according to the prescription provided by the CT18 collaboration⁸. First of all we observe that the relative size of the PDF uncertainty band for many distributions remains approximately the same when making a LO computation with NLO PDFs instead of a full NLO computation. This is shown in Fig. 17 and 18 in case of various

⁸The PDF uncertainties quoted by CT18 denote the 90% confidence level (C.L.) and have to be reduced by a factor of 1.645 for comparison with the 68% C.L. uncertainties quoted by other groups.

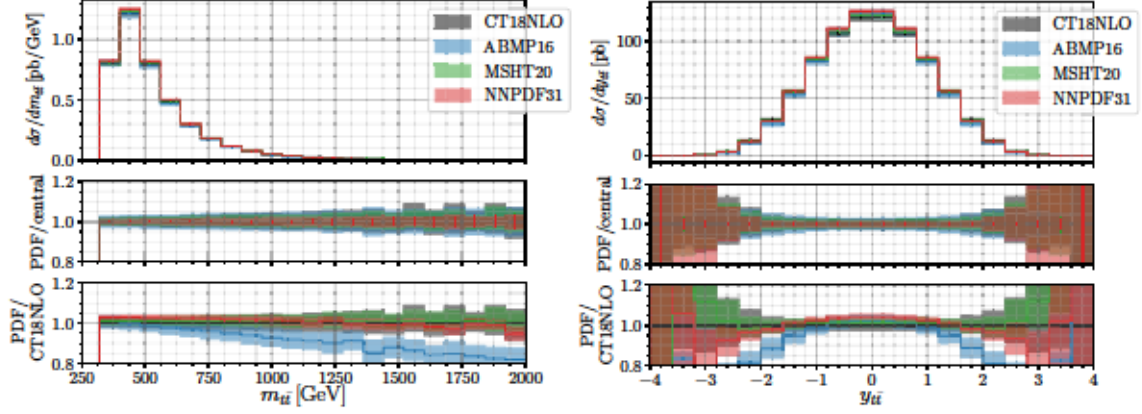


Figure 23. Same as Fig. 21, but for the $m_{i\bar{i}}$ (left) and the $y_{i\bar{i}}$ (right) distributions.

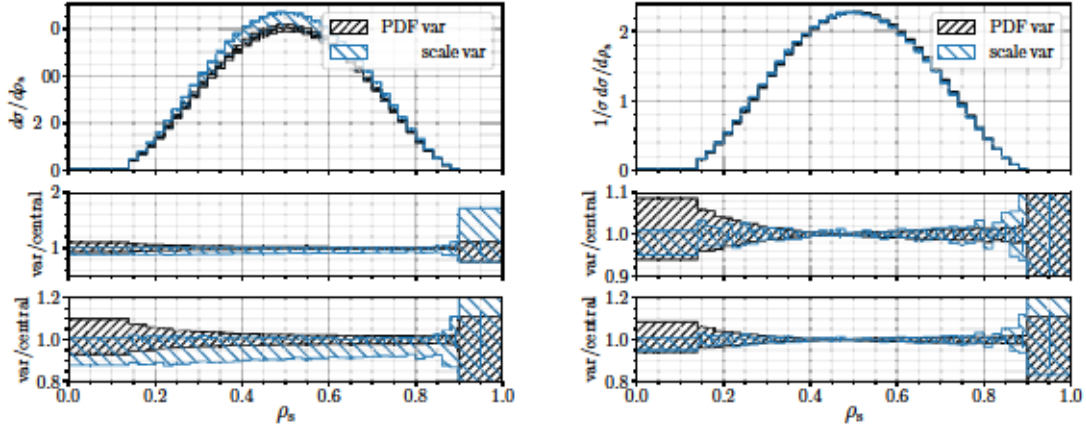


Figure 24. Predictions for the absolute (left) and normalized (right) ρ_s distribution in a LO computation with scale $\mu_0 = H_T^B/4$, including PDF uncertainties computed with the CT18 NLO PDF sets and seven-point scale variation uncertainties. The CT18 NLO uncertainty band is rescaled to 68% C.L. The $\alpha_s(M_Z)$ value is fixed according to the prescription associated to each PDF set and two-loop α_s evolution is considered. The computation of the PDF uncertainty was done by using LO partonic cross sections, while the scale uncertainty was computed with the NLO partonic cross sections.

representative distributions, i.e. $p_T^{j_1}$, y_{j_1} , $m_{i\bar{i}}$ and $y_{i\bar{i}}$, by using the central scale $\mu_0 = H_T^B/2$ for all predictions. This is also true for the $m_{i\bar{i}j}$ and ρ_s distributions for ρ_s values not too large (corresponding to large enough $m_{i\bar{i}j}$ values), as shown in Fig. 19. On the other hand, for very large ρ_s values ($\rho_s > 0.82$), corresponding to small enough $m_{i\bar{i}j}$ (approximately, $m_{i\bar{i}j} < 400$ GeV), the PDF uncertainty band obtained in the LO computation is smaller than the one from the full NLO computation. We observe, however, that the description of this region of phase-space is statistically limited and differences in the PDF uncertainty bands near $\rho_s \simeq 1$, being subject to statistical fluctuations, cannot be reliably predicted with the

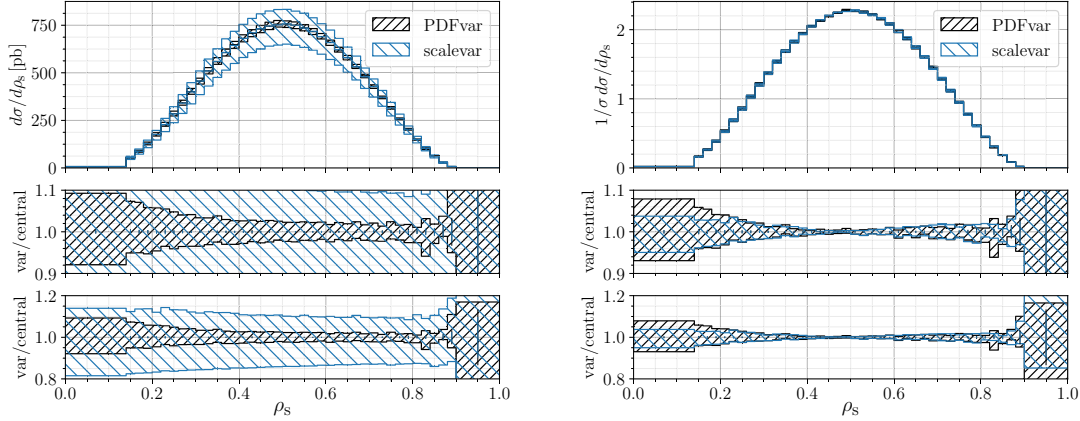


Figure 25. Same as Fig. 24, but for predictions obtained with scale $\mu_0 = H_T^B/2$. In this case both the PDF uncertainty and the scale variation uncertainty were obtained using the NLO partonic cross sections.

limited statistics of our computations. The experimental analyses aiming at the extraction of m_t from the s distribution focus on s values 0.6 - 0.9, avoiding larger values of s close to threshold, for which the statistical uncertainties of the experimental data become large, and improved theory descriptions beyond fixed order might be required. Thus, we conclude that, for the range of s values corresponding to the bulk of the available experimental data, it is possible to determine with good accuracy the relative size of the PDF uncertainty bands by performing LO computations with NLO PDFs.

This is, by far, less CPU intensive than running full NLO computations. Therefore, in the following we use this approximation, applying it in the computation of PDF uncertainties from a range of modern PDF sets, including the ABMP16, CT18, MMHT20 and NNPDF3.1 NLO PDF sets using $\mu_0 = H_T^B/4$. We also observe that, for the range of s values the experimentalists are interested in, PDF uncertainties do not vary in a considerable way when modifying the central scale from $\mu_0 = H_T^B/2$ to $\mu_0 = H_T^B/4$. This is shown for the LO computation with NLO PDFs for the $m_{t\bar{t}j}$ and s distributions in Fig. 20, using as input the CT18 NLO PDFs. Similar considerations are expected to be applicable also for other PDF sets.

With the procedure outlined above we investigated the effect of different PDF sets on the s distribution using as input the scale $\mu_0 = H_T^B/4$. As visible in Fig. 21, in the bulk of the s distribution, the predictions obtained with the aforementioned different PDF + s M_Z sets are in good agreement among each other. On the other hand, in the large s tails, differences are observed, which are not covered by the uncertainties of the involved PDF sets. In order to investigate this aspect further, we show in Fig. 22 the gluon distribution from the considered PDF sets as a function of the longitudinal momentum fraction x retained by the partons from the incoming protons involved in the hard scattering, for

a Q^2 value fixed to $Q^2 = m_t^2 = 172 \text{ GeV}^2$. Looking at the x distributions of the incoming partons for events leading to s values within the smallest bin ($s = 0.014$), we found that the $x_{\min} = \min(x_1, x_2)$ distribution is peaked around $x_{\min} = 0.15$, whereas the $x_{\max} = \max(x_1, x_2)$ one is peaked around $x_{\max} = 0.25$. This is a region where the gluon distributions from different PDF fits differ noticeably among each other. On the other hand, looking at s values in the bulk of the distribution ($s = 0.14$ to 0.65), we found that the x_{\min} and x_{\max} distributions are peaked at $x_{\min} = 0.02$ and $x_{\max} = 0.07$, respectively. In this range of x values, the gluon distributions from different PDF sets are in much better agreement among each other (see again Fig. 22) than in the case of small s . We conclude that, at small s , the sensitivity to large x PDFs, which are not yet very well constrained by the available experimental data, would hamper the possibility of using the s distribution to extract precise values of m_t . On the other hand, for the typical s values considered by the experimentalists to extract m_t , PDF uncertainties are smaller and we expect that the choice of a particular PDF set has a lesser impact on the m_t value extracted from the analysis of the s distribution. In order to use the full s distribution, it is very important that uncertainties on the gluon PDF in the large x tail get reduced. Including already available LHC differential data on bottom hadroproduction in PDF fits could also help constraining large x gluons, as pointed out in Ref. [62], whereas current top-quark hadroproduction data are known to put constraints especially in the region $x = 5 \cdot 10^{-2}$, see, e.g., Ref. [63].

For illustrative purpose, we also show PDF uncertainties on different distributions in Fig. 23. From the left panel, it is evident that considerations similar to those that we discussed in the previous paragraphs for the $m_{t\bar{j}}$ distribution, also apply to the $m_{t\bar{t}}$ distribution, i.e. at large $m_{t\bar{t}}$ values this distribution shows a large sensitivity to large- x gluons. On the other hand, from the $y_{t\bar{t}}$ distribution in the right panel, it is clearly visible how PDF uncertainties blow up for large absolute values of rapidities, corresponding to parton kinematics with more extreme x_1 and x_2 values. Thus, experimental data on these two distributions can be used to further constrain PDF fits, following, for example, the analysis of the CMS collaboration in Ref. [8] based on data for the $t\bar{t}$ normalized multi-differential cross sections, which has also kept the full correlations between the PDFs, s , M_Z and the top-quark mass.

Finally, one can observe that PDF uncertainties are smaller than scale uncertainties when looking at the absolute s distribution, whereas they are similar in size (or even larger at smaller s) when looking at the normalized s distribution, as shown in the left and right panels of Fig. 24, respectively. This conclusion remains valid even when changing the central scale from $\mu_0 = H_T^B/4$ to $\mu_0 = H_T^B/2$, as follows from comparing Figs. 24 and 25. While in the computation using $\mu_0 = H_T^B/4$ only the scale variation uncertainty was computed using the NLO partonic cross sections and the NLO PDF uncertainty approximated, as justified above, with the LO partonic cross sections, in the case of the computation using $\mu_0 = H_T^B/2$ both uncertainties were obtained with the NLO partonic cross sections.

In the following of this Section, we present some further considerations on the joined

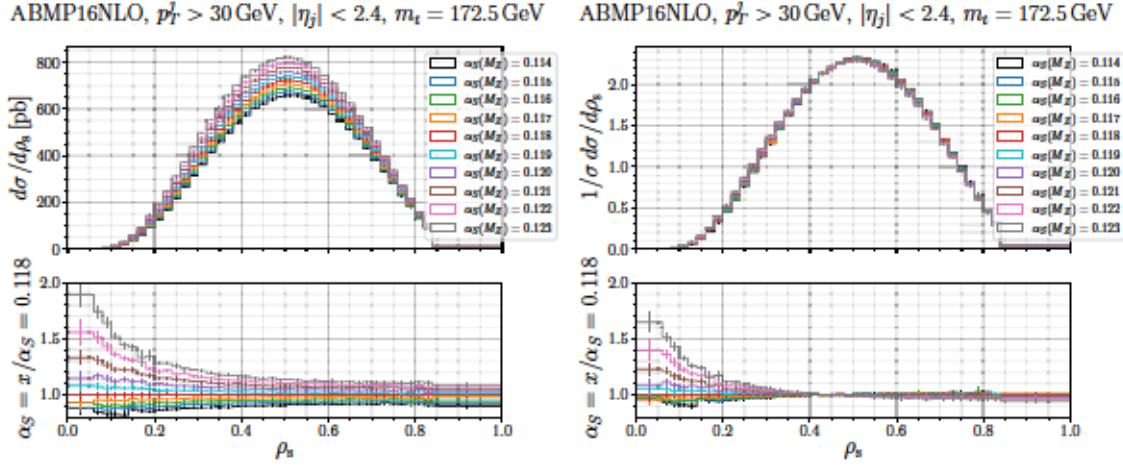


Figure 26. Predictions for the ρ_s (left) and $\mathcal{R}(m_t, \rho_s)$ (right) distributions in a full NLO computation with scale $\mu_0 = H_T^B/2$, using different $\alpha_s(M_Z) + \text{PDF}$ values, as extracted in the NLO ABMP16 $\alpha_s(M_Z) + \text{PDF}$ fits. Two-loop α_s evolution is considered. The top-quark mass value m_t is fixed to 172.5 GeV for all curves. In the lower inset, the ratio of predictions using different $\alpha_s(M_Z) + \text{PDF}$ values with respect to the case where $\alpha_s(M_Z) = 0.118$ is presented.

effect of $\alpha_s(M_Z) + \text{PDF}$ variation, applied to the ρ_s distribution. A more extensive study, that considers the prescriptions and results for α_s variation accompanying the different available PDF fits on a broad number of differential distributions, is beyond the scope of this work. To get a first idea on the main effects of $\alpha_s(M_Z) + \text{PDF}$ variation, and on the size of the differences generated in the ρ_s distribution, we use the different NLO PDF + $\alpha_s(M_Z)$ combinations provided by the ABMP16 collaboration. In particular, the ABMP16 set accounts for the correlations between PDFs and α_s (and heavy-quark masses). This implies that each fit characterized by a different $\alpha_s(M_Z)$ value, with the latter ranging in the interval from 0.114 to 0.123, is also characterized by different PDF values. As shown in the left panel of Fig. 26, the effect appears to be particularly sizable at low ρ_s , i.e. for $\rho_s < 0.2$, where the most extreme $\alpha_s(M_Z) + \text{PDF}$ combinations can produce predictions for the ρ_s distribution which may differ by even a factor of two with respect to the default choice $\alpha_s(M_Z) = 0.118$. Differences are instead much smaller in the ρ_s region currently explored in $t\bar{t}j$ experimental analyses aiming to m_t extraction, where they amount to approximately a maximum of $(-10, +20)\%$. One should also observe that predictions with different $\alpha_s(M_Z) + \text{PDF}$ s do not cross among each other, meaning that the effect of this variation and the corresponding uncertainty on $\mathcal{R}(m_t, \rho_s)$, the variable used in the experimental analyses, is much smaller, as shown in the right panel of Fig. 26. The effect is limited to very few percent in the region of interest for the experimental analyses and becomes increasingly sizable only for $\rho_s < 0.4$, as $\rho_s \rightarrow 0$.

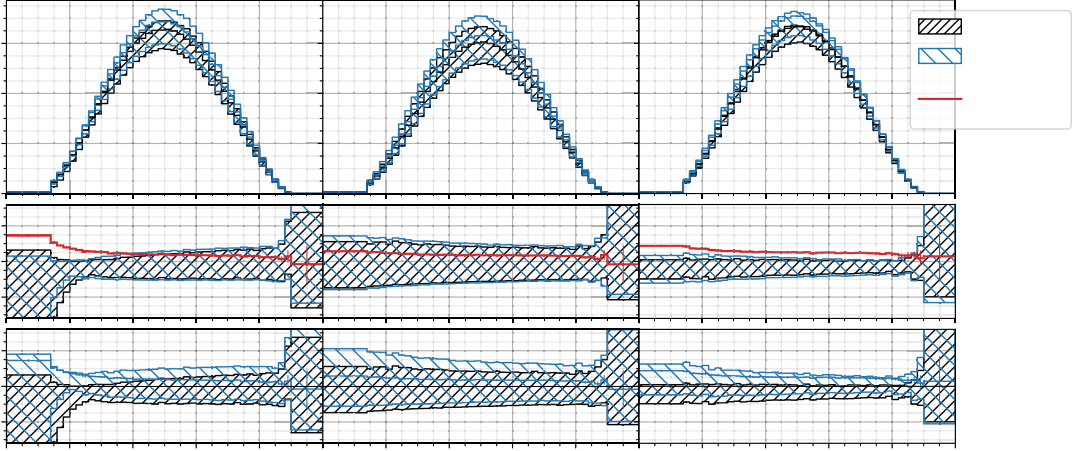


Figure 27. NLO differential cross section as a function of s calculated for the $pp \rightarrow t\bar{t}j + X$ process at $\sqrt{s} = 13$ TeV using the static central scale $\mu_0 = m_t$ (left panel) and the dynamical central scales $\mu_0 = H_T^B/2$ (central panel) and $\mu_0 = H_T^B/4$ (right panel), varying the R -value in the anti- k_T jet clustering algorithm from $R = 0.4$ (black) to $R = 0.8$ (blue). Thereby, besides central predictions, the uncertainty bands due to seven-point scale variation are shown. In the intermediate panel of each plot the relative size of each scale uncertainty band is shown. Thereby the ratio of the central scale prediction obtained with $R = 0.8$ and $R = 0.4$ is also plotted (red line). In the lower panel, all ratios are computed with respect to the central prediction with $R = 0.4$.

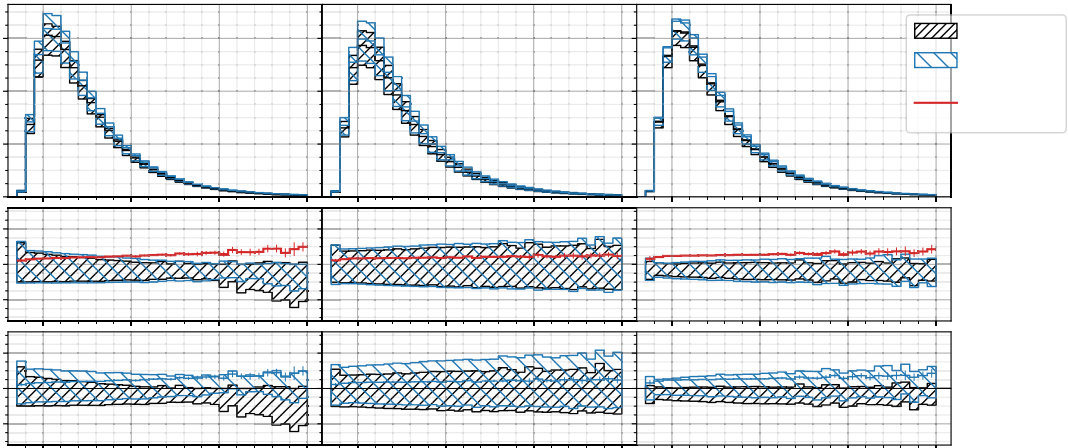


Figure 28. Same as Fig. 27, but for the $m_{t\bar{t}j}$ distribution.

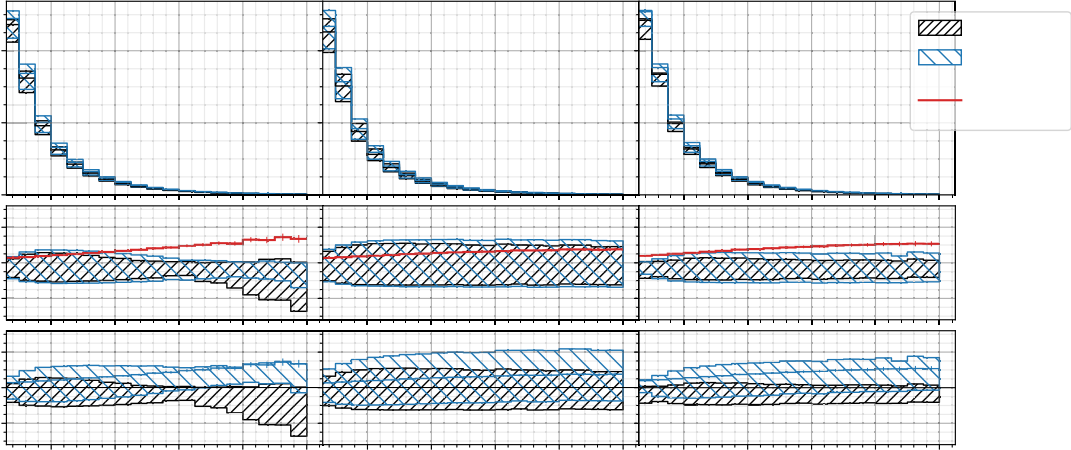


Figure 29. Same as Fig. 27, but for the p_T^j distribution.

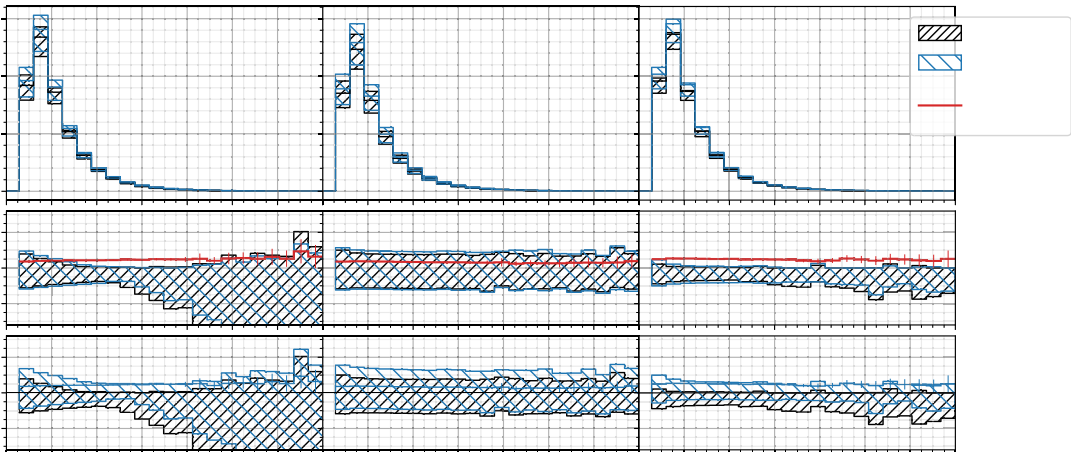


Figure 30. Same as Fig. 27, but for the $m_{l\bar{l}}$ distribution.

3.4 Effects of variation of the R parameter used in jet reconstruction

Additionally we have studied the influence of the variation of the R -parameter of the anti- k_T jet algorithm, on the scale variation uncertainty in the case of the static scale $\mu_0 = m_t$ and the dynamical scales $\mu_0 = H_T^B/2$ and $\mu_0 = H_T^B/4$, which have shown the most preferable behavior among the previously discussed scale choices. The choice of reconstructing jets with the anti- k_T jet algorithm using $R = 0.4$ as default in our work is motivated by the fact that this is the present default choice of both the ATLAS and CMS collaborations. However, the collaborations are also exploring the possibility of larger R values, as needed for a proper assessment of the systematic uncertainties in the experimental analyses. In particular, the case $R = 0.8$ is motivated by the fact that the CMS collaboration includes this value for R in their official jet reconstruction procedure. Therefore, all the calibration and correction factors needed to assess the systematic uncertainties associated to the jet reconstruction are now validated and available for the experimental analysis.

The comparison of the results adopting as input the value $R = 0.4$ (black), already used to obtain the distributions presented in the previous Subsections, and the value $R = 0.8$ (blue), is shown in Fig. 27 for the s distribution. Thereby the fixed central scale $\mu_0 = m_t$ was used to calculate the distributions shown in the left panel, while the central scale definition $\mu_0 = H_T^B/2$ and $\mu_0 = H_T^B/4$ were applied to obtain those in the central and right panels, respectively. For all central scale definitions the differential cross section is larger for larger values of the R -parameter, as expected on the basis of phase-space considerations. The shape of central predictions is also affected, with the $R = 0.8$ choice populating especially the low s (high $m_{t\bar{j}}$) tails. For the considered scale choices, the scale variation uncertainty bands applying either R -parameter value are very similar among each other over the whole range of the distribution, with a slightly reduced size when using $R = 0.4$ with respect to $R = 0.8$. Analogous considerations can be drawn when looking at Figs. 28 and 29, showing the $m_{t\bar{j}}$ and the p_T^{j1} distributions. Our conclusion is that the size of the scale uncertainty bands is almost insensitive to the R variation in the range [0.4 - 0.8]. On the other hand, the effect of a change in the R value on observables which only depend on the top quarks just amounts to a rescaling of the cross section, with no impact on the shape of the corresponding distributions, as shown e.g. in Fig. 30 for the case of the $m_{t\bar{t}}$ distribution.

Reassured by the fact that no significant shape distortion caused by the different value of the jet radius R appears in the NLO distributions we are interested in, we want however to remind the reader that some caution is required when extracting from fixed-order calculations the final physical dependence of the cross section and of inclusive distributions on R . This is due to the fact that the R -dependence of the cross section is not influenced by virtual corrections, but only by the additional real radiation. We thus expect it to display, at the NLO level, an unphysical behavior, in the form of a logarithmic divergence at small R . Only after adding shower and hadronization effects one obtains a more physical

description, usually resulting in an increase of the slope of the R dependence of the $d \sim dR$ cross section, compared to fixed-order calculations. This is a known effect, since hadron formation further randomizes the particles' momenta, driving even more energy out of the cone. It is also known that, on the other hand, the underlying event counteracts the effect of hadronization, since it generates soft hadrons that bring more energy into the jet cone, with a probability proportional to its area.

4 Theoretical predictions for top-quark mass measurements using the \mathcal{R} distribution

Some results for the \mathcal{R} distribution have already been presented in Section 3. However, for systematic extractions of the top-quark mass using as a basis the $t\bar{t}j$ X samples of events collected at the LHC at $\sqrt{S} = 13$ TeV, or future samples at higher center-of-mass energies like e.g. $\sqrt{S} = 14$ TeV, many more predictions are required, using different PDF sets and covering a large top-quark mass range in small mass steps. The purpose of this Section is to provide extensive results which can be used by the ATLAS and CMS experimental collaborations to infer the top-quark mass values in different mass renormalization schemes and allow also to study various systematic uncertainties. In the experimental analyses the binning of the \mathcal{R} distribution has been optimized to minimize systematic and statistical uncertainties. For the exemplary results shown in the following, we use the current binning and analysis setups as provided by ATLAS and CMS. As the analysis setup differs slightly from the one adopted in Section 3, we collect the details in the next Subsection.

4.1 Setup of the calculation

The results presented in Section 4.3 have NLO QCD accuracy, refer to stable top quarks and were obtained by properly extending the framework of Refs. [9, 10], after having verified that, for the case of top-quark mass renormalized in the on-shell scheme, it gives predictions compatible with the POWHEG-BOX implementation used in Section 3, as already discussed there. As in Section 3, the anti- k_T jet algorithm [58], as implemented in FASTJET [59], is used with R set to 0.4 and employing the E -scheme for parton recombination into jets. Additional cuts are applied to the jets as returned by FASTJET. First of all, a minimal transverse momentum p_T^{\min} is required for jet detection. We have produced results for different choices of p_T^{\min} : $p_T^{\min} = 30$ GeV, 50 GeV, 75 GeV, 100 GeV. This set of p_T^{\min} values extends the one considered in Section 3. In addition, in order to be consistent with the most recent experimental setups, we have computed predictions for two different choices of the maximal value of the pseudorapidity η_j : results using $\eta_j = 2.5$ as well as results using $\eta_j = 2.4$ have been produced (in Section 3 only $\eta_j = 2.4$ was used). If more than one jet satisfies these cuts (the top quarks are assumed to be always detected and not passed to the jet-algorithm), the highest energetic jet is used to calculate

For the binning in s we have investigated different choices, as provided by the experiments. In the following, predictions are presented using

$$0 \quad 0.18 \quad 0.22 \quad 0.27 \quad 0.32 \quad 0.38 \quad 0.45 \quad 0.53 \quad 0.62 \quad 0.71 \quad 1$$

for the bin boundaries.

For the hadronic center of mass energies we used both $\sqrt{s} = 13$ TeV and $\sqrt{s} = 14$ TeV, in view of Run 3 and the High Luminosity phase at the LHC. Further predictions for other center-of-mass energies can be provided if required by the experiments.

Despite the slightly enhanced mass sensitivity of the \mathcal{R} distribution compared to the inclusive cross section, the mass effects are still rather small and high precision in the numerical Monte Carlo integration is required to make them visible. For the virtual corrections to the partonic process $gg \rightarrow t\bar{t}g$ additional runs were required to achieve a precision at the sub-percent level in the combined result. To allow interpolations in the mass, results for different top-quark mass values were produced using a step size of 1 GeV.

For the numerical evaluation of the derivative of the leading order cross section required in the conversion to the $\overline{\text{MS}}$ or MSR heavy-quark mass renormalization scheme (see Section 4.2) a step size of 0.5 GeV is used. Employing different methods to calculate the derivative, we have checked that the step size of 0.5 GeV leads to negligible uncertainties for the derivative. As the pole mass m_t and the $\overline{\text{MS}}$ mass $m_t^{\overline{\text{MS}}}$ differ by about 10 GeV (doing the conversion at four loops), we produced results for mass values between 158 and 178 GeV, allowing to cover not only the relevant range in the pole mass but also in the $\overline{\text{MS}}$ and MSR mass. The MSR mass depends on the choice of the R scale. For typical R values between $O(\text{GeV})$ and the $\overline{\text{MS}}$ mass $m_t^{\overline{\text{MS}}}$, the value of the MSR mass lies between the $\overline{\text{MS}}$ mass $m_t^{\overline{\text{MS}}}(R = m_t^{\overline{\text{MS}}})$ and the pole mass ($R = 1$ GeV).

We used the (in alphabetic order) ABMP16_5_nlo [52], CT18NLO [64], MMHT2014-nlo68cl [54], as well as MSHT20nlo_as118 [55], and NNPDF31_nlo_as_0118 [56] PDF sets. The latter two fix $s M_Z$ to 0.118 and in the evaluation of the NLO predictions we have always used the $s M_Z$ value as provided by the corresponding PDF set. In addition, we also produced results always using a same fixed $s M_Z$ value, following the prescription applied in Refs. [9, 10].

4.2 Conversion to the $\overline{\text{MS}}$ and MSR mass scheme

As mentioned before, the \mathcal{R} distribution can also be expressed using renormalization schemes different from the pole mass scheme usually applied. In the following, we briefly describe how the predictions obtained in the pole mass scheme can be translated to the $\overline{\text{MS}}$ or to the MSR mass scheme. We follow the method outlined in Ref. [65] and present only the main steps as the details can be found in Ref. [65]. We start with the discussion of the $\overline{\text{MS}}$ mass. In perturbation theory the pole mass and $\overline{\text{MS}}$ mass are related through a finite renormalization and the mass given in one scheme can be expressed in terms of the mass given in a second scheme. For the concrete case the relation between the top-quark pole

mass m_t and $\overline{\text{MS}}$ mass m_μ reads:

$$m_t = m_\mu \left[1 + c_1 L_M a^{n_f} \mu + c_1 L_M^2 + c_2 L_M a^{n_f} \mu^2 \right] \quad (4.1)$$

with

$$a^{n_f} \mu = \frac{s^{n_f} \mu}{m_t^2} \quad \text{and} \quad L_M = \ln \frac{\mu^2}{m_t^2} \quad (4.2)$$

The coefficients c_i are known up to four-loop order [66] and can be found conveniently collected for example in Ref. [67, 68]. At NLO accuracy only c_1 is required which reads:

$$c_1 L = \frac{4}{3} L \quad (4.3)$$

At the order we are working, L_M can be replaced with $L_M = \ln \frac{\mu^2}{m_\mu^2}$. The difference between using m_μ or m_t is of higher order in the coupling constant and does not contribute at the order we are working here. Using in addition m_μ instead of m_μ leads to $L_M = 0$. In Refs. [9, 10] the top-quark loops in the gluon self energy are subtracted at finite momentum. At NLO accuracy the strong coupling defined in this way is equivalent to $s^{n_f-1} \mu$, i.e. s renormalized in the $\overline{\text{MS}}$ scheme with $n_f - 1$ active flavors. Note that all quarks except the top one are treated as massless. As the difference between $s^{n_f} \mu$ and $s^{n_f-1} \mu$ is of order $s^{n_f-1} \mu^2$, one finally obtains

$$m_t = m_\mu \left[1 + c_1 \left(\frac{s^{n_f-1} \mu}{m_\mu} \right) + \dots \right] \quad (4.4)$$

Starting with the perturbative expansion of the cross section using the pole mass

$$a^5 \mu^3 \sigma_0(m_t) = a^5 \mu^4 \sigma_1(m_t) \quad (4.5)$$

where we have set $n_f = 6$, and using the above relation between m_t and m_μ , one obtains after expanding in s

$$a^5 \mu^3 \sigma_0(m_\mu) = a^5 \mu^4 \sigma_1(m_\mu) + c_1 \left(\frac{d \sigma_0}{d m_t} \right)_{m_t = m_\mu} m_\mu \quad (4.6)$$

We note that this formula can be applied to the inclusive cross section but also to individual bins of differential distributions.

The definition of the MSR mass [6, 7] employs the fact that the $\overline{\text{MS}}$ mass is free of renormalon ambiguities and that the renormalon ambiguity does not depend on the mass of the heavy quark. Accordingly the MSR mass is defined through

$$m_{\text{MSR}} = m_t \left[R + d_1 \left(\frac{s^{n_f}}{R} \right) + d_2 \left(\frac{s^{n_f}}{R} \right)^2 \right] \quad (4.7)$$

with the expansion coefficients d_i implicitly given by

$$m_t = m \left(1 + d_1 \frac{a^{n_f}}{m} + d_2 \frac{a^{n_f}}{m^2} + \dots \right)$$

Note that the coefficients d_i can be expressed in terms of the c_i introduced above, e.g. $d_1 = -c_1$. Using again $a^{n_f-1} R$ instead of $a^{n_f} R$ and expressing the cross section in terms of the MSR mass leads to

$$\sigma = \mu^3 \left(1 + c_1 \frac{a^{n_f}}{m_{\text{MSRp}}} + \dots \right) \frac{d^0}{dm_t} \left(\frac{m_t}{m_{\text{MSRp}}} \right) R \quad (4.8)$$

We note that there are two variants of the MSR scheme, leading respectively to the *natural* MSR mass and the *practical* MSR mass, differing according to the way the transition from n_f active flavors to $n_f - 1$ active flavors is done. Expressing μ^{n_f} in terms of μ^{n_f-1} corresponds to the practical MSR mass scheme. This is indicated by the additional “p” in the subscript of the MSR mass m_{MSRp} . For the present application, the difference between the natural and the practical scheme is negligible, as has been shown in Refs. [7, 69, 70].

Using Eqs. (4.6) and (4.8) it is straightforward to convert the results using the pole mass scheme into the $\overline{\text{MS}}$ or MSR scheme.

4.3 Exemplary results for the \mathcal{R} distribution using different parton distribution function sets and different renormalization schemes

In this Section we provide theoretical predictions using the setup described above. The results allow for top-quark mass determinations from the measured \mathcal{R} distribution. Fig. 31 gives an overview of the different settings used in the calculation. In addition, we have

PDF sets	Mass renormalization	p^{cut}	Pseudo rapidity cut
ABMP16	pole mass scheme	$p^{\text{cut}} = 30 \text{ GeV}$	2.4
CT18NLO	$\overline{\text{MS}}$ mass scheme	$p^{\text{cut}} = 50 \text{ GeV}$	2.5
MMHT14	MSRp mass scheme	$p^{\text{cut}} = 75 \text{ GeV}$	
MSHT20		$p^{\text{cut}} = 100 \text{ GeV}$	
NNPDF3.1			

Figure 31. Overview of the different settings used as input in the calculation.

considered different bin choices. Here we only show selected results. Some reference cross sections are collected in the Appendix A and the complete set of predictions is available online at [71].

The first three panels of Fig. 32 show the \mathcal{R} distribution using different schemes for renormalizing the top-quark mass: the on-shell scheme, the $\overline{\text{MS}}$ scheme, as well as the

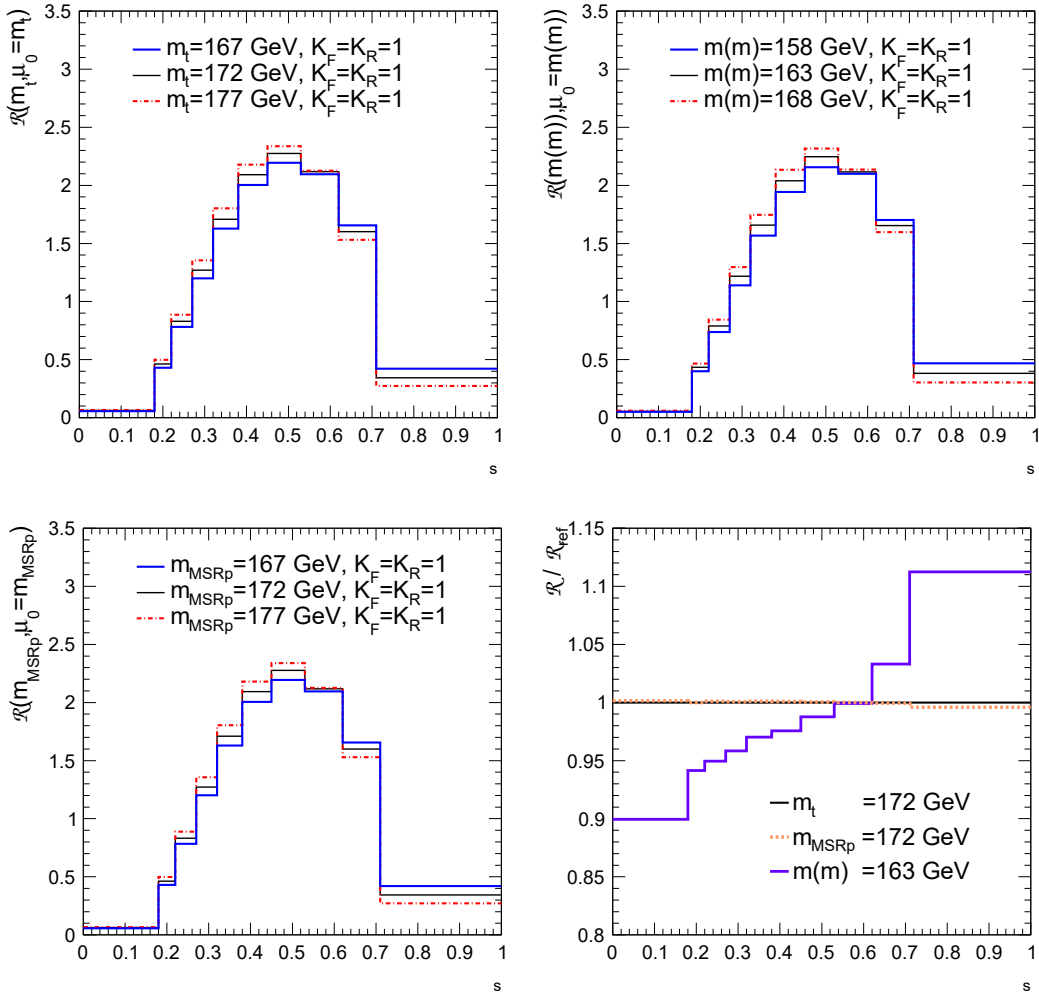


Figure 32. \mathcal{R} distribution using different renormalization schemes for the top-quark mass, i.e. the pole mass m_t , the $\overline{\text{MS}}$ mass $m(m)$ and the MSR mass m_{MSRp} . Different lines correspond to different input masses, implying different choices for the renormalization and the factorization scales (assumed to be equal). In the last panel, ratios of predictions with the $m(m)$ and m_{MSRp} masses with respect to predictions with the on-shell mass are shown. The central CT18NLO PDF set is used as input in all panels.

MSR scheme. In each panel, the \mathcal{R} distribution is depicted for a central mass value together with the variation by ± 5 GeV. We fix the renormalization and factorization scale to $\mu_F = \mu_R = m$, where m is the top-quark mass in the considered scheme. The central mass values in the three different schemes are chosen such that they roughly correspond to each other after doing the conversion at 4-loop accuracy. As we used a step size of 1 GeV for the masses in the calculation, this correspondence is obviously not exact. Although small, the effect of mass variation on the \mathcal{R} distribution is clearly visible within each of the three considered schemes. In the fourth plot in Fig. 32, we show the predic-

tions using the $\overline{\text{MS}}$ and MSR masses divided by the predictions obtained in the pole mass scheme. The MSR masses were computed at a scale $R = 3 \text{ GeV}$. Note that because of the aforementioned step size of 1 GeV we do not expect perfect agreement. The predictions using either the pole mass or the MSR mass agree with each other. However, a sizeable difference is observed using the $\overline{\text{MS}}$ mass. This is a consequence of the large impact of the NNLO and N³LO corrections in the conversion formulas. Using an $\overline{\text{MS}}$ mass value of 165 GeV, which is close to the value obtained using the one-loop conversion formula, the agreement is much better, as expected. The corresponding ratio plot is shown in Fig. 33. In

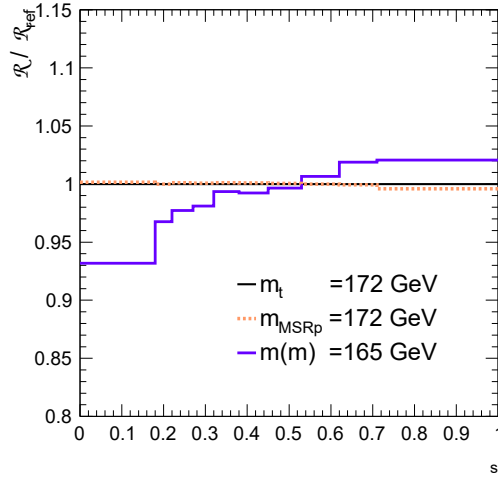


Figure 33. Ratio of \mathcal{R} in the $\overline{\text{MS}}$ and MSR scheme to \mathcal{R}_{ref} in the pole scheme, similar to the fourth plot in Fig. 32, however using $m = 165 \text{ GeV}$ instead of 163 GeV.

Fig. 34 we show the \mathcal{R} distribution for different PDF choices divided by the results for the CT18NLO set. Apart from the first bin, where the differences are larger, the CT18NLO, MMHT14-nlo68cl, MSHT20nlo_as118 and NNPDF3.1_nlo_as_0118 central PDF sets give similar results at the level of a few percent. We note that in all results shown in Fig. 34 the s M_Z value and evolution is used as provided by the PDF set. The differences in the first bin which corresponds to high energetic events and is thus sensitive to the large x values of the PDFs is irrelevant for practical applications due to the small number of high energetic events. The ABMP16_5_nlo PDF set shows slightly larger deviations reaching up to 5% if one excludes the three highest energetic bins ($s = 0-3$). In Fig. 35 we show the scale dependence of the \mathcal{R} distribution using different renormalization schemes for the top-quark mass. We used $\mu_F = \mu_R = \mu_0$ together with $\mu_0 = m, m/2, 2m$, where m denotes the respective mass. For the pole mass and the MSR mass the behavior is very similar. A major difference is only observed in the highest energetic bin, where the MSR mass leads to a larger scale dependence of the \mathcal{R} distribution. Again this is most likely of no practical relevance. In case of the MSR mass one could use a larger value for the R -scale bringing the MSR mass closer to the $\overline{\text{MS}}$

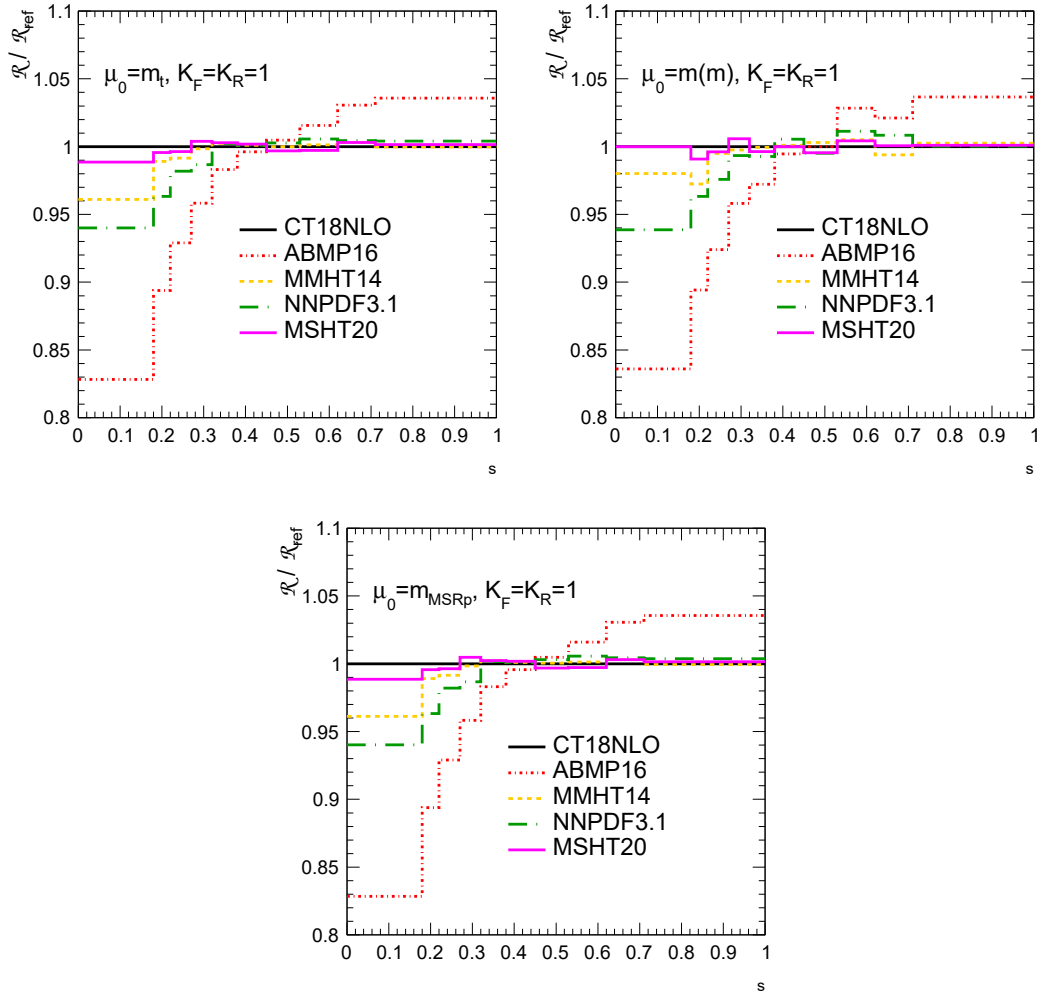


Figure 34. \mathcal{R} distribution using different PDF sets. We chose again $\mu_F = \mu_R = \mu_0$ where μ_0 is set equal to the respective mass value.

mass suggests that in this case the scale variation would become even larger. In the range $0.2 < s < 0.7$ the scale variation band using the $\overline{\text{MS}}$ mass is similar to the one obtained by working in the pole- and the MSR-scheme. However, in the bin close to the threshold one obtains very large scale variation effects using the $\overline{\text{MS}}$ mass. The origin of this effect is the strong mass dependence in the threshold region which leads to large contribution when using Eq. (4.6) to convert from the pole mass to the $\overline{\text{MS}}$ mass. Fig. 36 is similar to Fig. 32 using however a step size of 1 GeV instead of 5 GeV. From the approximately constant step size one can see that in all bins the mass dependence is to good approximation linear, allowing a linear interpolation when performing a χ^2 fit to determine the top-quark mass from the measured distributions.

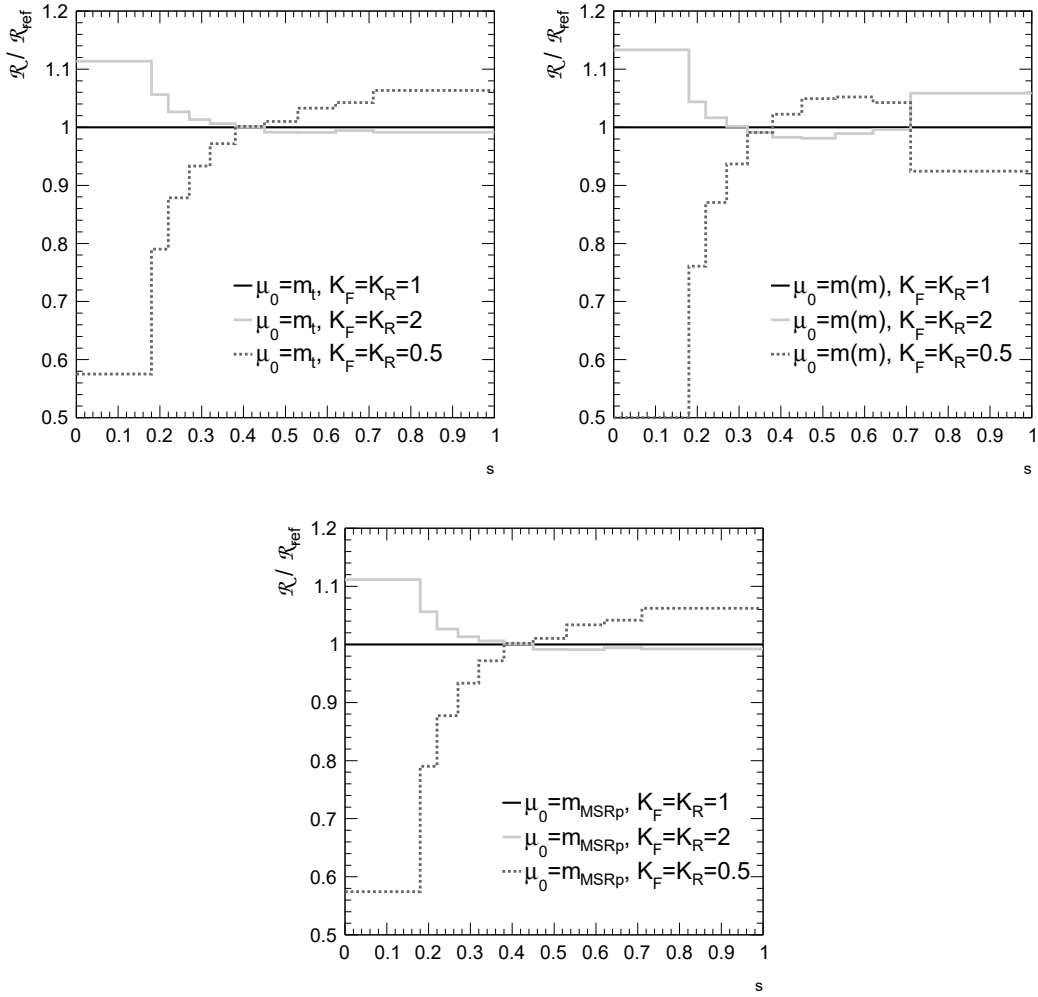


Figure 35. Ratios of \mathcal{R} distributions using different scale choices, i.e. $\mu_R = K_R \mu_0$, $\mu_F = K_F \mu_0$ with $\mu_0 = m$ and $K_F = K_R = 0.5, 1, 2$. Different panels refer to different renormalization schemes for the top-quark mass, i.e. the pole scheme (upper left), the $\overline{\text{MS}}$ scheme (upper right) and the MSR one (lower).

4.4 Off-shell effects and non-resonant/non-factorizable contributions

As mentioned already, the results presented in previous Sections can only be compared with data which have been unfolded to the *parton level*. The unfolding procedure accounts for effects due to the top-quark decay, additional gluon radiation from top-quark decay products as well as hadronization and experimental detector effects. Unfolding is a well established method and has been applied in the past to a variety of different observables. Obviously the unfolding procedure introduces additional uncertainties which need to be taken into account. In Ref. [72] an alternative approach has been investigated. Instead of unfolding the measured data to the level of the intermediate top quarks, the observable is

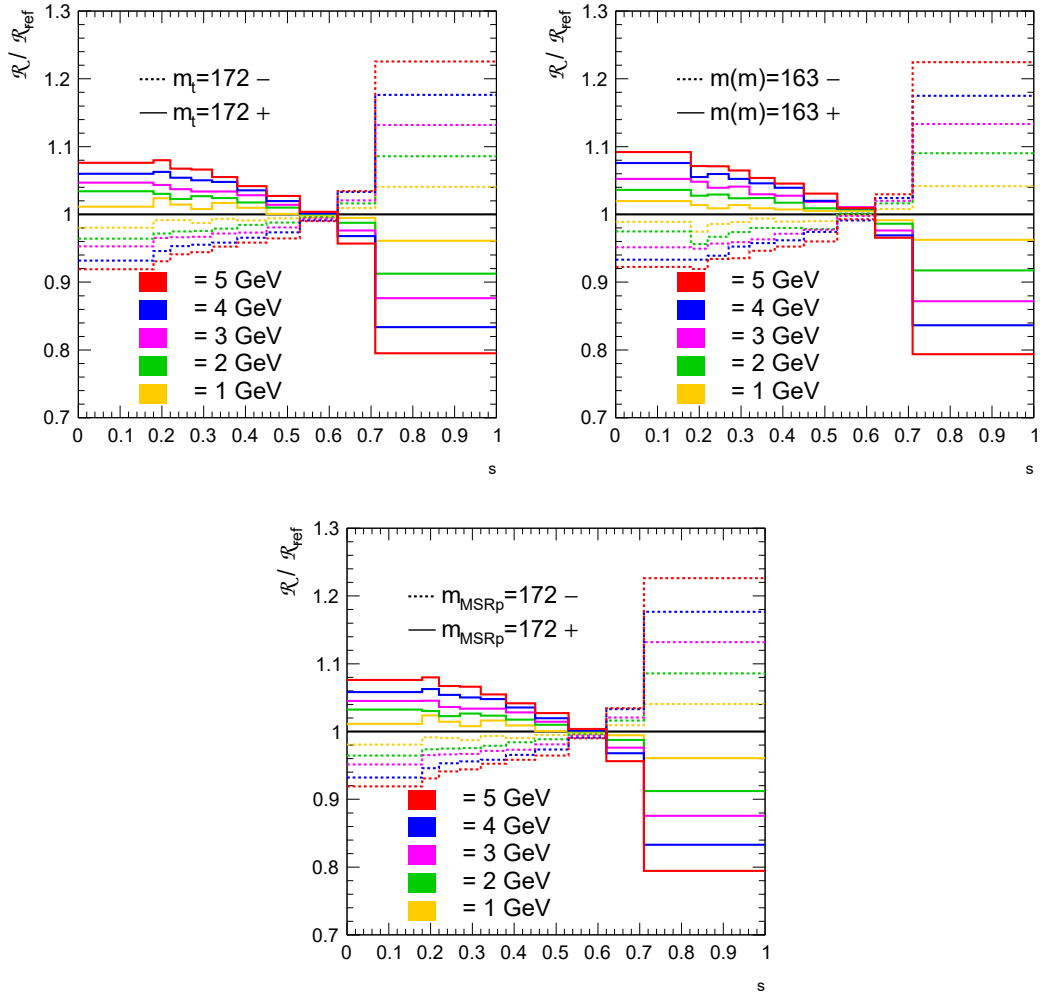


Figure 36. Ratios of \mathcal{R} distributions using as input different top-quark mass values and the \mathcal{R} distribution obtained with a fixed central top-quark mass value (assumed to be equal to 173 GeV in all renormalization schemes). Different panels refer to different renormalization schemes for the top-quark mass.

computed using the momenta of the final state particles in $pp \rightarrow e^+ e^- \mu^+ \mu^- b \bar{b} j + X$ events, which is a typical final state for $t\bar{t}j + X$ assuming that both the top and antitop quarks decay leptonically. In principle, this allows to incorporate some of the aforementioned effects like the top-quark decay or radiation from top-quark decay products into the theoretical prediction instead of modeling them with Monte Carlo (MC) programs. In particular, spin effects like for example spin correlations are automatically taken into account and passed on to the top-quark decay products. To compare with the results of Ref. [72] we consider *parton level with decay* of the top quarks instead of using the intermediate top quarks to define the final state.

An expected advantage of using the results of Ref. [72] is that unfolding uncertainties

should be reduced as less modeling is introduced in the partonic description. The calculation in Ref. [72] was performed at NLO accuracy in QCD keeping not only finite width effects for the top quark but also the corresponding effects for the intermediate W -bosons. Furthermore, non-resonant/non-factorizable contributions were also included in the prediction. The theoretical description thus includes many physical effects. In the following we will refer to it as *full calculation (Full NLO)*. However, this calculation has not yet been matched to a parton shower, therefore shower effects are not presently accounted for, and hadronization and further soft physics effects are also absent. In addition, two further approximations to model off-shell effects are studied in Ref. [72]. First, the approximation in which the two decay chains

$$pp \rightarrow t\bar{t}j + X \rightarrow e^+e^-\mu^+\mu^-b\bar{b}j + X \quad pp \rightarrow t\bar{t} \rightarrow e^+e^-\mu^+\mu^-b\bar{b}j + X$$

are calculated in the narrow width approximation, called *NWA* in Ref. [72]. The production cross sections as well as the decay is calculated at NLO accuracy. This approach thus includes spin effects while non-resonant/non-factorizable contributions are neglected. Please note that one should not naively think that these chains are calculated separately and added together, as this would lead to a double counting. Ref. [12], on which the discussion in Ref. [72] relies, first classifies the corrections depending on whether the additional jet is radiated in the top-quark pair production phase or from the top-quark decay products. Then it incorporates radiative corrections in a consistent way. While some contributions may be attributed to either one or the other aforementioned production chain, considered as standalone, Ref. [12] also includes mixed contributions leading to a much more complex picture than adding the chains would suggest, avoiding double counting without the need of a merging prescription. In a second approximation which is called *NWA_{Prod}* in Ref. [72], the process $pp \rightarrow t\bar{t}j + X$ at NLO QCD accuracy is combined with the leading-order decay of the top quarks following the approach presented in Ref. [11]. It should be stressed that neither the *full* calculation nor the two approximations include parton-shower effects. In Ref. [72] it has been argued, that employing the aforementioned different theoretical prescriptions can lead to significant differences in the extracted mass values. However, the interpretation of these results need further clarifications and the significance of the observed mass shift remains unclear as no uncertainty was calculated for it. Furthermore, in the analysis different scale settings were applied. While for the full calculation a dynamical scale (H_T) was used, a static scale with $\mu_R = \mu_F = m_t$ was used for the *NWA* and *NWA_{Prod}* approximations. It is well known [1, 2, 73] that scale variations can lead to sizable effects on the extracted top-quark mass. In addition, the findings of Ref. [72] are not directly applicable to the experimental analyses as the experimental approach taken by ATLAS and CMS is rather different from the procedure applied in Ref. [72]. In the experimental analysis the unfolding is done to the level of stable tops. Gluon emission from top-quark decay products is thus accounted for through the unfolding. In this work we argue that in fact the bulk of the effects leading to the aforementioned shift is, within the uncertainties associated to the modeling of the partonic sub-processes and the hadronization, well

described by MC tools, and is thus taken into account doing a proper unfolding as it is done in the analyses performed by ATLAS and CMS. To show this explicitly, the results of Ref. [72] are compared with a Monte Carlo simulation including NLO QCD corrections in the production. More precisely, events for the process $pp \rightarrow t\bar{t}j + W + W + b\bar{b}j$ are generated through a MC simulation, using the parameters shown in Tab. 2 matching those used in Ref. [72]. Top quarks are produced on-shell in association with an extra jet at NLO

Parameter	Value
$s M_Z$	0.118
G_μ	$1.6637 \cdot 10^{-5} \text{ GeV}^{-2}$
M_Z	91.1876 GeV
M_W	80.3990 GeV
Γ_Z	2.50848 GeV
Γ_W	2.09875 GeV

Table 2. Parameters used in the Monte Carlo generation of $pp \rightarrow t\bar{t}j + W + W + b\bar{b}j$. The electromagnetic coupling α_s and the weak mixing angle $\sin^2 \theta_w$ are computed in the G_μ scheme using $\alpha_s = 1 - \frac{M_W^2}{M_Z^2}$ and $\sin^2 \theta_w = \frac{1}{2} G_\mu \frac{M_W^2}{M_Z^2} \frac{M_Z^2 - M_W^2}{M_Z^2}$, where M_Z and M_W are the gauge boson masses and G_μ denotes the Fermi constant. The decay widths of the massive gauge bosons are defined as Γ_W and Γ_Z .

in QCD, using the ttj package in the POWHEG-BOX [32, 33, 36, 39], with the CT14nlo PDFs [74] and the μ_F and μ_R scales fixed to the value of the top-quark mass m_t , renormalized in the on-shell scheme. The POWHEG-BOX code is interfaced to the PYTHIA8 [37] code which simulates the parton showering beyond first radiation emission and the top-quark decay. Spin correlations could be included via the POWHEG-BOX. However, in this case also the decay of the top quarks would be handled by the POWHEG-BOX. As the distribution we are interested in is not particularly sensitive to the decay, we simplify the approach by allowing PYTHIA8 to do the top-quark decay, without any specific optimization or modification of its decay routines. The top quark is decayed into an on-shell W -boson and a b -quark, with decay width $\Gamma_t^{\text{on-shell}} = 1.37 \text{ GeV}$ for a top-quark pole mass value amounting to $m_t = 173.2 \text{ GeV}$ [73, 75]. The lighter quarks are considered massless. Only leptonic decays of the W -bosons are included in the simulation. No special settings have been used in the simulation with PYTHIA. The leptons are further restricted to electrons and muons, i.e. W -bosons decaying into neutrinos are excluded. The MC simulation is stopped before hadronization occurs and the objects entering the analysis as well as the fiducial volume are defined as in Ref. [72], in order to make the comparison between the two approaches as close as possible.

All the final-state partons with pseudorapidity $|\eta| < 5$ are recombined into jets using the anti- k_T algorithm [58] with radius parameter $R = 0.5$. Jets are required to have a transverse momentum p_T^j larger than 40 GeV, absolute pseudorapidity $|\eta_j|$ smaller than 2.5, and an angular separation satisfying $R_{j_1 j_2} = \frac{\sqrt{(y_{j_1} - y_{j_2})^2 + (\phi_{j_1} - \phi_{j_2})^2}}{\min(p_{T,j_1}, p_{T,j_2})} > 0.5$. A jet is

called b -jet if it originated from a b -quark. Charged leptons are defined by recombining electrons or muons with photons via the anti- k_T algorithm with $R = 0.1$. Only leptons with $p_T \geq 30$ GeV and $|\eta| \leq 2.5$ are considered. Charged leptons are also required to be well separated from other leptons ($R_{ll} = 0.4$) and from jets ($R_{lj} = 0.4$). The four momenta of the neutrinos are summed together into a missing momentum vector p^{miss} . Only events with two b -jets, at least one light jet⁹, two oppositely charged leptons and $p_T^{\text{miss}} \geq 40$ GeV are accepted. These cuts match precisely the ones used in Ref. [72]. Events passing these cuts are used to calculate the \mathcal{R} distribution. The quantity $s_{i\bar{j}}$ is calculated using

$$s_{i\bar{j}} = (p_{j_{b1}} + p_{j_{b2}} + p_{\text{light}} + p_{\text{miss}})^2$$

In Fig. 37 the \mathcal{R} distribution obtained from the MC simulation ($\mathcal{R}^{\text{POWHEG-BOX + PYTHIA8}}$) is presented and compared to the result $\mathcal{R}^{\text{Full}}$ obtained in Ref. [72]. For these computations PYTHIA8 (version 8.1.5.0) has been used. Furthermore, the top-quark mass used in PYTHIA8 is set equal to the mass used in POWHEG-BOX. Both distributions have been generated using the same top-quark mass $m_t = 173.2$ GeV. In the POWHEG-BOX + PYTHIA8 computation we set the factorization and renormalization scale to $\mu_R = \mu_F = m_t$. From the differences in terms of the total statistical uncertainty (lower plots in Fig. 37) one concludes that the two calculations give consistent results within the uncertainty. Already at this point one would expect similar top-quark mass values treating the simulated events as pseudo-data and using either Ref. [72] or POWHEG-BOX + PYTHIA8 to extract the corresponding top-quark mass. To turn this qualitative statement into a quantitative one, we have set up a χ^2 minimization test to infer the m_t values and quantify the difference using either Ref. [72] or POWHEG-BOX + PYTHIA8 as pseudo-data. To do so we generated MC event samples using top-quark masses ranging from 165 GeV to 180 GeV using again the input parameters quoted in Tab. 2. For each mass value the corresponding event sample is used to determine the \mathcal{R} distribution. Using a second order polynomial interpolation in the top-quark mass a continuous parameterization for each bin is derived. The binning choice follows Refs. [2] and [5]. In case of the choices with 5 or 6 bins, the setting is motivated by a detailed experimental analysis done by ATLAS and CMS to optimize the bins with respect to statistical and systematic uncertainties. In case of the choices with 10 or 20 bins, a uniform binning is used. Comparing the results obtained using different binnings, serves as check that the bin choice does not introduce a bias in the extracted mass value. The top-quark mass is extracted minimizing the quantity:

$$\chi^2 = \sum_{i \text{ bins}} \frac{\mathcal{R}_i^O - \mathcal{R}_i(m_t)}{\sqrt{\mathcal{R}_i^O}} \quad (4.9)$$

where \mathcal{R}_i^O is one of the approximations calculated in Ref. [72]. The corresponding uncertainty is given by $\sqrt{\mathcal{R}_i^O}$. We include an additional uncertainty $\sqrt{\mathcal{R}_i(m_t)}$ for the continuous parametrization. In all quantities the index i labels the respective bin. The

⁹A light jet is defined as a jet originated from a u -, d -, c -, s -quark or a gluon.

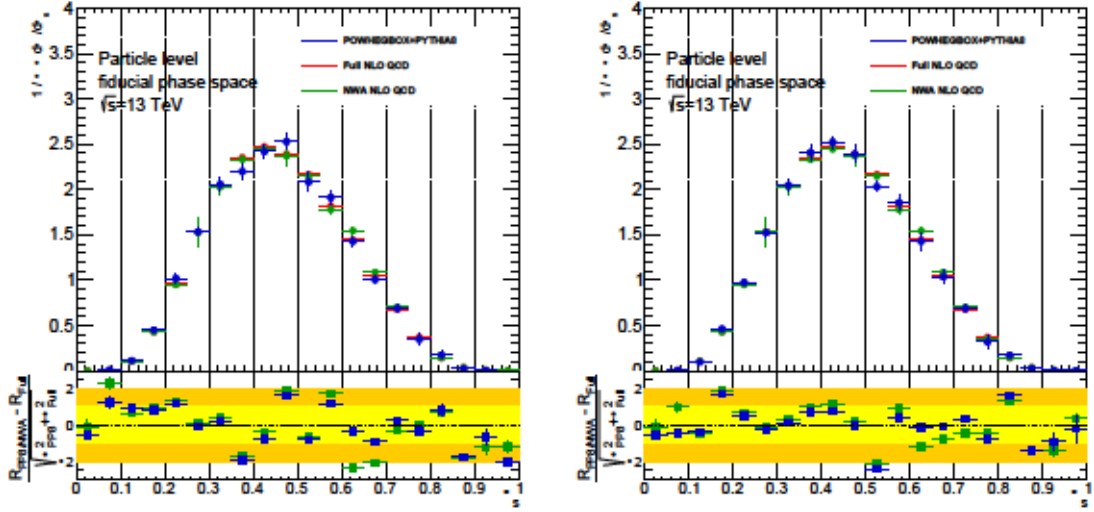


Figure 37. Comparison between the \mathcal{R} distributions computed using POWHEG-BOX + PYTHIA8 (blue), the calculation including off-shell and non-resonant contributions as well as finite width effects (*Full NLO*) [72] (red) and the calculation in the NWA [72] (green). Error bars refer to statistical uncertainties of the MC simulation. The lower plots show the differences between predictions of the POWHEG-BOX + PYTHIA8 or NWA and those of the full calculation, normalized to the statistical uncertainty. The yellow (orange) area represents the 1σ (2σ) band, where the standard deviation is calculated as the quadratic sum of the uncertainties of the two calculations, the statistical uncertainty of POWHEG-BOX + PYTHIA8 prediction due to a finite number of simulated events, and the uncertainty from the numerical MC integration of the *Full NLO* calculation. The uncertainties of the POWHEG-BOX + PYTHIA8 computation dominates the total uncertainty. The distribution on the left (right) is computed setting the parameter $hdamp$ of POWHEG-BOX to m_t (infinity).

results are shown in Fig. 38. As a consistency check we applied the fit procedure also to the distributions generated with POWHEG-BOX + PYTHIA8. The left-hand plot shows the reconstructed top-quark mass as a function of the true top-quark mass used in generating the event sample. The fit reproduces the true value without an additional offset. In the right hand plot the same procedure is applied treating the different approximations from Ref. [72] as pseudo-data. Different binnings using 6, 8, 10 or 20 bins have been used. For each bin choice the result of the fit including its uncertainty is shown as a band. As one can see using $\mathcal{R}^{\text{Full}}$ as pseudo-data, the true mass value is recovered within an uncertainty of about 500 MeV, which is below the sum of modeling uncertainties on m_t reported in Refs. [2, 5, 72]. Furthermore, this finding is, within the uncertainties, independent on the binning of \mathcal{R} . One can thus conclude that POWHEG-BOX + PYTHIA8 gives a reliable description of the \mathcal{R} distribution. As a consequence POWHEG-BOX + PYTHIA8 can be used to unfold the data to the parton-level. Using instead the NWA_{Prod} approximation from Ref. [72] we reproduce the sizable shift of about 3 GeV as observed already in Ref. [72].

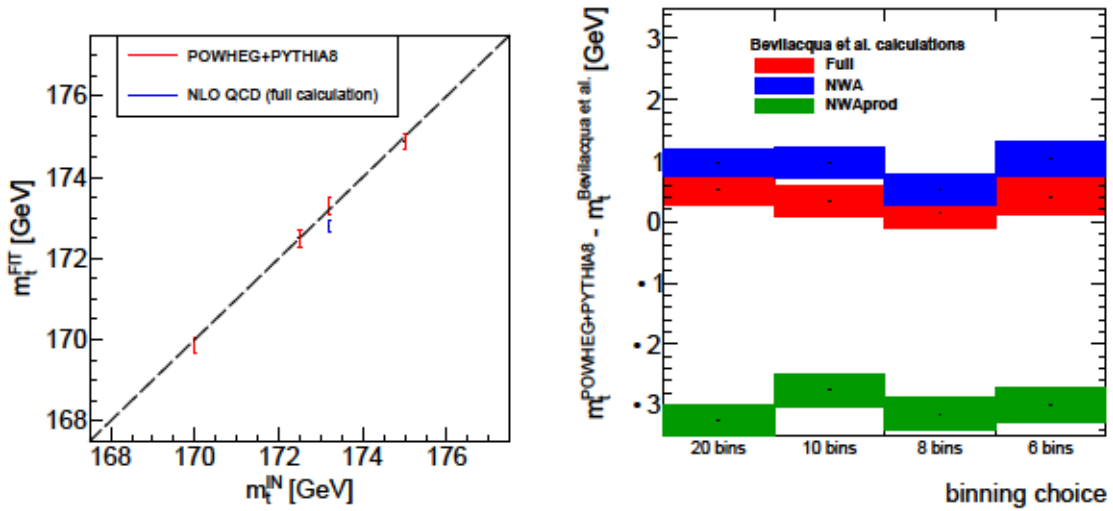


Figure 38. Linearity of the fit (left) and differences between top-quark mass values extracted from \mathcal{R} distributions calculated with different approaches (right). Different binning choices have been tested: 20 and 10 bins of equal size (respectively with widths 0.05 and 0.1), the 6 bins choice of Ref. [2, 3] and the 8 bins choice of Ref. [5]. Results are found to be consistent across the binning choices.

This is not surprising as the NWA_{Prod} approximation neglects NLO corrections in the decay stage. The bulk of the effect has thus nothing to do with off-shell effects but is a consequence of missing higher-order corrections, also considering that for the NWA approximation we do not observe the sizable shift reported in Ref. [72]. In fact inspecting Fig. 3 of Ref. [72] the size of the shift observed in Ref. [72] is surprising: in the range $0.3 < \rho_s < 0.6$ the two approximations *Full NLO* and *NWA* give consistent results. For larger ρ_s one can observe differences. However, the results fluctuate indicating that statistical uncertainties are important. For lower ρ_s there is a systematic difference. However, this corresponds to the high-energy region which should have only a marginal effect on the mass extraction. In fact in this region the different scale setting procedures applied in *Full NLO* and *NWA* lead to rather different values for the renormalization scale which could at least partially explain the differences in that region. As the NWA approximation as quoted in Ref. [72] is not used in the aforementioned experimental analysis we have not tried to pin down the shift observed in Fig. 38.

5 Conclusions

The main aim of this work is investigating the effects of different inputs on theoretical predictions for $t\bar{t}j$ hadroproduction at the LHC and providing reference cross sections with NLO QCD accuracy to the experimental collaborations, with particular emphasis on

the distributions used for top-quark mass extractions on the basis of experimental data concerning this process.

Among the different renormalization and factorization scale choices that we investigated, including both the static scale m_t and dynamical scales based on the $m_{t\bar{j}}$ and H_T quantities, we find that the $\mu_R = \mu_F = H_T/4$ dynamical scale provides the smallest NLO/LO \mathcal{K} -factor and minimizes shape variation effects when comparing predictions at these two orders for a wide selection of differential distributions, under the typical, quite inclusive, sets of analysis cuts currently adopted by the experimental collaborations. Therefore, we recommend the use of this scale, especially in case of absolute differential fiducial cross sections. On the other hand, in case of total fiducial cross sections, we find that even the static scale still represents a competitive option. This applies also to the normalized distribution $\mathcal{R}(m_t/s)$ used in present ATLAS and CMS analyses aiming at top-quark mass extraction, in the region $s = 0.3$. If future analyses will start to make use of the shape of the $\mathcal{R}(m_t/s)$ distribution for smaller values of s , it will become mandatory to use dynamical scales for a more reliable theoretical description. It will also be very important to use PDF fits with decreased uncertainties at large x , considering that, for both the s and the $\mathcal{R}(m_t/s)$ distributions, we have found that PDF uncertainties are particularly large in the small s region, that is mostly populated by hard-scattering interactions involving at least one large- x parton. While present experimental analyses do not particularly focus on the small s region, the sensitivity may increase with the increasing statistics of the data collected, as expected during the high luminosity (HL) phase of the LHC. Additionally, in the tails of the s distribution, fixed-order NLO calculations may not provide an accurate enough description. Further higher-order perturbative corrections beyond NLO for the hard-scattering process can be crucial to reduce uncertainties there.

Furthermore, we have investigated the dependence of QCD uncertainties on the jet radius parameter R used to construct jets according to the anti- k_T jet clustering algorithm. Comparing predictions for $R = 0.4$ and $R = 0.8$, we found that the size of the scale uncertainty bands is almost independent of the choice of the R value. A slight advantage of using $R = 0.8$ instead of the currently adopted $R = 0.4$ value would be offered by the larger absolute cross sections, allowing to better exploit low-statistics kinematical regions. It will be interesting to repeat such an investigation in presence of full shower Monte Carlo effects, which affect the jet formation process.

For the time being, we list some of our reference cross sections at $\sqrt{S} = 13$ and 14 TeV in Appendix A and make available an exhaustive set of predictions in the online repository [71], confident that they might be very useful for top-quark mass extractions on the basis of the data already collected at the LHC during Run 2 and the new data expected from the forthcoming Run 3.

These predictions, beside referring to different modern PDF sets, different scales and different analysis cuts on the jets, cover a wide range of top-quark mass values, renormalized in different schemes. In particular, in this work we show for the first time predictions for the $t\bar{t}j$ hadroproduction process using the MSR top-quark mass renormalization

scheme, providing an alternative to the on-shell and the $\overline{\text{MS}}$ schemes already used for top-quark mass extraction in previous $t\bar{t}j$ phenomenological studies and experimental analyses. We found that in the $0.2 < s < 0.7$ region the size of scale uncertainty bands using these three different top-quark mass renormalization schemes is approximately the same. On the other hand, close to threshold, the $\overline{\text{MS}}$ mass does not provide a good description, as expected on the basis of theory considerations and as proven in practice by the fact that scale uncertainties become very large. The mass dependence of the cross sections turns out to be linear, which allows to good approximation a linear interpolation between theory predictions for different m_t values, when building the χ^2 for performing the top-quark mass fits.

We finally observe that the \mathcal{R} distribution in the s region of largest experimental interest can be decently modeled by using simulations with POWHEG-BOX + PYTHIA8, making use of the POWHEG NLO matching algorithm and of PYTHIA8 to decay and shower $t\bar{t}j$ Les-Houches events with stable top-quarks and at most one extra parton. As far as the \mathcal{R} distribution is concerned, the predictions from this setup turn out to agree within the uncertainties with the calculation of Ref. [14], including full off-shellness and spin correlation effects, but missing parton shower and soft physics effects. Of course, using the full calculation can be very relevant for an accurate description of other observables, like e.g. angular correlation observables or t and W invariant mass distributions, which are, however, outside the present scope of $t\bar{t}j$ experimental analyses aiming at top-quark mass extraction. Once a calculation like the most sophisticated one in Ref. [14] will be combined with Shower Monte Carlo codes, it may also allow to further reduce modeling uncertainties in the top-quark mass measurements.

In conclusion, considering, on the one hand, the advanced techniques applied in the experimental analysis to reconstruct top quarks from their decay products and, on the other hand, the present level of experimental uncertainties, we are confident that the predictions presented in this work and in the associated repository are robust enough for reliable extractions of the top-quark mass parameter using LHC Run 2 and future Run 3 data, while hoping for future theoretical and experimental developments which might further increase the accuracy of these extractions and decrease the associated systematic uncertainties, during the HL-LHC phase.

Acknowledgments

We would like to thank Malgorzata Worek for providing us with numerical input for the study of off-shell effects. We are grateful to Giuseppe Bevilacqua for further clarifications and to André Hoang, Katerina Lipka, Marcel Vos, and Sebastian Wuchterl for useful discussions.

The work of S.A. and A.G. is supported by the ERC Starting Grant REINVENT-714788. S.A. also acknowledges funding from Fondazione Cariplo and Regione Lombardia, grant 2017-2070 and from MIUR through the FARE grant R18ZRBEAFC. J.F.

and A.I. acknowledge support from projects PGC2018-094856-B-100 (MICINN/FEDER), PROMETEO-2018/060 and CIDEAGENT/2020/21 (Generalitat Valenciana), and the iLINK grant LINKB20065 (CSIC). The work of M.V.G., S.M. and P.U. was supported in part by the Bundesministerium für Bildung und Forschung under contracts 05H21GUCCA and 05H18KHCA1.

A Numerical results for cross sections for different scales, top-quark masses and analysis cuts

In the following we present predictions for cross sections for $t\bar{t}j$ production in pp collisions at $\sqrt{S} = 13$ TeV at the LHC for future reference. In Tables 3, 4, 5 and 6, using as input $m_t^{\text{pole}} = 172$ GeV and the CT18 NLO PDF central set, we provide predictions for the s distribution under the default system of cuts described at the beginning of Section 3, that is $N_j = 1$, $p_T^j = 30$ GeV, $j = 2, 4$, for the different central scale choices: $\mu_R = \mu_F = \mu_0 = m_t$, $H_T^B = 2$, $H_T^B = 4$ and $m_{t\bar{t}j}^B$, as defined in Section 2. Scale variation effects, computed by varying simultaneously μ_R and μ_F by a factor of two around the central value are also shown.

x_l	x_r	K_R	K_F	0.5	K_R	K_F	1	K_R	K_F	2
0.0	0.18	12.6	0.2		22.0	0.1		21.70	0.07	
0.18	0.22	136	1		166.7	0.6		154.7	0.4	
0.22	0.27	269	1		300.1	0.9		271.5	0.9	
0.27	0.32	437	1		457.3	0.9		409.8	0.6	
0.32	0.38	609	2		616	1		546.6	0.8	
0.38	0.45	765	2		752	1		663.6	0.6	
0.45	0.53	845	1		814	1		717	2	
0.53	0.62	800	1		759.8	0.9		667.8	0.6	
0.62	0.71	615	1		576.2	0.9		505.6	0.6	
0.71	1.0	133.1	0.3		123.8	0.2		108.5	0.1	

Table 3. NLO predictions for the s distribution [pb] for $t\bar{t}j$ X hadroproduction at $\sqrt{S} = 13$ TeV using as input the CT18 NLO central PDF set, $m_t = 172$ GeV and $\mu_0 = m_t$, for $N_j = 1$, $p_T^j = 30$ GeV, $j = 2, 4$. See Section 3 for more detail.

Covering a range of top-quark mass values, a series of slightly different cuts $p_T^j = 30, 50, 75$ and 100 GeV along with $j = 2, 4$, and using as input the ABMP16_5_nlo PDF set, Tables 7–14 provide further examples for reference cross sections, the complete set of which is collected in the online repository [71].

x_l	x_r	K_R	K_F	0.5	K_R	K_F	1	K_R	K_F	2
0.0	0.18	23.91	0.09		21.10	0.06		17.38	0.05	
0.18	0.22	171.9	0.8		152.4	0.5		126.7	0.3	
0.22	0.27	306	1		269.9	0.8		226.6	0.4	
0.27	0.32	464	1		413.9	0.7		348.6	0.5	
0.32	0.38	626	2		558.7	0.9		473.5	0.6	
0.38	0.45	760	1		684.9	0.8		584.5	0.6	
0.45	0.53	828	2		749.5	0.8		643.4	0.9	
0.53	0.62	7745	1		706.1	0.7		609.6	0.6	
0.62	0.71	592	1		541.1	0.6		470.1	0.5	
0.71	1.0	127.9	0.3		117.6	0.2		102.5	0.2	

Table 4. Same as Table 3, but for $\mu_0 = H_T^B = 2$.

x_l	x_r	K_R	K_F	0.5	K_R	K_F	1	K_R	K_F	2
0.0	0.18	22.23	0.1		23.9	0.1		21.1	0.1	
0.18	0.22	164	1		171.9	0.8		152.4	0.5	
0.22	0.27	294	1		306	1		269.9	0.8	
0.27	0.32	446	2		464	1		413.9	0.7	
0.32	0.38	601	2		626	2		558.7	0.9	
0.38	0.45	732	2		760	1		684.9	0.8	
0.45	0.53	797	2		828	2		749.5	0.8	
0.53	0.62	743	2		775	1		706.1	0.7	
0.62	0.71	567	2		592	1		541.1	0.6	
0.71	1.0	123.4	0.8		127.9	0.3		117.6	0.2	

Table 5. Same as Table 3, but for $\mu_0 = H_T^B = 4$.

x_l	x_r	K_R	K_F	0.5	K_R	K_F	1	K_R	K_F	2
0.0	0.18	19.59	0.06		16.26	0.04		13.17	0.03	
0.18	0.22	146.2	0.4		123.1	0.3		100.8	0.3	
0.22	0.27	265.2	0.6		226.0	0.5		186.5	0.4	
0.27	0.32	412.5	0.7		355.0	0.5		296.2	0.5	
0.32	0.38	565.3	0.8		492.5	0.6		413.9	0.5	
0.38	0.45	698	1		618.1	0.6		523.4	0.5	
0.45	0.53	768	1		689.2	0.6		590.5	0.7	
0.53	0.62	725.9	0.9		659.1	0.6		570.4	0.5	
0.62	0.71	554.0	0.9		510.3	0.8		446.1	0.4	
0.71	1.0	119.9	0.4		111.9	0.2		98.6	0.1	

Table 6. Same as Table 3, but for $\mu_0 = m_{ij}^B = 2$.

		$\frac{d}{d^s} \frac{ij, X}{d^s}$ distribution with N_j															
x_l	x_r	165 GeV	166 GeV	167 GeV	168 GeV	169 GeV	170 GeV	171 GeV	172 GeV	173 GeV	174 GeV	175 GeV	176 GeV	177 GeV	178 GeV	179 GeV	
		$\frac{d}{d^s} \frac{ij, X}{d^s}$ distribution with N_j															
x_l	x_r	165 GeV	166 GeV	167 GeV	168 GeV	169 GeV	170 GeV	171 GeV	172 GeV	173 GeV	174 GeV	175 GeV	176 GeV	177 GeV	178 GeV	179 GeV	
0.00	0.18	19.49(6)	19.32(6)	19.23(6)	18.91(6)	18.79(6)	18.70(6)	18.48(6)	18.16(5)	18.13(5)	17.97(5)	17.72(5)	17.64(5)	17.49(5)			
0.18	0.22	159.1(6)	158.6(5)	156.4(5)	153.7(5)	152.7(5)	151.2(5)	149.6(5)	146.6(5)	146.0(5)	143.9(5)	142.1(4)	142.3(4)	139.6(4)			
0.22	0.27	299.0(8)	295.4(7)	291.3(7)	287.4(7)	285.6(7)	281.2(7)	278.4(7)	274.0(7)	271.8(6)	269.0(6)	264.4(6)	262.4(6)	259.4(6)			
0.27	0.32	475.0(1)	469.0(1)	461.0(1)	457.0(1)	452.0(1)	443.2(1)	439.6(1)	432.2(9)	426.1(9)	421.2(9)	414.9(9)	409.4(9)	401.9(9)			
0.32	0.38	658.0(1)	650.0(1)	639.0(1)	632.0(1)	619.0(1)	612.0(1)	604.0(1)	596.0(1)	585.0(1)	576.0(1)	568.8(1)	559.7(1)	553.0(1)			
0.38	0.45	830.0(1)	813.0(1)	803.0(1)	788.0(1)	776.0(1)	762.0(1)	749.0(1)	739.0(1)	728.0(1)	716.0(1)	703.0(1)	692.0(1)	679.0(1)			
0.45	0.53	931.0(1)	914.0(1)	894.0(1)	878.0(1)	861.0(1)	843.0(1)	829.0(1)	811.0(1)	796.0(1)	781.0(1)	768.0(1)	750.0(1)	736.0(1)			
0.53	0.62	899.0(1)	883.0(1)	858.0(1)	840.0(1)	823.0(1)	806.0(1)	783.0(1)	763.0(1)	746.0(1)	731.0(1)	711.0(1)	695.0(1)	678.0(1)			
0.62	0.71	732.0(1)	709.0(1)	690.0(1)	667.0(1)	644.0(1)	625.0(1)	605.0(1)	586.0(1)	566.1(1)	546.6(1)	529.1(9)	511.9(9)	493.7(9)			
0.71	1.00	200.0(3)	188.2(3)	176.5(3)	165.3(3)	155.2(3)	144.9(3)	135.4(3)	126.6(2)	118.3(2)	109.8(2)	103.0(2)	95.4(2)	88.8(2)			
		$\frac{d}{d^s} \frac{ij, X}{d^s}$ distribution with N_j															
x_l	x_r	165 GeV	166 GeV	167 GeV	168 GeV	169 GeV	170 GeV	171 GeV	172 GeV	173 GeV	174 GeV	175 GeV	176 GeV	177 GeV	178 GeV	179 GeV	
0.00	0.18	19.30(4)	19.24(4)	18.88(4)	18.67(4)	18.52(4)	18.36(4)	18.19(3)	18.01(3)	17.80(3)	17.58(3)	17.41(3)	17.32(3)	17.13(3)			
0.18	0.22	149.4(3)	146.4(3)	145.4(3)	143.8(3)	142.0(3)	140.0(3)	138.3(3)	136.6(3)	135.2(3)	133.7(3)	131.6(3)	130.5(3)	128.6(3)			
0.22	0.27	271.3(5)	267.4(5)	264.4(5)	260.4(5)	258.0(4)	254.3(4)	251.1(4)	248.5(4)	245.8(4)	242.4(4)	240.0(4)	235.7(4)	232.8(4)			
0.27	0.32	424.4(7)	418.4(7)	411.7(7)	407.7(7)	401.0(6)	395.1(7)	389.8(6)	383.6(6)	380.1(6)	374.7(6)	369.3(6)	364.2(6)	359.7(6)			
0.32	0.38	584.2(8)	575.0(8)	564.6(8)	556.4(8)	548.0(7)	540.0(7)	532.2(7)	524.3(7)	517.6(7)	510.0(7)	501.3(7)	494.4(6)	487.6(6)			
0.38	0.45	729.0(8)	717.1(8)	703.8(8)	693.8(8)	680.9(8)	669.6(8)	659.3(8)	649.2(8)	637.6(7)	627.1(7)	615.7(7)	606.6(7)	596.3(7)			
0.45	0.53	812.8(9)	796.3(9)	782.0(9)	767.1(9)	752.1(8)	740.2(8)	723.9(8)	710.6(8)	696.5(8)	683.7(8)	670.1(7)	657.6(7)	645.1(7)			
0.53	0.62	789.9(9)	770.3(9)	752.3(9)	735.4(9)	717.9(8)	700.5(8)	683.0(8)	669.9(8)	652.9(7)	637.1(7)	622.8(7)	606.5(7)	592.1(7)			
0.62	0.71	636.7(8)	618.8(8)	598.9(8)	581.7(8)	561.3(7)	546.1(7)	527.9(7)	508.9(7)	492.6(7)	477.1(6)	460.4(6)	445.8(6)	430.7(6)			
0.71	1.00	174.0(2)	163.0(2)	153.6(2)	143.8(2)	134.8(2)	125.7(2)	117.8(2)	110.2(2)	103.1(2)	95.9(2)	89.8(1)	83.0(1)	77.1(1)			
		$\frac{d}{d^s} \frac{ij, X}{d^s}$ distribution with N_j															
x_l	x_r	165 GeV	166 GeV	167 GeV	168 GeV	169 GeV	170 GeV	171 GeV	172 GeV	173 GeV	174 GeV	175 GeV	176 GeV	177 GeV	178 GeV	179 GeV	
0.00	0.18	10.5(1)	10.9(1)	10.7(1)	10.5(1)	10.4(1)	10.7(1)	10.7(1)	10.6(1)	10.58(9)	10.59(9)	10.59(9)	10.53(9)	10.38(9)			
0.18	0.22	125.9(9)	124.6(9)	124.1(9)	122.9(8)	123.3(9)	120.7(9)	121.3(8)	117.1(9)	118.1(8)	115.9(8)	116.0(7)	115.3(8)	114.8(8)			
0.22	0.27	265.0(1)	260.0(1)	259.0(1)	258.0(1)	255.0(1)	252.0(1)	246.0(1)	246.0(1)	242.0(1)	240.0(1)	237.0(1)	236.0(1)	232.6(1)			
0.27	0.32	446.0(2)	443.0(2)	439.0(2)	434.0(2)	423.0(2)	422.0(2)	418.0(2)	410.0(2)	405.0(2)	402.0(2)	397.0(2)	388.0(1)	387.0(1)			
0.32	0.38	646.0(2)	643.0(2)	636.0(2)	623.0(2)	615.0(2)	610.0(2)	596.0(2)	588.0(2)	584.0(2)	569.0(2)	565.0(2)	554.0(2)	548.0(2)			
0.38	0.45	846.0(2)	829.0(2)	815.0(2)	805.0(2)	789.0(2)	779.0(2)	764.0(2)	755.0(2)	738.0(2)	727.0(2)	715.0(2)	707.0(2)	691.0(2)			
0.45	0.53	966.0(2)	946.0(2)	933.0(2)	913.0(2)	896.0(2)	875.0(2)	862.0(2)	843.0(2)	828.0(2)	811.0(2)	799.0(2)	782.0(2)	766.0(2)			
0.53	0.62	955.0(2)	933.0(2)	910.0(2)	889.0(2)	866.0(2)	844.0(2)	826.0(2)	809.0(2)	789.0(2)	770.0(2)	751.0(2)	735.0(2)	719.0(2)			
0.62	0.71	780.0(2)	757.0(2)	733.0(2)	710.0(2)	688.0(2)	664.0(2)	643.0(2)	626.0(2)	604.0(2)	586.0(2)	564.0(2)	544.0(1)	528.0(1)			
0.71	1.00	215.2(6)	203.0(5)	192.2(5)	178.3(5)	167.9(5)	157.8(5)	146.3(4)	137.0(4)	128.3(4)	119.2(4)	111.4(4)	103.0(3)	96.3(3)			

Table 7. NLO predictions for the s distribution in the pole mass scheme for $\sqrt{s} = 13$ TeV using as input the static scale $\mu_0 = m_t$ and the ABMP16 NLO PDF set. At least one jet with $p_T^j \geq 2.4$ and $p_T^j \geq 30$ GeV is required.

		$\frac{d^{ij,x}}{d^s}$ distribution with N_j															
x_l	x_r	165 GeV	166 GeV	167 GeV	168 GeV	169 GeV	170 GeV	171 GeV	172 GeV	173 GeV	174 GeV	175 GeV	176 GeV	177 GeV	178 GeV	179 GeV	
		$\frac{d^{ij,x}}{d^s}$ distribution with N_j															
		$\frac{d^{ij,x}}{d^s}$ distribution with N_j															
0.00	0.18	19.23(6)	19.09(6)	18.94(5)	18.63(6)	18.52(6)	18.42(5)	18.19(5)	17.89(5)	17.86(5)	17.67(5)	17.46(5)	17.38(5)	17.22(5)	17.11(5)	17.00(5)	16.89(5)
0.18	0.22	152.3(5)	152.1(5)	149.7(4)	147.3(5)	146.3(5)	145.0(4)	143.4(4)	139.9(4)	139.6(4)	137.5(4)	136.7(4)	135.9(4)	133.6(4)	132.8(4)	132.0(4)	131.1(4)
0.22	0.27	276.7(7)	273.0(6)	268.6(6)	265.6(6)	263.1(6)	259.1(6)	255.7(6)	253.3(6)	249.9(5)	247.4(5)	244.0(5)	240.7(5)	237.7(5)	236.9(5)	236.0(5)	235.1(5)
0.27	0.32	420.1(9)	412.0(9)	405.6(8)	401.0(9)	396.9(8)	388.2(8)	386.0(8)	378.3(8)	373.8(7)	368.8(7)	362.2(7)	357.7(7)	350.9(7)	349.1(7)	348.2(7)	347.3(7)
0.32	0.38	547.6(1)	541.6(1)	532.0(9)	525.8(9)	514.7(9)	508.5(9)	499.1(8)	494.1(8)	483.8(8)	474.8(8)	469.0(8)	462.2(8)	456.1(7)	454.3(7)	453.4(7)	452.5(7)
0.38	0.45	647.5(1)	634.7(1)	623.2(9)	612.8(9)	601.0(9)	591.3(9)	579.8(8)	570.5(8)	560.7(8)	551.9(8)	541.3(7)	531.9(8)	522.6(8)	520.8(8)	519.9(8)	519.0(8)
0.45	0.53	666.3(9)	653.1(9)	638.4(9)	624.0(9)	612.5(9)	597.9(8)	586.8(8)	571.3(8)	561.9(8)	550.7(8)	538.9(7)	527.1(7)	516.6(7)	514.8(7)	513.9(7)	513.0(7)
0.53	0.62	573.9(9)	561.5(9)	546.1(8)	531.4(8)	519.5(7)	504.3(8)	491.6(7)	477.7(7)	465.2(7)	454.9(7)	440.1(6)	428.3(7)	415.8(6)	414.0(6)	413.1(6)	412.2(6)
0.62	0.71	393.1(7)	379.4(7)	366.0(7)	353.0(7)	337.4(6)	325.8(6)	312.2(6)	301.3(6)	290.5(6)	276.9(6)	265.5(5)	255.4(5)	244.4(5)	242.6(5)	241.7(5)	240.8(5)
0.71	1.00	66.2(2)	61.5(2)	56.8(1)	52.4(1)	48.7(1)	44.7(1)	41.3(1)	37.7(1)	34.7(1)	31.7(1)	29.28(9)	26.71(9)	24.27(8)	24.09(8)	23.90(8)	23.71(8)
		$\frac{d^{ij,x}}{d^s}$ distribution with N_j															
x_l	x_r	165 GeV	166 GeV	167 GeV	168 GeV	169 GeV	170 GeV	171 GeV	172 GeV	173 GeV	174 GeV	175 GeV	176 GeV	177 GeV	178 GeV	179 GeV	
0.00	0.18	18.83(4)	18.77(4)	18.41(4)	18.22(4)	18.09(3)	17.93(3)	17.74(3)	17.53(3)	17.36(3)	17.16(3)	16.96(3)	16.89(3)	16.66(3)	16.58(3)	16.47(3)	
0.18	0.22	142.0(3)	139.0(3)	138.0(3)	136.7(3)	134.6(3)	133.1(3)	131.0(3)	129.3(3)	128.2(3)	126.8(3)	124.7(3)	123.6(3)	122.0(3)	121.2(3)	120.3(3)	
0.22	0.27	248.4(4)	245.0(4)	242.1(4)	238.3(4)	235.9(4)	233.1(4)	229.9(4)	227.0(4)	223.9(3)	221.0(4)	218.0(4)	215.1(4)	212.2(3)	211.4(3)	210.5(3)	
0.27	0.32	370.6(6)	365.5(6)	359.0(6)	355.4(6)	348.9(5)	343.8(5)	339.0(5)	333.9(5)	329.8(5)	325.0(5)	320.4(5)	316.2(5)	312.0(4)	311.2(4)	310.3(4)	
0.32	0.38	482.6(6)	473.6(6)	466.6(6)	459.3(6)	451.7(5)	444.4(5)	438.5(5)	431.2(5)	424.8(5)	418.3(5)	411.8(5)	405.3(5)	397.9(5)	396.1(5)	395.2(5)	
0.38	0.45	562.1(6)	553.4(6)	544.0(6)	534.0(6)	523.5(6)	514.5(5)	505.7(6)	497.0(5)	487.3(5)	479.2(5)	469.5(5)	461.7(5)	453.5(5)	451.7(5)	450.8(5)	
0.45	0.53	577.4(6)	565.8(6)	552.3(6)	541.8(6)	530.8(5)	519.7(5)	508.1(5)	497.9(5)	487.6(5)	476.7(5)	467.5(5)	457.0(5)	447.2(5)	445.4(5)	444.5(5)	
0.53	0.62	499.3(6)	485.6(5)	473.4(5)	461.5(5)	449.0(5)	436.3(5)	423.8(5)	414.4(5)	401.7(5)	391.3(4)	380.0(4)	370.7(4)	360.3(4)	358.5(4)	357.6(4)	
0.62	0.71	340.3(5)	327.7(5)	316.0(5)	303.2(4)	291.5(4)	281.0(4)	269.9(4)	259.1(4)	249.1(4)	239.5(4)	229.2(3)	219.8(3)	211.8(3)	210.0(3)	209.1(3)	
0.71	1.00	57.0(1)	52.7(1)	48.8(1)	45.12(9)	41.78(8)	38.57(8)	35.36(8)	32.54(7)	29.92(7)	27.41(7)	25.07(6)	22.92(6)	20.79(6)	20.61(6)	20.52(6)	
		$\frac{d^{ij,x}}{d^s}$ distribution with N_j															
x_l	x_r	165 GeV	166 GeV	167 GeV	168 GeV	169 GeV	170 GeV	171 GeV	172 GeV	173 GeV	174 GeV	175 GeV	176 GeV	177 GeV	178 GeV	179 GeV	
0.00	0.18	11.1(1)	11.3(1)	11.2(1)	10.99(9)	10.98(9)	11.24(9)	11.03(9)	10.96(9)	11.02(9)	10.99(8)	11.04(8)	10.89(8)	10.85(8)	10.77(8)	10.68(8)	
0.18	0.22	124.1(9)	123.6(8)	122.9(8)	121.5(8)	121.1(8)	119.9(8)	119.7(7)	115.6(8)	116.9(7)	114.7(7)	114.4(7)	113.8(7)	113.2(7)	112.4(7)	111.5(7)	
0.22	0.27	252.0(1)	247.0(1)	244.0(1)	244.3(1)	240.0(1)	238.0(1)	232.7(1)	233.0(1)	229.1(1)	227.0(9)	223.6(9)	222.8(9)	220.3(8)	219.5(8)	218.6(8)	
0.27	0.32	403.0(1)	396.0(2)	395.0(1)	390.0(1)	381.0(1)	377.0(1)	376.0(1)	367.0(1)	363.0(1)	360.0(1)	355.0(1)	347.0(1)	347.0(1)	346.1(1)	345.2(1)	
0.32	0.38	553.0(2)	546.0(2)	538.0(2)	526.0(1)	522.0(2)	515.0(1)	501.0(1)	499.0(1)	493.0(1)	481.0(1)	477.0(1)	470.0(1)	460.0(1)	458.2(1)	457.3(1)	
0.38	0.45	670.0(2)	656.0(2)	644.0(2)	636.0(1)	623.0(2)	616.0(1)	604.0(1)	593.0(1)	581.0(1)	575.0(1)	561.0(1)	554.0(1)	542.0(1)	540.2(1)	539.3(1)	
0.45	0.53	705.0(2)	691.0(2)	677.0(2)	662.0(1)	645.0(1)	634.0(1)	621.0(1)	607.0(1)	596.0(1)	584.0(1)	574.0(1)	560.0(1)	549.0(1)	547.2(1)	546.3(1)	
0.53	0.62	623.0(1)	607.0(1)	588.0(1)	572.0(1)	560.0(1)	542.0(1)	528.0(1)	515.0(1)	498.0(1)	489.0(1)	476.0(1)	463.0(1)	452.0(1)	450.2(1)	449.3(1)	
0.62	0.71	430.0(1)	413.0(1)	400.0(1)	385.0(1)	367.0(1)	356.0(1)	341.9(1)	329.3(1)	315.1(1)	305.9(9)	289.2(9)	279.8(8)	268.2(8)	266.4(8)	265.5(8)	
0.71	1.00	73.1(3)	67.7(2)	63.0(2)	58.1(2)	54.0(2)	49.7(2)	45.8(2)	42.2(2)	38.9(2)	35.5(2)	32.7(1)	29.7(1)	27.1(1)	26.9(1)	26.8(1)	

Table 8. Same as 7 but for p_T^j 50 GeV.

		$\frac{d^{ij,x}}{d^s}$ distribution with N_j															
x_l	x_r	165 GeV	166 GeV	167 GeV	168 GeV	169 GeV	170 GeV	171 GeV	172 GeV	173 GeV	174 GeV	175 GeV	176 GeV	177 GeV	178 GeV	179 GeV	
		$\frac{d^{ij,x}}{d^s}$ distribution with N_j															
		$\frac{d^{ij,x}}{d^s}$ distribution with N_j															
0.00	0.18	18.69(6)	18.48(6)	18.39(5)	18.13(5)	17.98(5)	17.87(5)	17.65(5)	17.38(4)	17.37(5)	17.16(5)	16.98(4)	16.87(4)	16.74(5)	16.74(5)	16.74(5)	
0.18	0.22	142.0(5)	141.3(4)	139.4(4)	137.4(4)	135.5(4)	134.7(4)	133.1(4)	130.4(4)	129.7(4)	127.5(4)	126.8(4)	125.7(4)	123.7(4)	123.7(4)	123.7(4)	
0.22	0.27	245.7(5)	242.3(5)	239.0(5)	234.9(5)	232.5(5)	229.4(5)	226.3(5)	223.9(5)	220.7(5)	218.4(4)	215.0(4)	212.5(4)	209.7(5)	209.7(5)	209.7(5)	
0.27	0.32	351.3(7)	345.6(7)	341.1(6)	336.5(7)	332.9(7)	325.9(6)	323.1(6)	317.5(6)	312.9(6)	308.2(6)	304.3(6)	299.2(6)	294.2(6)	294.2(6)	294.2(6)	
0.32	0.38	435.7(8)	429.4(7)	422.4(7)	417.0(7)	407.6(7)	402.3(6)	396.1(6)	390.1(6)	382.2(6)	376.9(6)	369.6(6)	364.4(6)	359.4(6)	359.4(6)	359.4(6)	
0.38	0.45	478.6(7)	469.1(7)	459.0(7)	452.0(7)	443.3(7)	434.6(6)	427.2(6)	419.6(6)	411.7(6)	403.4(6)	396.2(6)	388.7(6)	382.2(6)	382.2(6)	382.2(6)	
0.45	0.53	449.1(7)	438.3(7)	428.6(6)	419.4(7)	410.1(6)	399.4(6)	392.0(6)	381.6(5)	373.3(5)	364.6(5)	356.7(5)	347.7(5)	339.7(5)	339.7(5)	339.7(5)	
0.53	0.62	337.1(6)	328.1(6)	316.9(5)	307.5(5)	299.4(5)	289.6(5)	280.9(5)	271.6(4)	262.7(4)	255.1(4)	246.8(4)	239.6(4)	231.1(4)	231.1(4)	231.1(4)	
0.62	0.71	179.7(4)	171.5(4)	163.0(4)	155.5(4)	147.8(4)	140.6(3)	133.5(3)	127.0(3)	121.0(3)	114.1(3)	107.6(3)	102.3(3)	96.6(3)	96.6(3)	96.6(3)	
0.71	1.00	14.44(6)	12.98(6)	11.64(5)	10.37(5)	9.28(5)	8.29(4)	7.39(4)	6.58(4)	5.83(4)	5.10(3)	4.46(3)	3.87(3)	3.34(3)	3.34(3)	3.34(3)	
		$\frac{d^{ij,x}}{d^s}$ distribution with N_j															
x_l	x_r	165 GeV	166 GeV	167 GeV	168 GeV	169 GeV	170 GeV	171 GeV	172 GeV	173 GeV	174 GeV	175 GeV	176 GeV	177 GeV	178 GeV	179 GeV	
0.00	0.18	18.22(4)	18.14(3)	17.79(3)	17.64(3)	17.49(3)	17.27(3)	17.12(3)	16.94(3)	16.75(3)	16.58(3)	16.39(3)	16.29(3)	16.09(3)	16.09(3)	16.09(3)	
0.18	0.22	131.7(3)	128.8(3)	128.0(3)	126.8(3)	125.0(3)	123.1(2)	121.3(2)	119.5(2)	118.7(2)	117.7(2)	115.2(2)	114.2(2)	113.1(2)	113.1(2)	113.1(2)	
0.22	0.27	219.7(3)	217.0(3)	213.9(3)	210.7(3)	208.2(3)	205.6(3)	203.0(3)	200.1(3)	197.1(3)	195.2(3)	192.5(3)	189.6(3)	187.3(3)	187.3(3)	187.3(3)	
0.27	0.32	311.7(5)	306.2(5)	301.8(4)	298.3(5)	293.0(4)	288.7(4)	284.2(4)	279.6(4)	275.9(4)	271.6(4)	267.4(4)	264.0(4)	260.4(4)	260.4(4)	260.4(4)	
0.32	0.38	382.7(5)	376.5(5)	370.1(5)	363.6(5)	357.6(4)	351.7(4)	346.0(4)	340.4(4)	335.3(4)	329.6(4)	324.3(4)	318.6(4)	312.9(4)	312.9(4)	312.9(4)	
0.38	0.45	415.6(5)	409.0(4)	400.0(4)	393.3(4)	385.2(4)	378.0(4)	371.9(4)	364.9(4)	356.7(4)	350.8(4)	343.6(4)	337.4(4)	331.4(4)	331.4(4)	331.4(4)	
0.45	0.53	388.5(4)	379.9(4)	370.2(4)	362.0(4)	354.2(4)	346.3(4)	338.1(4)	330.1(4)	323.1(4)	315.1(4)	308.0(3)	300.5(3)	294.3(3)	294.3(3)	294.3(3)	
0.53	0.62	291.5(4)	282.7(4)	274.1(4)	265.9(4)	257.9(3)	250.3(3)	241.4(3)	234.4(3)	226.7(3)	220.1(3)	212.4(3)	206.3(3)	199.2(3)	199.2(3)	199.2(3)	
0.62	0.71	154.4(3)	147.2(3)	139.9(3)	133.6(3)	126.7(2)	120.8(2)	114.8(2)	109.0(2)	103.2(2)	97.9(2)	92.8(2)	87.7(2)	82.8(2)	82.8(2)	82.8(2)	
0.71	1.00	12.27(4)	11.01(4)	9.89(4)	8.88(4)	7.94(3)	6.97(3)	6.25(3)	5.51(3)	4.90(2)	4.32(2)	3.77(2)	3.28(2)	2.78(2)	2.78(2)	2.78(2)	
		$\frac{d^{ij,x}}{d^s}$ distribution with N_j															
x_l	x_r	165 GeV	166 GeV	167 GeV	168 GeV	169 GeV	170 GeV	171 GeV	172 GeV	173 GeV	174 GeV	175 GeV	176 GeV	177 GeV	178 GeV	179 GeV	
0.00	0.18	11.1(1)	11.31(9)	11.12(9)	10.94(8)	10.97(9)	11.13(9)	10.99(8)	10.91(9)	10.93(8)	10.94(8)	10.98(7)	10.77(8)	10.75(8)	10.75(8)	10.75(8)	
0.18	0.22	116.7(8)	115.9(7)	115.3(7)	113.7(7)	114.8(7)	111.8(7)	112.5(7)	109.1(7)	109.3(6)	108.1(6)	107.1(6)	106.3(6)	106.1(6)	106.1(6)	106.1(6)	
0.22	0.27	222.4(1)	220.2(9)	217.2(9)	216.7(9)	215.3(9)	211.1(9)	208.0(8)	206.6(8)	204.6(8)	203.0(8)	199.0(8)	198.1(7)	195.2(7)	195.2(7)	195.2(7)	
0.27	0.32	341.0(1)	334.0(1)	332.0(1)	327.0(1)	321.0(1)	317.0(1)	315.0(1)	310.0(1)	306.0(1)	304.4(1)	299.7(1)	292.1(9)	291.3(9)	291.3(9)	291.3(9)	
0.32	0.38	440.0(1)	434.0(1)	428.0(1)	419.0(1)	413.0(1)	409.0(1)	400.0(1)	394.0(1)	392.0(1)	381.0(1)	378.0(1)	371.3(9)	365.2(9)	365.2(9)	365.2(9)	
0.38	0.45	495.0(1)	487.0(1)	479.0(1)	471.0(1)	463.0(1)	456.0(1)	446.0(1)	438.0(1)	428.0(1)	423.1(1)	413.5(1)	407.1(9)	399.1(9)	399.1(9)	399.1(9)	
0.45	0.53	478.0(1)	469.0(1)	455.0(1)	449.0(1)	435.0(1)	424.0(1)	417.0(1)	405.8(1)	397.6(9)	389.4(9)	383.5(9)	371.9(8)	363.9(8)	363.9(8)	363.9(8)	
0.53	0.62	366.6(1)	356.7(9)	344.0(9)	332.4(8)	325.1(9)	314.0(8)	304.3(8)	296.0(8)	287.1(8)	278.6(7)	269.7(7)	261.3(7)	252.5(7)	252.5(7)	252.5(7)	
0.62	0.71	197.2(7)	187.9(7)	181.0(7)	172.5(6)	164.2(6)	156.2(6)	147.5(6)	140.0(5)	132.1(5)	126.1(5)	119.6(5)	112.6(4)	107.2(4)	107.2(4)	107.2(4)	
0.71	1.00	16.2(1)	14.7(1)	12.91(9)	11.87(8)	10.67(8)	9.47(7)	8.59(7)	7.60(6)	6.56(6)	5.76(5)	5.13(5)	4.45(4)	3.81(4)	3.81(4)	3.81(4)	

Table 9. Same as 7 but for p_T^j 75 GeV.

		$\frac{d}{d^s} \frac{d^{ij,x}}{d^s}$ distribution with N_j 1 p_T^j 100 GeV, j 2 4, K_R K_F 1																	
x_l	x_r	165 GeV	166 GeV	167 GeV	168 GeV	169 GeV	170 GeV	171 GeV	172 GeV	173 GeV	174 GeV	175 GeV	176 GeV	177 GeV	178 GeV	179 GeV	180 GeV	181 GeV	
0.00	0.18	17.87(5)	17.62(5)	17.61(5)	17.33(5)	17.13(5)	17.14(5)	16.87(5)	16.62(4)	16.57(4)	16.43(4)	16.27(4)	16.13(4)	16.03(4)					
0.18	0.22	128.7(4)	128.7(4)	126.6(4)	124.6(4)	123.8(4)	122.8(4)	121.2(4)	118.9(3)	117.8(3)	116.0(3)	115.5(3)	114.4(3)	112.5(3)					
0.22	0.27	214.3(5)	211.6(5)	208.2(4)	205.2(5)	202.5(4)	199.7(4)	196.8(4)	194.6(4)	192.2(4)	189.7(4)	187.5(4)	184.7(4)	182.3(4)					
0.27	0.32	293.0(6)	287.3(6)	284.0(5)	280.5(6)	276.6(5)	272.1(5)	268.5(5)	264.2(5)	259.8(5)	255.7(5)	252.5(5)	248.7(5)	244.0(5)					
0.32	0.38	346.4(6)	340.2(6)	333.7(6)	329.8(6)	323.0(5)	317.9(5)	312.8(5)	308.8(5)	302.4(5)	297.7(5)	291.6(5)	287.7(5)	283.2(5)					
0.38	0.45	356.1(6)	348.3(6)	342.1(5)	335.2(5)	328.7(5)	322.7(5)	315.8(5)	308.7(5)	303.2(5)	298.3(4)	292.0(4)	285.9(5)	281.1(4)					
0.45	0.53	303.7(5)	296.3(5)	290.2(5)	281.8(5)	275.4(5)	267.7(4)	261.7(4)	255.4(4)	247.6(4)	241.9(4)	235.9(4)	229.9(4)	224.9(4)					
0.53	0.62	194.3(4)	187.5(4)	180.2(4)	174.5(4)	168.0(3)	162.4(3)	156.0(3)	151.2(3)	144.9(3)	140.0(3)	134.4(3)	129.5(3)	124.5(3)					
0.62	0.71	71.1(2)	66.8(2)	62.4(2)	58.2(2)	54.6(2)	50.7(2)	47.7(2)	44.4(2)	41.3(2)	38.1(2)	35.3(1)	32.8(1)	29.9(1)					
0.71	1.00	1.73(2)	1.51(2)	1.27(1)	1.03(1)	0.87(1)	0.69(1)	0.560(8)	0.458(7)	0.356(6)	0.281(5)	0.215(4)	0.161(3)	0.116(2)					
		$\frac{d}{d^s} \frac{d^{ij,x}}{d^s}$ distribution with N_j 1 p_T^j 100 GeV, j 2 4, K_R K_F 2																	
x_l	x_r	165 GeV	166 GeV	167 GeV	168 GeV	169 GeV	170 GeV	171 GeV	172 GeV	173 GeV	174 GeV	175 GeV	176 GeV	177 GeV	178 GeV	179 GeV	180 GeV	181 GeV	
0.00	0.18	17.44(3)	17.38(3)	17.03(3)	16.90(3)	16.72(3)	16.53(3)	16.41(3)	16.23(3)	16.05(3)	15.87(3)	15.70(3)	15.56(3)	15.37(3)					
0.18	0.22	120.0(2)	117.8(2)	116.6(3)	115.7(2)	114.2(2)	112.3(2)	110.6(2)	109.2(2)	108.6(2)	107.3(2)	105.4(2)	104.3(2)	103.0(2)					
0.22	0.27	192.4(3)	189.6(3)	187.1(3)	184.5(3)	181.5(3)	179.8(3)	177.5(3)	174.7(3)	172.2(3)	170.2(3)	168.0(3)	165.4(2)	163.4(2)					
0.27	0.32	260.5(4)	255.9(4)	252.3(4)	249.5(4)	244.4(3)	240.9(3)	237.4(3)	233.5(3)	229.9(3)	226.7(3)	222.7(3)	220.1(3)	216.9(3)					
0.32	0.38	305.0(4)	299.5(4)	294.1(4)	288.5(4)	284.1(3)	278.7(3)	274.8(3)	270.0(3)	265.8(3)	260.7(3)	257.0(3)	252.0(3)	246.8(3)					
0.38	0.45	310.2(4)	304.5(3)	298.0(3)	292.2(3)	286.3(3)	280.6(3)	275.3(3)	270.0(3)	263.8(3)	259.2(3)	253.3(3)	248.8(3)	244.2(3)					
0.45	0.53	263.5(3)	256.9(3)	249.7(3)	244.6(3)	238.1(3)	232.4(3)	226.4(3)	220.5(3)	215.2(3)	209.4(3)	204.5(3)	199.2(2)	194.0(2)					
0.53	0.62	167.2(3)	161.3(2)	155.9(2)	150.4(2)	145.0(2)	139.9(2)	134.3(2)	130.0(2)	124.7(2)	120.5(2)	115.8(2)	111.6(2)	107.3(2)					
0.62	0.71	60.7(2)	57.2(2)	53.7(1)	50.3(1)	46.5(1)	43.6(1)	40.8(1)	37.9(1)	35.2(1)	32.5(1)	30.1(1)	27.75(9)	25.73(9)					
0.71	1.00	1.42(1)	1.22(1)	0.99(1)	0.836(9)	0.689(7)	0.554(7)	0.443(6)	0.355(5)	0.277(4)	0.215(3)	0.153(3)	0.116(2)	0.083(2)					
		$\frac{d}{d^s} \frac{d^{ij,x}}{d^s}$ distribution with N_j 1 p_T^j 100 GeV, j 2 4, K_R K_F 0.5																	
x_l	x_r	165 GeV	166 GeV	167 GeV	168 GeV	169 GeV	170 GeV	171 GeV	172 GeV	173 GeV	174 GeV	175 GeV	176 GeV	177 GeV	178 GeV	179 GeV	180 GeV	181 GeV	
0.00	0.18	10.67(9)	10.79(9)	10.69(9)	10.36(8)	10.45(8)	10.65(8)	10.60(8)	10.43(8)	10.48(8)	10.48(7)	10.50(7)	10.37(7)	10.35(7)					
0.18	0.22	105.5(7)	104.8(6)	104.3(6)	103.7(6)	103.7(6)	101.3(6)	101.8(6)	98.7(6)	98.9(6)	97.9(6)	97.7(5)	96.8(5)	96.2(5)					
0.22	0.27	192.6(8)	190.7(8)	187.9(8)	188.3(7)	185.9(8)	182.4(7)	179.7(7)	180.1(7)	177.2(7)	176.2(7)	172.2(7)	171.6(6)	168.8(6)					
0.27	0.32	283.0(1)	277.7(1)	273.6(1)	270.6(9)	264.8(9)	262.6(9)	259.6(9)	256.5(9)	253.5(9)	249.9(8)	248.7(8)	241.3(8)	241.1(8)					
0.32	0.38	347.6(1)	341.9(1)	336.7(1)	329.0(9)	325.2(1)	322.2(1)	315.2(8)	310.1(8)	307.1(9)	299.6(9)	296.1(8)	292.4(7)	286.4(8)					
0.38	0.45	368.3(1)	360.3(9)	356.8(9)	348.0(9)	342.8(9)	336.3(8)	329.1(8)	322.8(8)	316.7(8)	310.1(8)	303.8(8)	300.3(7)	294.0(7)					
0.45	0.53	323.3(8)	315.7(8)	308.4(8)	301.9(8)	291.5(8)	286.0(8)	279.8(7)	271.4(7)	264.3(7)	259.0(7)	254.0(7)	245.9(6)	239.5(6)					
0.53	0.62	210.4(7)	203.4(6)	196.5(6)	189.0(6)	183.1(6)	176.3(6)	170.6(5)	164.6(6)	158.2(5)	152.0(5)	147.6(5)	142.0(5)	136.1(4)					
0.62	0.71	78.3(4)	73.9(4)	69.4(3)	65.6(3)	61.0(3)	56.8(3)	53.0(3)	48.4(3)	46.2(3)	42.7(3)	39.2(2)	36.3(2)	34.0(2)					
0.71	1.00	2.17(3)	1.83(3)	1.49(2)	1.31(2)	1.09(2)	0.89(2)	0.75(1)	0.58(1)	0.484(9)	0.366(8)	0.293(6)	0.233(5)	0.182(4)					

Table 10. Same as 7 but for p_T^j 100 GeV.

		$\frac{d}{d_s} \frac{d_{ij,X}}{d_s}$ distribution with N_j 1 p_T^j 30 GeV, j 2 4, K_R K_F 1																
x_l	x_r	165 GeV	166 GeV	167 GeV	168 GeV	169 GeV	170 GeV	171 GeV	172 GeV	173 GeV	174 GeV	175 GeV	176 GeV	177 GeV	178 GeV	179 GeV	180 GeV	
0.00	0.18	26.70(8)	26.61(8)	26.24(7)	26.18(8)	25.77(8)	25.57(8)	25.25(7)	25.09(7)	24.94(7)	24.68(7)	24.50(7)	24.39(6)	24.03(6)	23.81(6)	23.61(6)	23.42(6)	
0.18	0.22	208.5(7)	206.6(7)	203.9(6)	201.7(7)	199.9(6)	197.8(7)	195.0(6)	192.9(6)	190.5(6)	189.5(6)	187.3(6)	185.5(6)	182.5(5)	180.5(5)	178.5(5)	176.5(5)	
0.22	0.27	381.3(9)	376.4(9)	371.6(9)	366.9(1)	362.8(9)	358.3(9)	353.8(9)	349.6(8)	344.2(8)	340.5(8)	335.0(8)	332.5(8)	327.8(8)	324.5(8)	321.5(8)	318.5(8)	
0.27	0.32	593.0(1)	582.0(1)	575.0(1)	569.0(1)	560.0(1)	551.0(1)	544.0(1)	539.0(1)	530.0(1)	522.0(1)	516.0(1)	512.0(1)	505.0(1)	501.0(1)	497.0(1)	493.0(1)	
0.32	0.38	807.0(1)	799.0(1)	786.0(1)	775.0(2)	762.0(1)	750.0(1)	740.0(1)	727.0(1)	716.0(1)	709.0(1)	698.0(1)	687.0(1)	676.0(1)	671.0(1)	667.0(1)	663.0(1)	
0.38	0.45	1002.0(2)	984.0(2)	968.0(1)	951.0(2)	936.0(2)	922.0(1)	907.0(1)	890.0(1)	876.0(1)	860.0(1)	849.0(1)	832.0(1)	820.0(1)	814.0(1)	809.0(1)	804.0(1)	
0.45	0.53	1110.0(2)	1083.0(2)	1064.0(2)	1044.0(2)	1025.0(2)	1003.0(2)	983.0(2)	969.0(1)	948.0(1)	929.0(1)	913.0(1)	896.0(1)	880.0(1)	872.0(1)	866.0(1)	860.0(1)	
0.53	0.62	1063.0(2)	1040.0(2)	1017.0(1)	993.0(2)	968.0(1)	947.0(1)	925.0(1)	901.0(1)	881.0(1)	862.0(1)	839.0(1)	819.0(1)	801.0(1)	793.0(1)	786.0(1)	779.0(1)	
0.62	0.71	853.0(1)	831.0(1)	804.0(1)	780.0(1)	754.0(1)	731.0(1)	707.0(1)	685.0(1)	664.0(1)	640.0(1)	617.0(1)	598.0(1)	577.1(1)	567.0(1)	559.0(1)	551.0(1)	
0.71	1.00	232.0(4)	218.9(4)	204.1(3)	192.0(4)	179.0(3)	168.4(3)	156.8(3)	146.7(3)	137.1(3)	127.8(3)	119.2(2)	111.3(2)	103.0(2)	100.0(2)	97.0(2)	94.0(2)	
		$\frac{d}{d_s} \frac{d_{ij,X}}{d_s}$ distribution with N_j 1 p_T^j 30 GeV, j 2 4, K_R K_F 2																
x_l	x_r	165 GeV	166 GeV	167 GeV	168 GeV	169 GeV	170 GeV	171 GeV	172 GeV	173 GeV	174 GeV	175 GeV	176 GeV	177 GeV	178 GeV	179 GeV	180 GeV	
0.00	0.18	26.63(5)	26.29(5)	25.96(5)	25.77(5)	25.63(5)	25.23(5)	25.08(5)	24.79(4)	24.35(5)	24.28(4)	24.06(4)	23.78(4)	23.53(4)	23.31(4)	23.11(4)	22.92(4)	
0.18	0.22	194.1(4)	191.4(4)	188.9(4)	187.6(4)	184.7(4)	182.6(4)	181.3(4)	177.8(4)	176.9(4)	174.0(4)	171.6(4)	169.6(4)	168.2(4)	166.5(4)	164.8(4)	163.1(4)	
0.22	0.27	345.6(6)	341.2(6)	336.0(6)	333.1(6)	329.4(6)	324.0(6)	319.3(6)	316.5(5)	311.9(5)	306.5(5)	304.0(5)	299.9(5)	296.6(5)	294.5(5)	292.5(5)	290.5(5)	
0.27	0.32	530.5(9)	521.4(9)	514.7(8)	507.1(9)	498.5(9)	493.2(8)	487.4(8)	479.2(8)	475.3(8)	467.5(7)	460.5(7)	456.3(7)	447.3(7)	443.5(7)	439.5(7)	435.5(7)	
0.32	0.38	715.1(1)	705.9(1)	695.4(1)	683.9(1)	676.7(9)	664.2(9)	651.3(9)	644.0(9)	633.1(9)	626.4(8)	615.9(8)	607.5(8)	599.0(8)	594.5(8)	589.5(8)	584.5(8)	
0.38	0.45	882.0(1)	867.0(1)	852.6(1)	837.0(1)	823.8(9)	813.3(9)	799.5(9)	783.5(9)	773.0(9)	758.0(8)	746.0(9)	734.0(8)	724.5(8)	718.5(8)	713.5(8)	708.5(8)	
0.45	0.53	973.0(1)	953.0(1)	937.0(1)	919.0(1)	903.0(1)	882.8(9)	866.8(9)	849.4(9)	831.9(9)	816.8(8)	802.1(9)	785.6(9)	769.5(8)	761.5(8)	753.5(8)	745.5(8)	
0.53	0.62	932.0(1)	912.0(1)	891.4(1)	869.1(1)	849.1(9)	830.8(9)	809.8(9)	790.0(9)	771.2(9)	754.5(8)	735.2(8)	718.8(8)	701.4(7)	693.5(7)	685.5(7)	677.5(7)	
0.62	0.71	750.6(1)	727.0(9)	704.0(9)	682.6(9)	658.4(9)	639.4(9)	619.2(8)	598.5(8)	579.0(8)	560.4(7)	541.8(7)	524.8(7)	506.4(7)	497.5(7)	488.5(7)	479.5(7)	
0.71	1.00	202.6(3)	190.5(2)	178.3(2)	167.4(2)	156.8(2)	147.1(2)	137.4(2)	128.5(2)	120.1(2)	111.9(2)	104.0(2)	96.9(2)	90.1(1)	86.0(1)	82.0(1)	78.0(1)	
		$\frac{d}{d_s} \frac{d_{ij,X}}{d_s}$ distribution with N_j 1 p_T^j 30 GeV, j 2 4, K_R K_F 0 5																
x_l	x_r	165 GeV	166 GeV	167 GeV	168 GeV	169 GeV	170 GeV	171 GeV	172 GeV	173 GeV	174 GeV	175 GeV	176 GeV	177 GeV	178 GeV	179 GeV	180 GeV	
0.00	0.18	15.0(1)	14.8(1)	14.8(1)	15.0(1)	15.0(1)	14.7(1)	14.7(1)	14.8(1)	14.8(1)	14.5(1)	14.6(1)	14.7(1)	14.5(1)	14.3(1)	14.1(1)	13.9(1)	
0.18	0.22	165.0(1)	163.0(1)	163.0(1)	164.0(1)	159.0(1)	159.0(1)	159.0(1)	155.0(1)	155.0(1)	153.9(9)	153.3(1)	151.4(9)	149.5(9)	147.5(9)	145.5(9)	143.5(9)	
0.22	0.27	338.0(2)	332.0(2)	331.0(2)	328.0(2)	325.0(2)	322.0(1)	318.0(1)	312.0(1)	310.0(1)	306.0(1)	305.0(1)	300.0(1)	298.0(1)	295.0(1)	292.0(1)	289.0(1)	
0.27	0.32	560.0(2)	555.0(2)	548.0(2)	535.0(2)	530.0(2)	522.0(2)	518.0(2)	514.0(2)	506.0(2)	503.0(2)	495.0(2)	486.0(2)	485.0(2)	481.0(2)	477.0(2)	473.0(2)	
0.32	0.38	798.0(3)	787.0(3)	775.0(3)	764.0(3)	754.0(2)	743.0(2)	734.0(2)	721.0(2)	712.0(2)	696.0(2)	695.0(2)	684.0(2)	672.0(2)	665.0(2)	658.0(2)	651.0(2)	
0.38	0.45	1017.0(3)	998.0(3)	981.0(3)	968.0(3)	952.0(3)	938.0(2)	922.0(2)	912.0(2)	893.0(2)	879.0(2)	860.0(2)	853.0(2)	836.0(2)	828.0(2)	820.0(2)	812.0(2)	
0.45	0.53	1151.0(3)	1129.0(3)	1105.0(3)	1086.0(3)	1061.0(3)	1046.0(2)	1025.0(3)	1005.0(2)	984.0(2)	972.0(2)	949.0(2)	935.0(2)	910.0(2)	901.0(2)	893.0(2)	885.0(2)	
0.53	0.62	1119.0(3)	1095.0(3)	1073.0(3)	1045.0(2)	1019.0(2)	996.0(2)	972.0(2)	952.0(2)	928.0(2)	907.0(2)	883.0(2)	859.0(2)	845.0(2)	836.0(2)	828.0(2)	820.0(2)	
0.62	0.71	912.0(2)	886.0(2)	858.0(2)	827.0(2)	803.0(2)	776.0(2)	751.0(2)	728.0(2)	704.0(2)	680.0(2)	660.0(2)	638.0(2)	616.0(2)	607.0(2)	599.0(2)	591.0(2)	
0.71	1.00	250.0(6)	234.8(6)	219.3(6)	205.9(6)	192.9(6)	180.6(5)	169.5(5)	157.8(4)	147.6(4)	138.2(4)	127.9(4)	118.8(4)	111.4(4)	106.0(4)	101.0(4)	96.0(4)	

Table 11. NLO predictions for the s distribution in the pole mass scheme for \sqrt{s} 14 TeV using as input the static scale μ_0 m_t and the ABMP16 NLO PDF set. At least one jet with p_T^j 2 4 and p_T^j 30 GeV is required.

		$\frac{d^{ij,x}}{d^s}$ distribution with N_j															
x_l	x_r	165 GeV	166 GeV	167 GeV	168 GeV	169 GeV	170 GeV	171 GeV	172 GeV	173 GeV	174 GeV	175 GeV	176 GeV	177 GeV	178 GeV	179 GeV	
		$\frac{d^{ij,x}}{d^s}$ distribution with N_j															
		$\frac{d^{ij,x}}{d^s}$ distribution with N_j															
0.00	0.18	26.39(7)	26.18(7)	25.91(7)	25.82(7)	25.41(7)	25.23(7)	24.91(7)	24.72(7)	24.56(6)	24.31(7)	24.13(6)	23.99(6)	23.60(6)	23.45(6)	23.16(4)	
0.18	0.22	199.9(6)	197.9(6)	194.2(6)	193.4(6)	191.3(6)	189.0(6)	186.9(5)	184.1(5)	181.7(5)	180.2(5)	178.8(5)	176.4(5)	174.4(5)	172.8(5)	169.8(4)	
0.22	0.27	351.2(8)	346.0(8)	341.7(8)	336.8(8)	332.9(8)	330.0(7)	324.7(7)	320.1(7)	317.0(7)	312.8(7)	307.3(7)	306.1(7)	300.9(7)	298.8(7)	293.8(6)	
0.27	0.32	521.0(1)	510.0(1)	505.0(1)	499.0(1)	490.0(1)	482.8(1)	477.0(1)	470.5(9)	463.8(9)	457.2(1)	450.9(9)	445.5(9)	440.8(9)	437.8(9)	432.8(8)	
0.32	0.38	672.0(1)	663.0(1)	652.0(1)	643.0(1)	632.0(1)	622.0(1)	612.0(1)	602.0(1)	592.0(1)	584.9(1)	575.7(1)	566.7(9)	556.9(9)	551.9(9)	546.9(8)	
0.38	0.45	778.0(1)	767.0(1)	751.0(1)	739.0(1)	723.0(1)	713.0(1)	701.0(1)	687.7(1)	675.9(1)	663.9(1)	651.6(9)	641.1(9)	630.1(9)	624.1(9)	619.1(8)	
0.45	0.53	794.0(1)	776.0(1)	759.0(1)	744.0(1)	731.0(1)	713.0(1)	699.0(1)	685.8(9)	669.3(9)	655.8(9)	642.4(9)	629.5(9)	615.8(8)	610.8(8)	605.8(7)	
0.53	0.62	681.8(1)	665.5(1)	647.7(9)	628.0(1)	612.1(1)	595.8(9)	580.5(9)	564.9(8)	549.5(8)	535.1(8)	519.4(8)	504.0(8)	491.2(7)	486.2(7)	481.2(6)	
0.62	0.71	462.6(8)	445.6(8)	427.9(8)	411.9(8)	397.0(8)	382.3(8)	365.9(7)	353.3(7)	339.5(6)	325.5(6)	312.3(6)	300.6(6)	286.7(6)	281.7(5)	276.7(4)	
0.71	1.00	77.2(2)	71.4(2)	66.5(2)	61.4(2)	56.5(2)	52.0(1)	48.1(1)	44.1(1)	40.4(1)	37.1(1)	34.1(1)	30.9(1)	28.35(9)	27.85(8)	27.35(7)	
		$\frac{d^{ij,x}}{d^s}$ distribution with N_j															
x_l	x_r	165 GeV	166 GeV	167 GeV	168 GeV	169 GeV	170 GeV	171 GeV	172 GeV	173 GeV	174 GeV	175 GeV	176 GeV	177 GeV	178 GeV	179 GeV	
0.00	0.18	25.97(5)	25.68(5)	25.33(5)	25.13(5)	24.99(4)	24.60(4)	24.45(4)	24.15(4)	23.73(4)	23.65(4)	23.42(4)	23.16(4)	22.90(4)	22.75(4)	22.50(4)	
0.18	0.22	184.1(4)	181.5(4)	179.2(4)	177.8(4)	175.2(4)	173.0(4)	171.7(4)	168.7(3)	167.3(4)	164.7(3)	162.4(3)	160.3(3)	158.8(3)	157.3(3)	155.8(3)	
0.22	0.27	315.6(5)	311.7(5)	306.9(5)	303.8(5)	300.0(5)	295.5(5)	291.1(5)	288.0(5)	284.5(5)	279.2(4)	277.2(4)	273.0(4)	269.3(4)	267.3(4)	263.6(3)	
0.27	0.32	462.4(7)	454.5(7)	448.8(7)	440.6(7)	434.2(7)	429.0(7)	423.3(6)	416.1(6)	412.1(6)	405.6(6)	398.6(6)	394.7(6)	387.9(6)	385.9(6)	382.2(5)	
0.32	0.38	590.9(8)	582.0(7)	573.8(7)	564.1(7)	555.1(7)	545.1(7)	535.5(7)	529.1(7)	519.8(6)	513.3(6)	504.4(6)	496.3(6)	488.8(6)	486.8(6)	483.1(5)	
0.38	0.45	681.6(8)	669.5(8)	656.2(7)	643.1(8)	631.8(7)	623.6(7)	611.8(7)	599.6(7)	590.8(6)	578.9(6)	570.1(6)	558.5(6)	549.8(6)	547.8(6)	544.1(5)	
0.45	0.53	691.6(7)	675.0(7)	661.9(7)	649.2(7)	634.5(7)	620.4(7)	607.5(6)	596.5(6)	583.2(6)	570.2(6)	558.0(6)	546.4(6)	534.2(5)	532.2(5)	528.5(4)	
0.53	0.62	589.0(7)	575.5(6)	560.5(6)	546.1(6)	531.1(6)	517.7(6)	504.1(6)	489.4(5)	475.2(6)	464.1(5)	449.9(5)	438.4(5)	426.5(5)	424.5(5)	420.8(4)	
0.62	0.71	400.6(6)	385.2(6)	370.6(5)	357.4(5)	342.7(5)	331.1(5)	318.0(5)	305.7(4)	293.5(4)	282.2(4)	270.4(4)	259.7(4)	248.2(4)	246.2(4)	242.5(3)	
0.71	1.00	66.5(1)	61.6(1)	57.0(1)	52.6(1)	48.7(1)	44.76(9)	41.32(9)	38.08(9)	34.83(8)	31.95(8)	29.28(7)	26.73(7)	24.33(7)	24.13(7)	23.76(6)	
		$\frac{d^{ij,x}}{d^s}$ distribution with N_j															
x_l	x_r	165 GeV	166 GeV	167 GeV	168 GeV	169 GeV	170 GeV	171 GeV	172 GeV	173 GeV	174 GeV	175 GeV	176 GeV	177 GeV	178 GeV	179 GeV	
0.00	0.18	15.6(1)	15.5(1)	15.4(1)	15.6(1)	15.6(1)	15.3(1)	15.4(1)	15.3(1)	15.3(1)	15.1(1)	15.1(1)	15.3(1)	15.2(1)	15.0(1)	14.8(1)	
0.18	0.22	163.0(1)	161.0(1)	162.0(1)	162.0(1)	157.0(1)	156.0(1)	156.6(1)	153.6(1)	153.0(1)	152.0(8)	151.5(8)	150.5(8)	147.3(8)	147.3(8)	143.6(7)	
0.22	0.27	319.0(1)	314.0(1)	314.0(1)	309.0(1)	306.0(1)	303.0(1)	300.0(1)	294.0(1)	293.0(1)	290.0(1)	286.0(1)	283.0(1)	282.0(1)	280.0(1)	276.3(7)	
0.27	0.32	503.0(2)	500.0(2)	492.0(2)	480.0(2)	478.0(2)	470.0(2)	464.0(2)	459.0(2)	450.0(2)	449.0(1)	441.0(1)	434.0(1)	432.0(1)	430.0(1)	426.3(6)	
0.32	0.38	680.0(2)	666.0(2)	657.0(2)	646.0(2)	637.0(2)	627.0(2)	620.0(2)	609.0(2)	601.0(2)	591.0(2)	584.0(2)	574.0(2)	566.0(1)	564.0(1)	560.3(5)	
0.38	0.45	808.0(2)	791.0(2)	777.0(2)	766.0(2)	751.0(2)	739.0(2)	728.0(2)	714.0(2)	703.0(2)	690.0(2)	678.0(2)	668.0(1)	657.0(1)	655.0(1)	651.3(4)	
0.45	0.53	840.0(2)	823.0(2)	805.0(2)	792.0(2)	771.0(2)	757.0(2)	741.0(2)	725.0(2)	711.0(2)	699.0(2)	683.0(1)	670.0(1)	653.0(1)	653.0(1)	649.3(3)	
0.53	0.62	731.0(2)	714.0(2)	696.0(2)	676.0(2)	662.0(2)	641.0(1)	627.0(1)	608.0(1)	592.0(1)	576.0(1)	560.0(1)	542.0(1)	531.0(1)	531.0(1)	527.3(2)	
0.62	0.71	504.0(1)	487.0(1)	467.0(1)	448.0(1)	433.0(1)	416.0(1)	399.0(1)	384.0(1)	370.0(1)	353.0(1)	340.7(1)	326.9(1)	315.6(9)	315.6(9)	311.9(8)	
0.71	1.00	85.6(3)	78.7(3)	73.2(3)	68.2(3)	62.5(3)	57.8(2)	53.3(2)	48.8(2)	45.2(2)	41.1(2)	37.6(2)	34.4(2)	31.3(1)	31.3(1)	30.9(1)	

Table 12. Same as Fig. 11 but for $p_T^j = 50$ GeV.

		$\frac{d}{d^s} \frac{d^j}{d^i} x$ distribution with N_j																
x_l	x_r	165 GeV	166 GeV	167 GeV	168 GeV	169 GeV	170 GeV	171 GeV	172 GeV	173 GeV	174 GeV	175 GeV	176 GeV	177 GeV	178 GeV	179 GeV	180 GeV	
		$\frac{d}{d^s} \frac{d^j}{d^i} x$ distribution with N_j																
		$\frac{d}{d^s} \frac{d^j}{d^i} x$ distribution with N_j																
0.00	0.18	25.61(7)	25.42(7)	25.11(6)	25.06(7)	24.63(7)	24.45(7)	24.13(6)	24.00(6)	23.79(6)	23.61(6)	23.32(6)	23.22(6)	22.88(5)	22.81(4)	22.62(4)	22.35(4)	22.05(4)
0.18	0.22	185.5(6)	183.8(5)	180.1(5)	178.8(6)	176.8(5)	175.1(5)	173.5(5)	170.0(5)	168.5(5)	166.9(5)	165.8(5)	163.5(5)	161.3(4)	152.1(3)	150.0(3)	147.9(3)	146.5(3)
0.22	0.27	309.4(7)	305.6(7)	302.5(6)	297.7(7)	295.0(7)	290.6(6)	286.5(6)	282.8(6)	279.4(6)	275.1(6)	271.3(6)	268.2(6)	264.5(5)	245.6(4)	243.6(4)	240.0(4)	236.4(4)
0.27	0.32	437.3(9)	429.0(8)	423.8(8)	418.7(9)	410.7(8)	403.9(8)	397.5(8)	393.9(7)	387.6(7)	382.7(8)	377.5(7)	372.1(7)	367.3(7)	338.4(5)	333.1(5)	328.8(5)	323.2(5)
0.32	0.38	534.6(9)	525.0(9)	516.9(8)	509.5(9)	500.3(8)	492.8(8)	483.5(8)	474.9(7)	467.1(8)	461.6(8)	454.0(7)	446.0(7)	437.8(7)	409.1(5)	403.5(5)	397.3(5)	384.4(4)
0.38	0.45	574.9(9)	566.9(9)	555.5(8)	545.6(9)	534.3(8)	525.0(8)	515.2(8)	506.5(7)	495.8(7)	486.0(7)	476.5(7)	469.2(7)	460.2(6)	431.7(5)	423.8(5)	415.8(5)	399.8(4)
0.45	0.53	535.5(8)	523.1(8)	512.3(7)	499.8(8)	489.5(7)	476.7(7)	465.4(7)	455.3(7)	445.8(7)	435.1(6)	424.7(6)	415.7(6)	406.0(6)	377.5(5)	370.9(5)	363.3(5)	350.4(4)
0.53	0.62	400.0(7)	387.7(7)	375.4(6)	364.2(7)	352.8(6)	341.8(6)	332.5(6)	320.8(5)	310.7(5)	300.9(5)	292.3(5)	281.7(5)	273.8(5)	252.2(3)	244.7(3)	236.6(3)	226.6(3)
0.62	0.71	210.4(5)	201.3(5)	191.3(4)	181.7(5)	173.8(4)	165.4(4)	157.1(4)	149.2(4)	141.4(4)	133.7(4)	127.2(3)	120.5(3)	112.9(3)	108.8(2)	103.5(2)	97.1(2)	91.1(2)
0.71	1.00	16.76(7)	15.24(7)	13.69(6)	12.33(7)	10.93(6)	9.68(5)	8.67(5)	7.70(5)	6.78(4)	5.87(4)	5.16(4)	4.50(3)	3.85(3)	3.82(2)	3.49(2)	3.20(2)	3.00(2)
		$\frac{d}{d^s} \frac{d^j}{d^i} x$ distribution with N_j																
x_l	x_r	165 GeV	166 GeV	167 GeV	168 GeV	169 GeV	170 GeV	171 GeV	172 GeV	173 GeV	174 GeV	175 GeV	176 GeV	177 GeV	178 GeV	179 GeV	180 GeV	
0.00	0.18	25.04(5)	24.76(5)	24.43(4)	24.25(4)	24.10(4)	23.74(4)	23.59(4)	23.31(4)	22.88(4)	22.81(4)	22.62(4)	22.35(4)	22.05(4)	200.0(1)	194.0(1)	188.0(1)	
0.18	0.22	170.5(4)	168.4(4)	166.0(4)	164.0(4)	161.6(3)	159.7(3)	158.3(3)	155.6(3)	154.3(3)	152.1(3)	150.0(3)	147.9(3)	146.5(3)	133.1(5)	128.8(5)	124.5(5)	
0.22	0.27	278.6(5)	275.2(5)	270.9(4)	267.7(4)	264.1(4)	260.4(4)	256.6(4)	253.5(4)	250.2(4)	245.6(4)	243.6(4)	240.0(4)	236.4(4)	217.3(3)	213.0(3)	208.7(3)	
0.27	0.32	387.5(6)	380.5(6)	375.3(5)	369.0(6)	363.3(5)	358.7(5)	353.5(5)	348.1(5)	343.6(5)	338.4(5)	333.1(5)	328.8(5)	323.2(5)	304.4(4)	299.1(4)	293.8(4)	
0.32	0.38	468.0(6)	461.3(6)	453.1(5)	445.7(6)	439.4(5)	430.4(5)	423.1(5)	417.2(5)	409.1(5)	403.5(5)	397.3(5)	389.9(5)	384.4(4)	365.3(4)	359.0(4)	353.7(4)	
0.38	0.45	503.3(6)	494.4(6)	484.1(5)	473.4(6)	465.7(5)	457.6(5)	449.1(5)	440.0(5)	431.7(5)	423.8(5)	415.8(5)	407.8(4)	399.8(4)	380.7(3)	374.4(3)	368.1(3)	
0.45	0.53	465.3(5)	453.9(5)	444.1(5)	434.2(5)	425.6(5)	413.4(5)	404.2(4)	395.4(4)	386.5(4)	376.4(4)	368.3(4)	359.7(4)	350.4(4)	331.3(3)	325.0(3)	318.7(3)	
0.53	0.62	344.1(4)	333.7(4)	323.8(4)	314.4(4)	304.5(4)	295.8(4)	286.9(4)	277.4(4)	269.0(3)	260.7(3)	252.2(3)	244.7(3)	236.6(3)	217.3(2)	213.0(2)	208.7(2)	
0.62	0.71	181.4(3)	173.5(3)	164.8(3)	156.9(3)	149.5(3)	142.4(3)	134.9(3)	128.5(2)	121.5(2)	115.0(2)	108.8(2)	103.5(2)	97.1(2)	93.0(1)	88.7(1)	84.4(1)	
0.71	1.00	14.35(5)	12.90(5)	11.59(4)	10.39(4)	9.21(4)	8.27(4)	7.34(3)	6.52(3)	5.71(3)	4.99(3)	4.39(2)	3.82(2)	3.30(2)	3.20(2)	2.90(2)	2.70(2)	
		$\frac{d}{d^s} \frac{d^j}{d^i} x$ distribution with N_j																
x_l	x_r	165 GeV	166 GeV	167 GeV	168 GeV	169 GeV	170 GeV	171 GeV	172 GeV	173 GeV	174 GeV	175 GeV	176 GeV	177 GeV	178 GeV	179 GeV	180 GeV	
0.00	0.18	15.6(1)	15.4(1)	15.3(1)	15.5(1)	15.3(1)	15.3(1)	15.3(1)	15.3(1)	15.3(1)	15.3(1)	15.0(1)	15.2(1)	15.0(1)	140.0(1)	134.0(1)	128.0(1)	
0.18	0.22	152.5(1)	150.8(1)	151.7(1)	150.7(9)	147.4(9)	146.5(9)	146.6(9)	144.4(9)	143.1(9)	142.3(8)	141.0(8)	140.3(8)	138.3(8)	125.0(1)	120.7(1)	116.4(1)	
0.22	0.27	284.0(1)	279.0(1)	278.0(1)	274.0(1)	271.0(1)	269.0(1)	266.0(1)	261.0(1)	260.0(1)	256.2(9)	254.4(1)	250.0(1)	250.0(1)	231.3(0)	227.0(0)	222.7(0)	
0.27	0.32	421.0(2)	421.0(2)	414.0(1)	405.0(1)	401.0(1)	395.0(1)	389.0(1)	385.0(1)	379.0(1)	377.0(1)	371.0(1)	365.0(1)	362.0(1)	343.3(0)	339.0(0)	334.7(0)	
0.32	0.38	541.0(2)	530.0(2)	521.0(2)	513.0(2)	508.0(1)	497.0(1)	492.0(1)	484.0(1)	476.0(1)	467.0(1)	462.0(1)	455.0(1)	450.0(1)	431.3(0)	427.0(0)	422.7(0)	
0.38	0.45	600.0(1)	588.0(1)	580.0(1)	568.0(1)	558.0(1)	548.0(1)	541.0(1)	529.0(1)	518.0(1)	510.0(1)	498.0(1)	490.0(1)	483.0(1)	464.3(0)	460.0(0)	455.7(0)	
0.45	0.53	571.0(1)	559.0(1)	545.0(1)	532.0(1)	520.0(1)	509.0(1)	497.0(1)	486.0(1)	475.0(1)	467.0(1)	454.5(1)	445.4(1)	434.7(1)	415.0(0)	410.7(0)	406.4(0)	
0.53	0.62	431.0(1)	420.0(1)	408.0(1)	396.0(1)	385.0(1)	371.7(1)	361.9(9)	349.9(9)	339.4(9)	328.1(8)	318.8(8)	306.4(8)	297.1(8)	277.3(0)	273.0(0)	268.7(0)	
0.62	0.71	232.2(8)	222.1(8)	209.8(8)	199.9(7)	190.7(7)	181.7(7)	172.2(6)	164.2(6)	157.1(6)	148.2(6)	140.2(5)	132.2(5)	125.5(5)	120.7(0)	116.4(0)	112.1(0)	
0.71	1.00	19.0(1)	17.0(1)	15.4(1)	13.9(1)	12.46(9)	11.11(9)	9.86(8)	8.65(7)	7.68(7)	6.71(6)	5.95(6)	5.21(5)	4.43(5)	4.30(2)	4.00(2)	3.70(2)	

Table 13. Same as Fig. 11 but for $p_T^j = 75$ GeV.

		$\frac{d^{ij,x}}{d^s}$ distribution with N_j 1 p_T^j 100 GeV, j 2 4, K_R K_F 1															
x_l	x_r	165 GeV	166 GeV	167 GeV	168 GeV	169 GeV	170 GeV	171 GeV	172 GeV	173 GeV	174 GeV	175 GeV	176 GeV	177 GeV	178 GeV	179 GeV	
0.00	0.18	24.43(7)	24.23(6)	24.04(6)	23.89(6)	23.57(6)	23.43(6)	23.02(6)	22.90(6)	22.71(6)	22.60(6)	22.32(6)	22.14(5)	21.91(5)			
0.18	0.22	168.6(5)	167.4(5)	164.2(4)	162.4(5)	161.0(5)	159.0(5)	157.4(4)	154.7(4)	153.3(4)	151.6(4)	149.9(4)	147.8(4)	146.5(4)			
0.22	0.27	268.8(6)	266.0(6)	262.6(5)	258.4(6)	256.4(6)	253.0(6)	248.9(5)	246.2(5)	242.7(5)	239.8(5)	235.6(5)	233.1(5)	230.2(5)			
0.27	0.32	364.3(7)	356.5(7)	352.9(7)	348.3(8)	342.7(7)	335.9(7)	330.6(7)	326.6(6)	322.8(6)	317.6(6)	312.6(6)	309.8(6)	303.9(6)			
0.32	0.38	423.4(7)	415.4(7)	408.6(7)	402.9(7)	395.9(7)	388.9(6)	382.1(7)	375.6(6)	368.8(6)	363.9(6)	357.6(6)	352.6(6)	345.8(6)			
0.38	0.45	428.3(7)	421.7(7)	411.8(6)	404.0(7)	395.3(6)	389.1(6)	381.3(6)	374.0(6)	366.1(6)	358.2(5)	351.4(5)	344.0(5)	337.8(5)			
0.45	0.53	363.2(6)	353.4(6)	345.9(6)	335.6(6)	328.9(6)	320.0(5)	311.5(5)	303.8(5)	296.8(5)	289.5(5)	282.2(5)	274.4(4)	268.0(4)			
0.53	0.62	228.8(5)	221.5(5)	213.4(4)	206.2(5)	198.7(4)	191.5(4)	185.2(4)	177.9(4)	171.8(3)	165.1(4)	159.9(3)	152.1(3)	147.7(3)			
0.62	0.71	83.6(3)	78.2(3)	73.9(2)	68.9(3)	64.3(2)	59.7(2)	55.8(2)	52.1(2)	48.4(2)	44.8(2)	41.3(2)	38.6(2)	35.3(2)			
0.71	1.00	2.08(2)	1.76(2)	1.45(2)	1.21(2)	1.01(1)	0.82(1)	0.68(1)	0.524(8)	0.419(7)	0.332(6)	0.245(5)	0.181(4)	0.143(3)			
		$\frac{d^{ij,x}}{d^s}$ distribution with N_j 1 p_T^j 100 GeV, j 2 4, K_R K_F 2															
x_l	x_r	165 GeV	166 GeV	167 GeV	168 GeV	169 GeV	170 GeV	171 GeV	172 GeV	173 GeV	174 GeV	175 GeV	176 GeV	177 GeV	178 GeV	179 GeV	
0.00	0.18	23.99(4)	23.67(4)	23.40(4)	23.17(4)	23.02(4)	22.69(4)	22.54(4)	22.28(4)	21.88(4)	21.79(4)	21.60(3)	21.36(3)	21.08(4)			
0.18	0.22	155.6(3)	153.6(3)	151.6(3)	149.6(3)	147.3(3)	145.6(3)	144.0(3)	141.8(3)	140.2(3)	138.7(3)	136.7(3)	134.9(3)	133.0(3)			
0.22	0.27	243.5(4)	240.4(4)	236.7(4)	233.8(4)	230.4(4)	227.2(3)	223.7(3)	220.7(3)	218.2(3)	214.3(3)	211.9(3)	209.2(3)	206.0(3)			
0.27	0.32	322.7(5)	317.7(5)	313.1(5)	308.2(5)	303.7(4)	298.7(4)	294.3(4)	289.9(4)	286.2(4)	282.2(4)	276.8(4)	273.5(4)	268.9(4)			
0.32	0.38	371.9(5)	366.3(5)	359.6(4)	354.4(5)	347.8(4)	341.8(4)	335.8(4)	329.9(4)	323.7(4)	319.3(4)	313.8(4)	308.7(4)	303.2(4)			
0.38	0.45	375.3(4)	367.7(4)	360.4(4)	352.8(4)	345.1(4)	339.6(4)	332.7(4)	325.4(4)	319.3(4)	313.1(3)	305.8(4)	300.7(3)	294.7(3)			
0.45	0.53	315.5(4)	306.7(4)	300.0(4)	292.5(4)	285.7(3)	277.7(3)	270.6(3)	264.3(3)	257.4(3)	250.7(3)	244.6(3)	238.0(3)	231.4(3)			
0.53	0.62	197.4(3)	191.1(3)	184.2(3)	178.3(3)	172.1(3)	165.2(3)	160.0(3)	153.5(2)	148.0(2)	142.4(2)	137.3(2)	132.1(2)	127.4(2)			
0.62	0.71	72.0(2)	67.5(2)	62.9(2)	58.9(2)	55.1(2)	51.6(2)	47.6(1)	44.6(1)	41.4(1)	38.2(1)	35.4(1)	32.8(1)	30.1(1)			
0.71	1.00	1.68(1)	1.43(1)	1.19(1)	0.97(1)	0.808(9)	0.655(8)	0.514(7)	0.413(6)	0.320(5)	0.242(4)	0.183(3)	0.141(3)	0.094(2)			
		$\frac{d^{ij,x}}{d^s}$ distribution with N_j 1 p_T^j 100 GeV, j 2 4, K_R K_F 0.5															
x_l	x_r	165 GeV	166 GeV	167 GeV	168 GeV	169 GeV	170 GeV	171 GeV	172 GeV	173 GeV	174 GeV	175 GeV	176 GeV	177 GeV	178 GeV	179 GeV	
0.00	0.18	14.9(1)	14.8(1)	14.7(1)	14.9(1)	14.8(1)	14.6(1)	14.6(1)	14.7(1)	14.5(1)	14.50(9)	14.36(9)	14.49(9)	14.39(9)			
0.18	0.22	137.6(9)	136.3(9)	137.3(9)	136.8(8)	133.5(8)	132.7(8)	131.9(8)	130.7(8)	130.0(8)	128.4(7)	127.8(7)	127.1(7)	125.8(7)			
0.22	0.27	247.0(1)	240.0(1)	240.0(1)	237.5(1)	234.3(1)	232.7(9)	229.2(9)	226.5(9)	225.4(9)	221.2(8)	219.5(8)	216.6(8)	216.5(8)			
0.27	0.32	350.0(1)	348.0(1)	341.0(1)	336.0(1)	333.0(1)	328.0(1)	323.0(1)	318.0(1)	313.0(1)	312.0(1)	305.9(1)	302.5(1)	299.3(1)			
0.32	0.38	426.0(1)	418.0(1)	412.0(1)	403.0(1)	400.0(1)	391.0(1)	387.0(1)	379.0(1)	377.0(1)	368.8(1)	364.7(1)	358.5(9)	353.8(9)			
0.38	0.45	444.0(1)	436.0(1)	428.0(1)	422.0(1)	415.0(1)	405.0(1)	398.0(1)	389.8(9)	381.8(9)	374.2(9)	365.6(9)	360.7(9)	355.4(8)			
0.45	0.53	388.0(1)	376.8(1)	366.9(1)	358.8(1)	349.6(9)	341.4(9)	332.5(9)	325.8(8)	316.6(8)	311.2(8)	301.9(8)	294.9(7)	289.0(7)			
0.53	0.62	248.0(8)	240.8(8)	232.5(8)	224.2(7)	217.0(7)	208.7(7)	202.8(6)	194.0(6)	188.6(6)	180.6(6)	174.5(5)	167.7(5)	161.5(5)			
0.62	0.71	93.1(5)	87.2(4)	82.0(4)	76.4(4)	71.2(4)	66.4(4)	61.8(3)	57.5(3)	53.6(3)	49.7(3)	46.4(3)	42.6(3)	39.5(2)			
0.71	1.00	2.45(3)	2.12(3)	1.82(3)	1.52(3)	1.29(2)	1.08(2)	0.83(2)	0.70(1)	0.56(1)	0.443(9)	0.346(7)	0.291(6)	0.201(4)			

Table 14. Same as Fig. 11 but for p_T^j 100 GeV.

References

- [1] S. Alioli, P. Fernandez, J. Fuster, A. Irlles, S. Moch, P. Uwer, and M. Vos, *A new observable to measure the top-quark mass at hadron colliders*, Eur. Phys. J. C **73** (2013) 2438, [[arXiv:1303.6415](#)].
- [2] **ATLAS** Collaboration, G. Aad et. al., *Determination of the top-quark pole mass using $t\bar{t}$ + 1-jet events collected with the ATLAS experiment in 7 TeV pp collisions*, JHEP **10** (2015) 121, [[arXiv:1507.01769](#)].
- [3] J. Fuster, A. Irlles, D. Melini, P. Uwer, and M. Vos, *Extracting the top-quark running mass using $t\bar{t}$ 1-jet events produced at the Large Hadron Collider*, Eur. Phys. J. C **77** (2017), no. 11 794, [[arXiv:1704.00540](#)].
- [4] **CMS** Collaboration, *Determination of the normalised invariant mass distribution of $t\bar{t}$ jet and extraction of the top quark mass*, CMS-PAS-TOP-13-006.
- [5] **ATLAS** Collaboration, G. Aad et. al., *Measurement of the top-quark mass in $t\bar{t}$ 1-jet events collected with the ATLAS detector in pp collisions at $\sqrt{s} = 8$ TeV*, JHEP **11** (2019) 150, [[arXiv:1905.02302](#)].
- [6] A. H. Hoang, A. Jain, I. Scimemi, and I. W. Stewart, *Infrared Renormalization Group Flow for Heavy Quark Masses*, Phys. Rev. Lett. **101** (2008) 151602, [[arXiv:0803.4214](#)].
- [7] A. H. Hoang, A. Jain, C. Lepenik, V. Mateu, M. Preisser, I. Scimemi, and I. W. Stewart, *The MSR mass and the O_{QCD} renormalon sum rule*, JHEP **04** (2018) 003, [[arXiv:1704.01580](#)].
- [8] **CMS** Collaboration, A. M. Sirunyan et. al., *Measurement of $t\bar{t}$ normalised multi-differential cross sections in pp collisions at $\sqrt{s} = 13$ TeV, and simultaneous determination of the strong coupling strength, top quark pole mass, and parton distribution functions*, Eur. Phys. J. C **80** (2020), no. 7 658, [[arXiv:1904.05237](#)].
- [9] S. Dittmaier, P. Uwer, and S. Weinzierl, *NLO QCD corrections to t anti- t + jet production at hadron colliders*, Phys. Rev. Lett. **98** (2007) 262002, [[hep-ph/0703120](#)].
- [10] S. Dittmaier, P. Uwer, and S. Weinzierl, *Hadronic top-quark pair production in association with a hard jet at next-to-leading order QCD: Phenomenological studies for the Tevatron and the LHC*, Eur. Phys. J. C **59** (2009) 625–646, [[arXiv:0810.0452](#)].
- [11] K. Melnikov and M. Schulze, *NLO QCD corrections to top quark pair production in association with one hard jet at hadron colliders*, Nucl. Phys. B **840** (2010) 129–159, [[arXiv:1004.3284](#)].
- [12] K. Melnikov, A. Scharf, and M. Schulze, *Top quark pair production in association with a jet: QCD corrections and jet radiation in top quark decays*, Phys. Rev. D **85** (2012) 054002, [[arXiv:1111.4991](#)].
- [13] G. Bevilacqua, H. B. Hartanto, M. Kraus, and M. Worek, *Top Quark Pair Production in Association with a Jet with Next-to-Leading-Order QCD Off-Shell Effects at the Large Hadron Collider*, Phys. Rev. Lett. **116** (2016), no. 5 052003, [[arXiv:1509.09242](#)].

- [14] G. Bevilacqua, H. B. Hartanto, M. Kraus, and M. Worek, *Off-shell Top Quarks with One Jet at the LHC: A comprehensive analysis at NLO QCD*, JHEP **11** (2016) 098, [[arXiv:1609.01659](#)].
- [15] R. K. Ellis, Z. Kunszt, K. Melnikov, and G. Zanderighi, *One-loop calculations in quantum field theory: from Feynman diagrams to unitarity cuts*, Phys. Rept. **518** (2012) 141–250, [[arXiv:1105.4319](#)].
- [16] G. Bevilacqua, M. Czakon, M. V. Garzelli, A. van Hameren, A. Kardos, C. G. Papadopoulos, R. Pittau, and M. Worek, *HELAC-NLO*, Comput. Phys. Commun. **184** (2013) 986–997, [[arXiv:1110.1499](#)].
- [17] G. Ossola, C. G. Papadopoulos, and R. Pittau, *Reducing full one-loop amplitudes to scalar integrals at the integrand level*, Nucl. Phys. B **763** (2007) 147–169, [[hep-ph/0609007](#)].
- [18] P. Draggiotis, M. V. Garzelli, C. G. Papadopoulos, and R. Pittau, *Feynman Rules for the Rational Part of the QCD 1-loop amplitudes*, JHEP **04** (2009) 072, [[arXiv:0903.0356](#)].
- [19] V. Hirschi, R. Frederix, S. Frixione, M. V. Garzelli, F. Maltoni, and R. Pittau, *Automation of one-loop QCD corrections*, JHEP **05** (2011) 044, [[arXiv:1103.0621](#)].
- [20] G. Cullen, N. Greiner, G. Heinrich, G. Luisoni, P. Mastrolia, G. Ossola, T. Reiter, and F. Tramontano, *Automated One-Loop Calculations with GoSam*, Eur. Phys. J. C **72** (2012) 1889, [[arXiv:1111.2034](#)].
- [21] G. Cullen et. al., *GOSAM-2.0: a tool for automated one-loop calculations within the Standard Model and beyond*, Eur. Phys. J. C **74** (2014), no. 8 3001, [[arXiv:1404.7096](#)].
- [22] F. Cascioli, P. Maierhofer, and S. Pozzorini, *Scattering Amplitudes with Open Loops*, Phys. Rev. Lett. **108** (2012) 111601, [[arXiv:1111.5206](#)].
- [23] F. Buccioni, J.-N. Lang, J. M. Lindert, P. Maierhöfer, S. Pozzorini, H. Zhang, and M. F. Zoller, *OpenLoops 2*, Eur. Phys. J. C **79** (2019), no. 10 866, [[arXiv:1907.13071](#)].
- [24] S. Actis, A. Denner, L. Hofer, J.-N. Lang, A. Scharf, and S. Uccirati, *RECOLA: REcursive Computation of One-Loop Amplitudes*, Comput. Phys. Commun. **214** (2017) 140–173, [[arXiv:1605.01090](#)].
- [25] A. Denner, J.-N. Lang, and S. Uccirati, *Recola2: REcursive Computation of One-Loop Amplitudes 2*, Comput. Phys. Commun. **224** (2018) 346–361, [[arXiv:1711.07388](#)].
- [26] S. Catani, S. Dittmaier, M. H. Seymour, and Z. Trocsanyi, *The Dipole formalism for next-to-leading order QCD calculations with massive partons*, Nucl. Phys. B **627** (2002) 189–265, [[hep-ph/0201036](#)].
- [27] S. Frixione, Z. Kunszt, and A. Signer, *Three jet cross-sections to next-to-leading order*, Nucl. Phys. B **467** (1996) 399–442, [[hep-ph/9512328](#)].
- [28] Z. Nagy and D. E. Soper, *Parton showers with quantum interference: Leading color, with spin*, JHEP **07** (2008) 025, [[arXiv:0805.0216](#)].
- [29] G. Bevilacqua, M. Czakon, M. Kubocz, and M. Worek, *Complete Nagy-Soper subtraction for next-to-leading order calculations in QCD*, JHEP **10** (2013) 204, [[arXiv:1308.5605](#)].

- [30] M. A. Ebert and F. J. Tackmann, *Impact of isolation and fiducial cuts on q_T and N -jettiness subtractions*, JHEP **03** (2020) 158, [[arXiv:1911.08486](#)].
- [31] S. Alekhin, A. Kardos, S. Moch, and Z. Trócsányi, *Precision studies for Drell–Yan processes at NNLO*, Eur. Phys. J. C **81** (2021), no. 7 573, [[arXiv:2104.02400](#)].
- [32] P. Nason, *A New method for combining NLO QCD with shower Monte Carlo algorithms*, JHEP **11** (2004) 040, [[hep-ph/0409146](#)].
- [33] S. Frixione, P. Nason, and C. Oleari, *Matching NLO QCD computations with Parton Shower simulations: the POWHEG method*, JHEP **11** (2007) 070, [[arXiv:0709.2092](#)].
- [34] S. Frixione and B. R. Webber, *Matching NLO QCD computations and parton shower simulations*, JHEP **06** (2002) 029, [[hep-ph/0204244](#)].
- [35] A. Kardos, C. Papadopoulos, and Z. Trocsanyi, *Top quark pair production in association with a jet with NLO parton showering*, Phys. Lett. B **705** (2011) 76–81, [[arXiv:1101.2672](#)].
- [36] S. Alioli, P. Nason, C. Oleari, and E. Re, *A general framework for implementing NLO calculations in shower Monte Carlo programs: the POWHEG BOX*, JHEP **06** (2010) 043, [[arXiv:1002.2581](#)].
- [37] T. Sjostrand, S. Mrenna, and P. Z. Skands, *PYTHIA 6.4 Physics and Manual*, JHEP **05** (2006) 026, [[hep-ph/0603175](#)].
- [38] G. Corcella, I. G. Knowles, G. Marchesini, S. Moretti, K. Odagiri, P. Richardson, M. H. Seymour, and B. R. Webber, *HERWIG 6.5 release note*, [hep-ph/0210213](#).
- [39] S. Alioli, S. Moch, and P. Uwer, *Hadronic top-quark pair-production with one jet and parton showering*, JHEP **01** (2012) 137, [[arXiv:1110.5251](#)].
- [40] J. Alwall, R. Frederix, S. Frixione, V. Hirschi, F. Maltoni, O. Mattelaer, H. S. Shao, T. Stelzer, P. Torrielli, and M. Zaro, *The automated computation of tree-level and next-to-leading order differential cross sections, and their matching to parton shower simulations*, JHEP **07** (2014) 079, [[arXiv:1405.0301](#)].
- [41] T. Sjöstrand, *The PYTHIA Event Generator: Past, Present and Future*, Comput. Phys. Commun. **246** (2020) 106910, [[arXiv:1907.09874](#)].
- [42] J. Bellm *et. al.*, *Herwig 7.1 Release Note*, [arXiv:1705.06919](#).
- [43] J. Bellm *et. al.*, *Herwig 7.0/Herwig++ 3.0 release note*, Eur. Phys. J. C **76** (2016), no. 4 196, [[arXiv:1512.01178](#)].
- [44] M. Czakon, H. B. Hartanto, M. Kraus, and M. Worek, *Matching the Nagy-Soper parton shower at next-to-leading order*, JHEP **06** (2015) 033, [[arXiv:1502.00925](#)].
- [45] Z. Nagy and D. E. Soper, *A parton shower based on factorization of the quantum density matrix*, JHEP **06** (2014) 097, [[arXiv:1401.6364](#)].
- [46] Z. Nagy and D. E. Soper, *Effects of subleading color in a parton shower*, JHEP **07** (2015) 119, [[arXiv:1501.00778](#)].

- [47] C. Gütschow, J. M. Lindert, and M. Schönherr, *Multi-jet merged top-pair production including electroweak corrections*, Eur. Phys. J. C **78** (2018), no. 4 317, [[arXiv:1803.00950](#)].
- [48] S. Hoeche, F. Krauss, M. Schonherr, and F. Siegert, *QCD matrix elements + parton showers: The NLO case*, JHEP **04** (2013) 027, [[arXiv:1207.5030](#)].
- [49] **Sherpa** Collaboration, E. Bothmann *et. al.*, *Event Generation with Sherpa 2.2*, SciPost Phys. **7** (2019), no. 3 034, [[arXiv:1905.09127](#)].
- [50] R. Frederix, E. Re, and P. Torrielli, *Single-top t -channel hadroproduction in the four-flavour scheme with POWHEG and aMC@NLO*, JHEP **09** (2012) 130, [[arXiv:1207.5391](#)].
- [51] G. Bevilacqua, M. V. Garzelli, and A. Kardos, *$t\bar{t}b\bar{b}$ hadroproduction with massive bottom quarks with PowHel*, [[arXiv:1709.06915](#)].
- [52] S. Alekhin, J. Blümlein, and S. Moch, *NLO PDFs from the ABMP16 fit*, Eur. Phys. J. C **78** (2018), no. 6 477, [[arXiv:1803.07537](#)].
- [53] T.-J. Hou *et. al.*, *New CTEQ global analysis of quantum chromodynamics with high-precision data from the LHC*, Phys. Rev. D **103** (2021), no. 1 014013, [[arXiv:1912.10053](#)].
- [54] L. A. Harland-Lang, A. D. Martin, P. Motylinski, and R. S. Thorne, *Parton distributions in the LHC era: MMHT 2014 PDFs*, Eur. Phys. J. C **75** (2015), no. 5 204, [[arXiv:1412.3989](#)].
- [55] S. Bailey, T. Cridge, L. A. Harland-Lang, A. D. Martin, and R. S. Thorne, *Parton distributions from LHC, HERA, Tevatron and fixed target data: MSHT20 PDFs*, Eur. Phys. J. C **81** (2021), no. 4 341, [[arXiv:2012.04684](#)].
- [56] **NNPDF** Collaboration, R. D. Ball *et. al.*, *Parton distributions from high-precision collider data*, Eur. Phys. J. C **77** (2017), no. 10 663, [[arXiv:1706.00428](#)].
- [57] A. Buckley, J. Ferrando, S. Lloyd, K. Nordström, B. Page, M. Rüfenacht, M. Schönherr, and G. Watt, *LHAPDF6: parton density access in the LHC precision era*, Eur. Phys. J. C **75** (2015) 132, [[arXiv:1412.7420](#)].
- [58] M. Cacciari, G. P. Salam, and G. Soyez, *The anti- k_t jet clustering algorithm*, JHEP **04** (2008) 063, [[arXiv:0802.1189](#)].
- [59] M. Cacciari, G. P. Salam, and G. Soyez, *FastJet User Manual*, Eur. Phys. J. C **72** (2012) 1896, [[arXiv:1111.6097](#)].
- [60] S. Catani, M. Ciafaloni, and F. Hautmann, *High-energy factorization and small x heavy flavor production*, Nucl. Phys. B **366** (1991) 135–188.
- [61] R. D. Ball and R. K. Ellis, *Heavy quark production at high-energy*, JHEP **05** (2001) 053, [[hep-ph/0101199](#)].
- [62] **PROSA** Collaboration, O. Zenaiev *et. al.*, *Impact of heavy-flavour production cross sections measured by the LHCb experiment on parton distribution functions at low x* , Eur. Phys. J. C **75** (2015), no. 8 396, [[arXiv:1503.04581](#)].

- [63] S. Alekhin, J. Blümlein, and S. Moch, *The ABM parton distributions tuned to LHC data*, Phys. Rev. D **89** (2014), no. 5 054028, [[arXiv:1310.3059](#)].
- [64] T.-J. Hou et. al., *Progress in the CTEQ-TEA NNLO global QCD analysis*, [arXiv:1908.11394](#).
- [65] U. Langenfeld, S. Moch, and P. Uwer, *Measuring the running top-quark mass*, Phys. Rev. D **80** (2009) 054009, [[arXiv:0906.5273](#)].
- [66] P. Marquard, A. V. Smirnov, V. A. Smirnov, and M. Steinhauser, *Quark Mass Relations to Four-Loop Order in Perturbative QCD*, Phys. Rev. Lett. **114** (2015), no. 14 142002, [[arXiv:1502.01030](#)].
- [67] K. G. Chetyrkin, J. H. Kühn, and M. Steinhauser, *RunDec: A Mathematica package for running and decoupling of the strong coupling and quark masses*, Comput. Phys. Commun. **133** (2000) 43–65, [[hep-ph/0004189](#)].
- [68] F. Herren and M. Steinhauser, *Version 3 of RunDec and CRunDec*, Comput. Phys. Commun. **224** (2018) 333–345, [[arXiv:1703.03751](#)].
- [69] M. V. Garzelli, L. Kemmler, S. Moch, and O. Zenaiev, *Heavy-flavor hadro-production with heavy-quark masses renormalized in the \overline{MS} , MSR and on-shell schemes*, JHEP **04** (2021) 043, [[arXiv:2009.07763](#)].
- [70] A. H. Hoang, C. Lepenik, and V. Mateu, *REvolver: Automated running and matching of couplings and masses in QCD*, Comput. Phys. Commun. **270** (2022) 108145, [[arXiv:2102.01085](#)].
- [71] S. Alioli, J. Fuster, M.V. Garzelli, A. Gavardi, A. Irlles, D. Melini, S. Moch, P. Uwer, K. Voß, *Complete set of predictions in online repository*, <https://ttj-phenomenology.web.cern.ch/>, 2022.
- [72] G. Bevilacqua, H. B. Hartanto, M. Kraus, M. Schulze, and M. Worek, *Top quark mass studies with $t\bar{t}j$ at the LHC*, JHEP **03** (2018) 169, [[arXiv:1710.07515](#)].
- [73] A. Denner, S. Dittmaier, S. Kallweit, and S. Pozzorini, *NLO QCD corrections to off-shell top-antitop production with leptonic decays at hadron colliders*, JHEP **10** (2012) 110, [[arXiv:1207.5018](#)].
- [74] S. Dulat, T.-J. Hou, J. Gao, M. Guzzi, J. Huston, P. Nadolsky, J. Pumplin, C. Schmidt, D. Stump, and C. P. Yuan, *New parton distribution functions from a global analysis of quantum chromodynamics*, Phys. Rev. **D93** (2016), no. 3 033006, [[arXiv:1506.07443](#)].
- [75] M. Jezabek and J. H. Kühn, *QCD Corrections to Semileptonic Decays of Heavy Quarks*, Nucl. Phys. **B314** (1989) 1–6.